UNIVERSIDAD AUTÓNOMA DE MADRID

FACULTAD DE CIENCIAS

DEPARTAMENTO DE FÍSICA APLICADA

Advanced applications of porous silicon: biofunctionalized luminescent particles and ZnO based white light emitting nanocomposites

Memoria que presenta
Darío Gallach Pérez

Para optar al grado de
Doctor

Directores:
Prof. Dr. D. Miguel Manso Silván
Prof. Dr. D. Vicente Torres Costa

Madrid, 2015

A mis padres y a Arancha

Agradecimientos

Permíteme, estimado lector, que dedique estos renglones a las personas que, de un modo u otro, han contribuido a que en este momento tengas este documento entre tus manos. A ellos se lo debo, porque con ellos he dado mis primeros pasos tambaleantes en el mundo científico.

Como es usanza, voy a comenzar los agradecimientos por mis mentores: Miguel Manso y Vicente Torres. Ellos me permitieron formar parte de su grupo de trabajo, han compartido conmigo su conocimiento y me han dado la oportunidad de desarrollar mi capacidad investigadora dejándome una sana libertad de actuación que me ha templado el carácter.

Entré hace seis años en un Departamento al que no sabía que podría acabar teniendo tanto afecto. Me he sentido como en casa con todos sus integrantes, aprendiendo de ellos a investigar y a enseñar. He tenido la suerte de conocer a personas como mi buen amigo Manuel Hernández, con quien he crecido sobremanera no sólo en el ámbito profesional sino en el personal; Aurelio Climent, que me ha enseñado que física y arte van de la mano y con quien paso ratos entretenidos resolviendo problemas de electromagnetismo; Basilio García, con quien empecé dando clases en la UAM de electrónica digital y que nunca he dejado de dar desde entonces. También es imposible olvidarse de José Manuel Martínez, Raúl Martín Palma, Máximo León, José Luis Castaño, Antonio Arranz, José Luis Pau, Carlos Palacio, Manuel Cervera, Lalo, María Jesús Hernández, Rafael Pérez, Alejandro Braña, Alejandro Gutiérrez, Carmen Morant, Nair López, Pilar Prieto, Raquel Caballero, José Manuel Merino, Óscar Bomatí, Luis Galán o Pablo Pernas. Todos han contribuido en algo a mi historia. No puedo olvidarme de Beatriz Luna, que es la base sobre la que descansa todo el Departamento.

Es imposible olvidarme de Predes, quien desempeña la labor de embajadora de mi madre en la Facultad y como tal, por tenerme un cariño extraordinario. De ella he aprendido muchísimo sobre biología y me ha hecho darme realmente cuenta de lo que implica que todo sistema tienda a un mínimo de energía.

Tengo mucho que agradecer a la gente del C4, Ginés Lifante, Jon Martínez y, por supuesto, Paco Jaque, que me acogieron como técnico del SNOM en mitad de mi tesis. Sin ellos tal vez no estaría escribiendo estas palabras. Paco, además de tratarme como a uno más desde el primer día, ha resultado ser otro punto de inflexión en mi vida por su manera de ver la ciencia y la vida. Indudablemente hay que nombrar a José Luis Plaza, con el que tan bien lo he pasado dando clases en la Boston. Espero tener contacto con él para "darle la lata" y que haga más cristales.

Durante la tesis suelen hacerse estancias, que permiten conocer cómo se investiga en otros lugares y tener acceso a otras técnicas y al conocimiento de otros especialistas. Estos períodos permiten, además, conocer a gente estupenda como la que he conocido en Milán. Tengo que darle las gracias a Simona Binetti por acogerme en su grupo y a la gente del equipo: Andrea, Raluca, Alessia, Zara, Bruno, Laura… he pasado un tiempo inmejorable.

No me he olvidado tampoco de los doctorandos del Departamento, tanto de los que están como de los que ya son Doctores: Guille, con quien tantas horas de física recreativa he pasado; Álvaro, que es como un hermano mayor; Dani, Vali, Edu, Jacobo, Noelia, Esther, Chloé, Paola, Rosalía…

Tampoco se puede uno olvidar del importante apoyo técnico dado por Luis y Tomás. En este caso, tengo que agradecer a Luis que, además de ser un plomo, sea un cabezón porque no son pocas las veces que me ha ayudado a razonar y a hacerme ver dónde me fallan los conocimientos. ¿Y los técnicos del SIdI? La mitad de mi estudio no existiría de no ser por Esperanza, Enrique, Isi y Noemí.

He de dar las gracias también a mis amigos fuera de la Universidad, especialmente a Javier, Patricia, Robert y Miguel; porque han sido los que más se han preocupado por mí durante todo este tiempo.

Y claro, a mi pequeña familia. A mi madre, por haberme ayudado a dar los primeros pasos no en la ciencia sino en la vida; a mi tío, quien me contagió la curiosidad por todo desde pequeño y a mi padre, a quien perdí al comienzo de esta andadura y a quien le habría encantado estar conmigo en este momento para ver la tesis de su hijo junto a la suya en la UAM.

Reservo para el final el expresar mi gratitud hacia Arancha, por su cariño y su amor demostrado a diario, por comprenderme, por aguantarme, por ser paciente y comprensiva y por haber aguantado el fuerte tirón de la tesis habiéndose quedado sin vacaciones "sin protestar".

Summary

Porous silicon (PS) is a material with special properties. Its most relevant characteristic is the efficient photoluminescence at room temperature caused by quantum confinement, but not less attractive are its biocompatibility and high surface to volume ratio. All these properties make this material especially suitable for biomedical and optoelectronic applications and thus, the present study aims at deepening in PS conditioning towards applications in these fields.

On the one hand, the functionalization of luminescent PS particles has been studied for possible biomedical applications by two different ways: silanization (using 3-Aminopropyltriethoxysilane) and pegilation (using polyethylene-glycol). Both molecules have attractive properties: the former has amino capping groups ($-NH_2$) capable of linking biomolecules such proteins or DNA to the particles, while the latter (with two hydroxyl (-OH) ending groups), makes the particles more soluble in aqueous media. The synthesis and full colloidal and surface characterization has been achieved, showing that PS is conveniently conjugated forming particles in the micron range. In addition, it has been considered how functionalization protects the particles from oxidation, preserving their luminescence for longer time with respect to pristine PS particles.

On the other hand, new applications of PS are envisaged by a proper combination with zinc oxide (ZnO) to produce ZnO-PS nanocomposites. The structures where grown by combining the electrochemical anodization of Si with a sol-gel process for permeation of the formed PS with ZnO. Intermediate annealing temperatures have been optimized to crystallize the ZnO nanoclusters, making these compatible with the presence of Si quantum dots within PS. More specifically, this work is focused in the existent correlation between luminescence and the PS-ZnO fine structure after sample annealing at different temperatures in air. The luminescence changes allows us to tune the emission and form white light electroluminescent devices based exclusively on PS and ZnO. Furthermore, the lack of a model that explains the electrical behavior and the mechanism of white-light emission from these structures moved us to propose one.

Resumen

El silicio poroso (PS) es un material con propiedades especiales. Su característica más relevante es la luminiscencia a temperatura ambiente causada por el confinamiento cuántico, pero no son menos atractivas su biocompatibilidad y elevada relación superficie-volumen. Todas ellas hacen del PS un material adecuado para aplicaciones en biomedicina y optoelectrónica. Por ello, el presente estudio pretende profundizar en su aplicación en estos campos.

Por un lado, se han estudiado dos maneras diferentes de funcionalizar nanopartículas luminiscentes de PS para aplicaciones biomédicas: silanización (con 3-Aminopropiltrietoxisilano) y pegilación (con polietilenglicol). Ambas moléculas tienen propiedades atractivas: la primera posee terminaciones amino (-NH_2) capaces de enlazar biomoléculas tales como proteínas o ADN a las partículas, mientras que la segunda tiene terminaciones hidroxilo (-OH), que hace que sean más duraderas en medios acuosos. Se ha llevado a cabo la síntesis y caracterización, observando cómo el PS está conjugado formando partículas en el rango de las micras. Además, se ha considerado cómo la funcionalización protege a las partículas de la oxidación, preservando su luminiscencia por períodos más largos de tiempo en comparación con partículas no modificadas.

Por otro lado, la combinación de PS y óxido de zinc (ZnO) para formar nanocompositos de PS-ZnO abre la posibilidad de nuevas aplicaciones. Estas estructuras fueron sintetizadas combinando la anodización electroquímica del Si con un proceso de sol-gel para su permeabilización con ZnO. Se han optimizado los tratamientos térmicos a temperaturas moderadas en aire para cristalizar el ZnO, haciendo que sea compatible con la presencia de puntos cuánticos de Si existentes en el PS. Específicamente, esta parte del trabajo se centra en la correlación existente entre la luminiscencia y la estructura fina de los nanocompositos de PS-ZnO. Los cambios en la luminiscencia permiten ajustar la emisión y producir dispositivos electroluminiscentes de luz blanca basados exclusivamente en PS y ZnO. Además, se propone un modelo que explica el comportamiento eléctrico y el mecanismo de emisión de luz blanca.

Acronyms

AcZn: Zinc Acetate

APTS: 3-Aminopropyltriethoxysilane

APTS-PSps: APTS-modified PSps

BE: Binding Energy

CDF: Cumulative distribution function

CB: Conduction Band

CE: Counter Electrode

DT: Direct Tunneling

EBS: Elastic Backscattering Spectroscopy

EDX: Energy-Dispersive X-Ray Spectroscopy

EL: Electroluminescence

EtOH: Ethanol

FESEM: Field Emission Scanning Electron Microscopy

FN: Fowler-Norheim

GIXD: Grazing Incidence X-Ray Diffraction

IC: Integrated Circuit

ITO: Indium Tin Oxide

MEA: Monoethanolamine

O_i: Oxygen Interstitial

O_{Zn}: Oxygen antisite

p^+-Si: Higly doped p-type Si

PEG: polyethylene glycol

PEG-PSps: PEG-modified PSps

PL: Photoluminescence

PS: Porous Silicon

PS-ZnO: Porous Silicon – Zinc Oxide

PSps: Porous Silicon Particles

QDs: Quantum Dots

RE: Reference Electrode

RT: Room Temperature

RTP: Rapid Thermal Processing

SAED: Selected Area Electron Diffraction

SEM: Scanning Electron Microscopy

SSWLS: Solid-State White-Light Source

TEM: Transmission Electron Microscopy

UV: Ultraviolet

UV-Vis: Ultraviolet-Visible Spectroscopy

VB: Valence Band

V_O: Oxygen Vacancy

V_{Zn}: Zinc vacancy

WE: Working Electrode

XAFS: X-ray Absorption Spectroscopy

XPS: X-ray Photoelectron Spectroscopy

XRD: X-Ray Diffraction

Zn_i: Zinc Interstitial

ZnO: Zinc Oxide

Index

CHAPTER 1

Introduction

This chapter gives a short introduction to the main properties of porous silicon (PS) and how they drove us to study applications in fields like biomedicine and optoelectronics that, at a first glance, seem to be very different. Specifically, the approach of this work to the former application is through the functionalization of PS particles while to the latter is the use of PS thin films permeated with zinc oxide (ZnO). The state of the art of both systems is discussed to later show the motivations that lead us to work on them.

1.1 A brief introduction to Silicon

Since the middle of the 20th century, the impact of silicon (Si) on science, technology and welfare is unquestioned. It has revolutionized the world of electronics stablishing itself as the fundamental component in integrated circuit (IC) technology. The reason lies, on the one hand, in its semiconductor character and the possibility of easily change its conductivity by doping with III or V elements **[1]**. On the other hand, not less important is the fact that Si was the first material from which high quality crystalline wafers without surface impurities nor contamination were fabricated **[2]**. In addition, it is interesting to point out that Si is the second most abundant element on Earth's crust **[3]**.

From the biomedical point of view, although some *in vivo* and *in vitro* experiments have determined that bulk Si is not a biocompatible material **[4, 5]**, small amounts of this element are indispensable for connective tissues such as bone, aorta, trachea and tendon **[6]**. However, Si is unstable in aqueous solutions (like

living organisms) or air and rapidly oxidizes to form a passivating silica (SiO_x, $x \approx 2$) layer **[7]**, which does not generate a negative response in the organism **[8]**.

From the optoelectronics point of view, Si has an indirect energy band gap of 1.12 eV at room temperature (RT). This means that electrons (e^-) and holes (h^+) are found at different locations in the Brillouin zone and thus, their recombination by emitting only a photon is not efficient because it requires another particle capable of carrying momentum (i.e. a phonon) **[9]**. The participation of this particle drops the efficiency several orders of magnitude being 10^{-5}% at RT, making Si unsuitable for light-emitting technology **[10]**. To make it worse, the Si band gap energy is smaller than that of visible photons (with energies between 3.2 and 1.8 eV) and thus, all of them are completely absorbed.

These properties of Si make us question ourselves about its suitability for biomedical and optoelectronic applications. However, when the size of a material is reduced to the nanoscale, its chemical and physical properties may change **[11]**. In the case of Si, these new properties arising from quantum mechanics were accidentally discovered in the 1950s at Bell Labs **[12]**.

1.2 Porous Silicon

The first report about porous silicon (PS) was published in 1956 by the Uhlirs while they were working in the electro-polishing of Ge and Si. They realized that the resulting surface of Si under certain etching conditions in hydrofluoric acid (HF) solutions was porous and rough instead of smooth and polished. Results were published as a curious but somehow irrelevant phenomenon **[12]**. The real interest in this material started in 1990, when efficient red-orange photoluminescence (PL) at RT was reported. This effect was attributed to the Si band-gap widening and the enhanced exciton recombination caused by quantum size effects in Si quantum dots (QDs) formed during the PS synthesis **[13, 14]**. This discovery led to a flood of work principally focused on creating Si-based optoelectronic devices compatible with IC technology such light-emitting devices **[15, 16]** or solar cells **[17, 18]** to mention some examples. However, problems with PS chemical and mechanical

stability led to a drop in interest some years later **[19]**. Many of these problems have been already solved and PS is being used not only for optoelectronic applications but also for biomedical applications such drug delivery **[20, 21]**, biosensors **[22, 23]** or therapeutics **[24, 25]**.

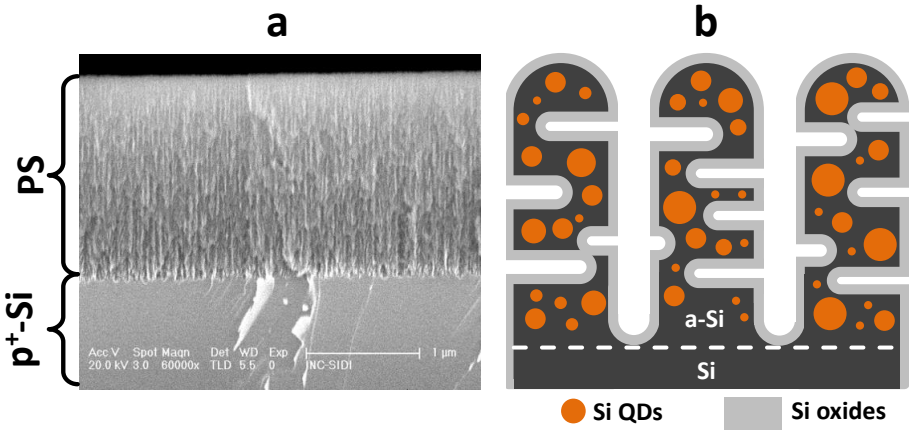

Figure 1.1: FESEM image of a PS sample anodized at 80 mA·cm^{-2} during 30 s (**a**). Schematic view of the typical distribution of PS components adapted from **[26]** (**b**).

PS is usually formed by etching crystalline Si wafers in HF-based electrolytes **[27]**. There are two chemical ways to produce PS: electrochemical anodization **[28]** and stain etching **[29]**. Although mechanisms are different, the objective of both techniques is to dissolve Si atoms from the wafer to form a porous structure. In this work, we will focus on the electrochemical anodization to produce mesoporous PS (pores with diameters between 2 and 50 nm).

Fig. 1.1a shows a field-emission scanning electron microscopy (FESEM) image of such a type of PS. As seen on **Fig. 1.1b**, its structure is constituted by Si QDs embedded in an amorphous Si (a-Si) matrix **[30]** whose surface is gradually oxidized over time in contact with air. Although it will be discussed in **Chapter 2**, it is important to take into account from now on, that the first stages in the PS oxidation lead to a combination of Si-OH and SiO_x, ($x \approx 2$) while further oxidation (specially at high temperatures) results in surfaces that are totally covered by silica **[28, 30-32]**. Transmission electron microscopy (TEM) showed that Si QDs are

round shaped with a size distribution between 20 and 80 Å without a preferential orientation **[33, 34]**.

Some of the most important properties of PS in contrast to bulk Si material can be itemized as follows:

- **Efficient luminescence at RT.** Perhaps this is the most remarkable PS characteristic and the most important one for optoelectronic applications. As mentioned before, Si QDs produce a strong, efficient red-orange photoluminescence at RT (**Fig. 1.2**) due to the enhanced exciton recombinations caused by quantum confinement **[13, 35]**, overcoming the problem of the Si indirect band gap. However, PL measurements show broad emission bands whose origin lies in the Si QDs size distribution (**Fig. 1.1b**). This emission can be tuned by adjusting the electrochemical process. Just to mention some examples, red, green and blue luminescent PS has been reported in the literature **[36-38]**.

Figure 1.2: PS samples anodized at different conditions observed through an optical longpass filter (λ_c=550 nm) while being illuminated with ultraviolet light.

- **High surface to volume ratio (10^2 to 10^3 m^2/cm^3).** During etching, Si is dissolved due to the action of HF and forms pores in the bulk material.

The surface to volume ratio is directly dependent on the etching current density **[30]**. This characteristic makes this material especially suitable for an interaction with different molecules for sensing applications **[39, 40]**, drug delivery **[20, 25]** or for permeation with other materials **[25, 41].**

- **Biocompatibility and biodegradability.** In contrast to Si and silica, PS' biocompatibility depends on formation conditions. Upon formation, it shows a surface covered by Si-H_x bonds (x=1,2,3). Under these conditions, this material is toxic as demonstrated in *in vitro* essays since it generates oxygenated radicals due to its high reactivity **[42]**. However, as mentioned before, PS is rapidly oxidized forming silica and degrades in orthosilicic acid ($SiOH_4$) which is easily removed by the kidneys **[43]**.

- **Compatibility with conventional microfabrication of Si.** This is another important feature especially for the optoelectronic industry, opening the possibility to create thick high-quality oxide layers **[28]** and light emitting devices **[16]**. In addition, many interesting materials are required to be incorporated in the current Si-based IC technology and PS opens the possibility to integrate them in a single composite avoiding tensile stress due to different thermal expansion coefficient or lattice mismatch **[44]**.

1.3 PS nanoparticles for biomedical applications

Nanoparticles are used for fluorescent biological labeling **[45, 46]** or directly in medicine for imaging, drug and gene delivery or therapeutics **[47, 48]** to mention some examples. For most of these applications, we expect from these nanoparticles to be biocompatible (in order to make them interact with a biological entity) and biodegradable (disappearing from the organism once their work was done). Of course, some of these functions can be combined or improved by functionalization with different functional groups **[49]**.

Taking this into account, PS exhibits the basic properties, such as biocompatibility and biodegradability and adds interesting characteristics such large surface to volume ratio **[41]**, high reactivity and luminescence at RT **[13]**. Relevantly, the physicochemical properties have attracted much interest in view of the biocompatibility of PS when placed in contact with epithelium **[50]**, bone **[51]** and ophthalmic tissues **[52]**. These PS characteristic opened the way to bioapplications both for *in vitro* biosensors **[53, 54]** as well as for *in vivo* systems as biofunctional targets for epithelial tissues or diagnosis **[55, 56]**, contrast agents and hyperthermia induction **[57]** or focused drug delivery **[58]**. In this respect, further studies have been opened since PS performance (in the form of films) is limited and should be optimized by the formation of porous silicon particles (PSps) **[48]**.

Several methods have been proposed for the micronization of electrochemically anodized PS surfaces to form particles. These include a previous step of PS film delamination plus alternative ultrasound **[59]** or mechanical milling **[60]** methods. In certain cases a cutting layer is formed by increasing current density **[55]** to favor delamination. In order to control particle size and/or distribution, different chemistries are used **[59]** (i.e. including HNO_3 in the etching HF-based electrolyte), microfiltration steps applied **[61]** or micropatterning processes employed **[55]**. It is clear that under such processes the risk of alteration of the electrochemically etched Si is of concern. In particular, oxidation of the Si nanocrystals is considered as the origin of the short life viability of the PSps' PL.

1.4 PS matrices for optoelectronic applications

As mentioned before, PS has attracted much attention since the observation of its efficient luminescence at room temperature **[13]**. This particular property makes this material interesting for optoelectronic applications. In fact, only one year after the discovery of this feature, the first PS-based electroluminescent device was reported **[15]**. However, PS is highly reactive and is quickly oxidized when exposed to the atmosphere, losing its luminescence and becoming more resistive over time. These problems soon lead to a decreasing interest in this material for this kind of applications.

One attractive approach to solve these problems in order to produce efficient electroluminescent devices is to passivate and preserve the PS luminescence by filling its pores with transparent and conductive materials **[62, 63]**. Indeed, this approach allows combining the optoelectronic properties of different materials while at the same time stablishes an ingenious way to integrate others with the current Si-based IC technology **[44, 64]**. So far, PS has been combined with different materials such as Rhodamine 6G **[62]**, ZnS **[65]**, CdS **[66]**, laser dyes **[67]**, SnO_2 **[68]**, or ZnO **[62]** to mention some examples. Among them, the combination of PS and ZnO to produce PS-ZnO nanocomposites is especially attractive since the observation of white PL **[69-72]** from such a system. This feature attracted much attention due to its potential applications in solid-state white-light sources (SSWLS) **[70, 73]**.

ZnO is a wide band gap ($E_{g,ZnO}$=3.37 eV at RT) semiconductor with a high exciton binding energy (60 meV). This material has a characteristic PL emission composed of a strong UV emission as a result of band-to-band exciton recombinations and a blue-green visible emission due to the presence of characteristic intrinsic defects in the ZnO structure **[74]**. Therefore, the white light emission is the combination of the PS red-orange luminescence and the blue-green visible emission due to the presence of characteristic intrinsic point defects present in the ZnO structure **[74]**. The way these defects are able to produce blue-green luminescence is still under debate. Some authors related this emission with donor defects (n-type) like oxygen vacancies (V_O) **[71, 75-77]** or interstitial zinc (Zn_i) **[78, 79]**; others, by acceptors (p-type) like zinc vacancies (V_{Zn}) **[79, 80]**, oxygen interstitials (O_i) **[71]** or oxygen antisites (O_{Zn}) **[81-83]**.

Different chemical and physical approaches have been followed to combine ZnO with PS, such as pulsed laser deposition **[69]**, magnetron sputtering **[71, 73]**, thermal spray **[62]** or sol-gel spin-coating **[44, 77, 84]**. Among them, the sol-gel technique is a simple, low cost and flexible technique **[44]**. It allows an optimal infiltration of ZnO inside the PS matrix to take advantage of the high internal PS surface to achieve an enhanced interaction between them. In addition, this technique improves the crystallization and the infiltration inside the pores protecting PS against further oxidation **[62]**. Relevantly, the sol-gel technique has been

described to produce proper nanocomposites with adjustable optoelectronic properties since low surface tension ZnO precursors are able to easily permeate the PS with precise Zn^{2+} concentrations **[85]**.

1.5 Thesis motivation and objectives

This work studies the possible usage of the PS interesting properties to biomedical applications (i.e. PS in the form of nanoparticles) and optoelectronics (i.e. PS in the form of thin films). The strategy for the development of new configurations of both types of PS structures is focused as follows:

- **Biomedical applications**: This part of the work aims at describing a process for the fabrication of PSps based on surface modification aiming at a twofold improvement: preserve its RT luminescence (as proved previously for adsorbed dextran **[86]**) and adapt the biocompatibility/biofunctionality in two different frames. On the one hand, poorly biointeractive PSps based on polyethylene glycol (PEG) **[87]** can be functional for long circulating times in the blood stream and, on the second hand, amino-functional PSps can be activated for protein or DNA driven specific recognition through (3-aminopropyl)triethoxysilane (APTS), as performed **[88]** following similar procedures to previously reported hydrosilylized PSps **[89]**.

- **Optoelectronic applications**: A wide variety of PS-ZnO optoelectronic devices has been proposed until now **[90-92]**. However, and in spite of several efforts to understand the mechanisms ruling the behaviour of these devices, there is an apparent lack of understanding that requires deepening in microstructural aspects and deriving appropriate physical models. In particular, it is patent that PS-ZnO devices depend strongly on the methods of preparation and on particular processing steps. This part of the work is committed to understand the effect of the annealing steps in air applied to PS-ZnO nanocomposites prepared by the sol-gel process. Understanding the correlation between fine structure and luminescence in PS-ZnO

nanocomposites is the first step to develop solid-state Si-based white light-emitting devices.

With these objectives in mind, this thesis is divided (excluding this one) in five more chapters. **Chapter 2** is divided in two parts: the first one contains the experimental details of the sample synthesis such as PS formation, functionalization, combination with ZnO and formation of electroluminescent devices, while the second part contains details about the particular characterization of each system and a brief introduction to the techniques reported. **Chapter 3** is focused on the results from the study about PS nanoparticles, especially their morphology, surface chemistry and photoluminescence. **Chapter 4** is devoted to the study of the relation that exists between the PS-ZnO composites microstructure and their luminescence. **Chapter 5** is the sequel of the PS-ZnO composites characterization but more focused in its optoelectronic properties to produce PS-ZnO electroluminescent devices. A model is proposed to explain its behavior. Finally, **Chapter 6** collects all conclusions derived from this work.

CHAPTER 2:

Experimental Techniques

This chapter is divided in three well defined sections. The first one, named synthesis techniques, begins by explaining the PS formation since this step is common to both systems under study (i.e. functionalized particles and PS-ZnO nanocomposites), making way to describe the protocols used for their particular synthesis. In all cases, the experimental conditions and the specific techniques applied are described in detail. The second section, named characterization techniques, sketches out very briefly each technique used and the configuration applied to study the samples. Finally, the third section describes the specific parameters used during the measurements in each case.

2.1 Synthesis techniques

2.1.1 PS formation by electrochemical anodization

All PS samples synthesized in this work were made by electrochemical anodization. The reason is that this technique allows a precise control of all PS main characteristics (i.e. pore size, porosity and thickness). Although both chemical and physical principles involved in the formation of PS are essentially the same, the specific experimental procedure requires slight variations depending on the type of Si that is going to be etched (i.e. dopants or resistivity above all) **[30]**. For that reason, the description of the PS formation is adapted to our particular case in which all samples where produced from p^+-type, B-doped, (100), low resistivity (0.01-0.05 Ω·cm) Si wafers to obtain mesoporous PS layers.

The first step towards the formation of PS is to stablish an ohmic back-side contact to the Si wafer before the electrochemical anodization. These contacts where formed by depositing a 200 nm thick Al layer by electron beam evaporation following recommended procedures **[28]**. To improve the Si-Al junction, a rapid thermal processing (RTP) of the samples is carried out at 450 ºC for 10 min. in a N_2 atmosphere producing a graded ohmic junction.

Fig. 2.1 shows the experimental setup for the electrochemical anodization. This process takes place in a Teflon beaker filled with an electrolyte formed by aqueous HF(48%) and ethanol (HF:EtOH, 1:2 in volume). The Si wafer is placed in contact with a Cu working electrode (WE) through the ohmic contact so that its front side is exposed to the electrolyte forming a semiconductor-electrolyte junction where the anodization process occurs. Two additional Pt wires are used as counter (CE) and reference (RE) electrodes. All electrodes are connected to a galvanostat that supplies the adequate voltage to maintain a constant etching current.

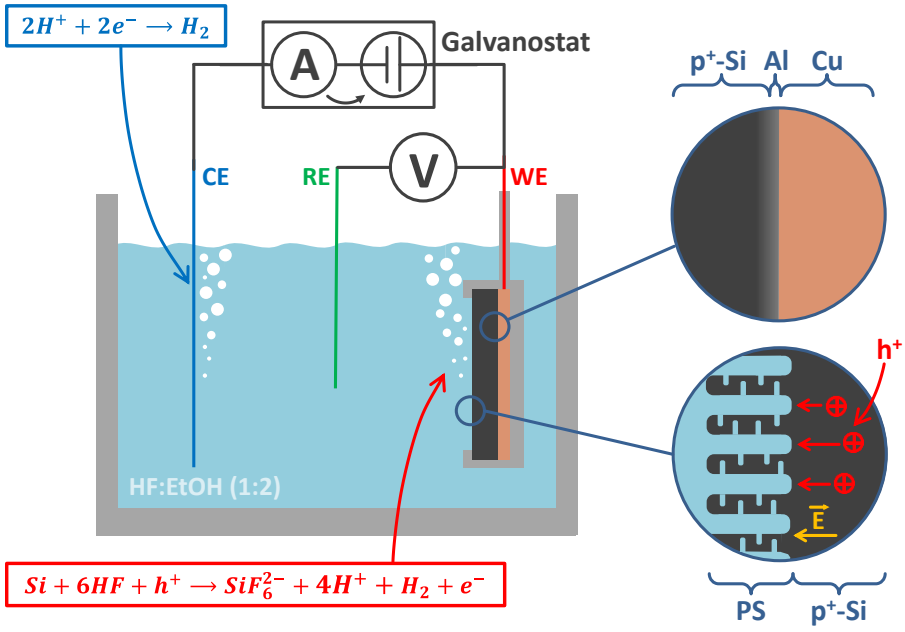

Figure 2.1: Scheme of the electrochemical cell used for PS formation, the main chemical reactions that take place during anodization and the pore formation dominated by holes (h^+).

Since bare Si is thermodynamically unstable when exposed to air or an aqueous solution, the surface of these wafers have a native SiO_2 layer of several angstroms **[7]** that inhibits the formation of PS. However, SiO_2 is spontaneously removed when placed in contact with the HF:EtOH (1:2) solution, allowing progress of the following reactions **[93]**:

$$SiO_2 + 6HF \rightarrow SiF_6^{2-} + 2H_2O + 2H^+ \qquad \textbf{Eq. 2.1}$$

$$SiO_2 + 3HF_2^- \rightarrow SiF_6^{2-} + H_2O + OH^- \qquad \textbf{Eq. 2.2}$$

The dissolution of the native oxide leaves the surface covered by Si-H bonds, as reported by infrared spectroscopy, **[94]** low energy electron diffraction **[95]** and scanning tunneling microscopy **[96]**. Under this passivated condition, the Si wafer is stable inside the solution if no holes (h^+) reach the surface. However, since our wafer is p^+-Si, these charge carriers are available at room temperature (RT) and the dissolution of Si is constant but limited by their diffusion to the surface (which is very slow). This process is accelerated by the electrochemical anodization, in which the galvanostat sets a positive voltage to the WE and holes are efficiently injected from the bulk to the semiconductor-electrolyte interface while attracting F^- ions. As seen on **Fig. 2.1**, the result is an oxidation at the Si surface (WE) and a reduction at the CE (note that both chemical processes produce H_2) **[28]**.

The way a Si atom is removed from the wafer under this condition is not well understood yet **[93]**. However, the mechanism discussed in the following lines is the most widely accepted since it explains the previous observations **[97]**. The whole process is depicted in **Fig. 2.2**. It begins when an h^+ is injected from the bulk to the surface by the positive voltage induced in the WE, causing a nucleophilic attack on a Si-H bond by a F^- ion (I). The new Si-F bond polarizes the Si-Si backbonds, making this atom susceptible for further attacks. Two hydrogen atoms can then combine and an electron (e^-) is injected into the substrate (II). The H_2 molecule formed is liberated and the second Si-F bond is stablished. The Si-Si backbonds support an

increasing polarization so that they suddenly suffer an attack by two HF molecules (III). The H atoms will substitute the Si-Si for Si-H bonds and F^- ions will finish the dissolution of the Si atom by forming SiF_4. In addition, this molecule reacts immediately with two new HF molecules to form a SiF_6^{2-} fluoroanion (IV). Note that the surface of the Si wafer ends passivated with H atoms and ready for the dissolution of new atoms as soon as another h^+ reaches the surface.

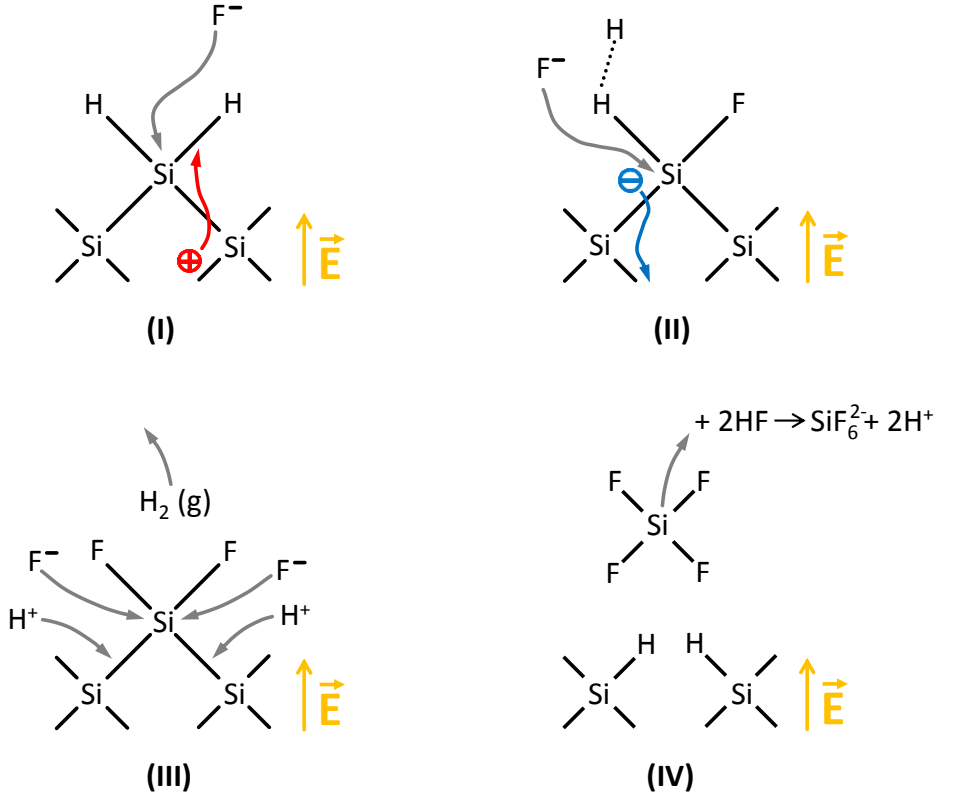

Figure 2.2: Dissolution mechanism of Si in HF associated with PS formation **[97]**.

So far, the process explains how pores can be formed, but it does not answer why it creates a porous structure instead of just dissolving the wafer. There are many different explanations to this phenomenon and the most plausible mechanism seems to be a combination of all of them (see **Fig. 2.3**) **[28]**. The first thing to point out is that the Si-H bonds on a (100) Si surface are strained and are more prone to

dissolution than other surfaces such (111), making the pores propagate in the <100> direction (**Fig. 2.3a**). This propagation is favored by the intense electric field produced at the bottom of the pore due to its curvature radius, producing a h^+ accumulation and thus, a preferential region to the anodization reactions (**Fig. 2.3b**). Another limiting effect is the increased resistance due to thin Si filaments formed in the structure that favor the h^+ injection directly to the electrolyte at the pore bottom, rather than its propagation along the Si structure (**Fig. 2.3c**). In addition, the semiconductor-electrolyte interface plays an important role since the space-charge region depends on the available charge carriers. Thus, if a region is h^+ depleted, the band bending avoids their transport to the interface, limiting the pore formation (**Fig. 2.3d**). Quantum confinement in PS (modelled as Si with a wider bandgap and different electron affinity **[73]**) also plays an important role in the pore formation since the widened bandgap produces a trap for the available h^+ (**Fig. 2.3e**) **[97]**. Furthermore, a low concentration of F^- anions in the electrolyte may result in an oxidation at the bottom of the pore, inhibiting the pore growth and favoring the lateral pore growth (**Fig. 2.3f**) **[98]**.

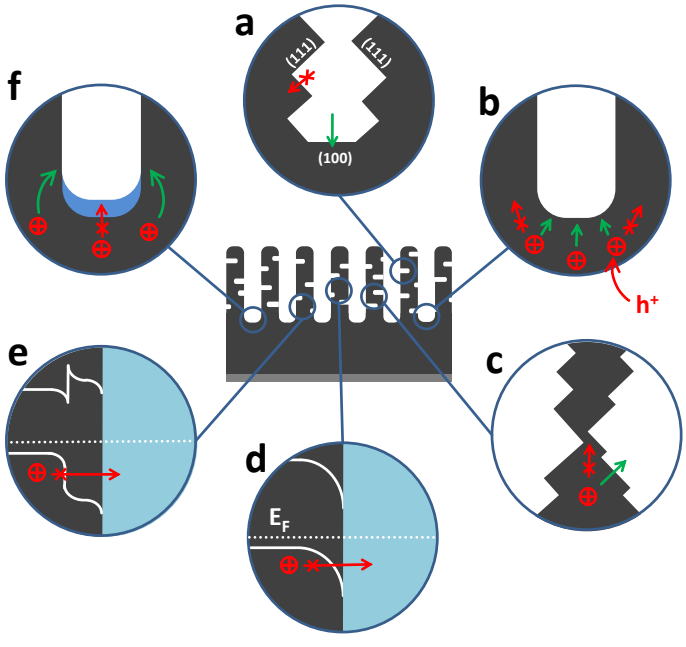

Figure 2.3: Main pore forming mechanisms in PS (adapted from **[28]**).

The main PS properties (morphology, porosity, thickness and pore diameter) depend on the HF concentration, applied current, anodization time, temperature during the synthesis and the wafer characteristics (doping type, resistivity and orientation) **[30]**. These parameters are listed on **Table 2.1**. Although mentioned at the beginning of this section, during this work all samples where produced from p^+-type, B-doped, (100), low resistivity (0.01-0.05 Ω·cm) Si wafers etched in HF:EtOH (1:2) solutions at RT. The specific wafer resistivity and anodization time is mentioned in the experimental part of each system studied. These conditions lead to mesoporous PS (pore diameter between 2 and 50 nm) that contain Si QDs in its matrix to take advantage of its efficient luminescence.

An increase of … yields a	**Porosity**	**Etching rate**	**Critical current**
HF concentration	Decreases	Decreases	Increases
Current density	Increases	Increases	-
Anodization time	Increases	Almost constant	-
Temperature	-	-	Increases
Wafer doping (p-type)	Decreases	Increases	Increases
Wafer doping (n-type)	Increases	Increases	-

Table 2.1: Effects of anodization parameters on PS formation. Adapted from **[30]**.

2.1.2 Synthesis of PS functionalized particles

After the PS synthesis previously described, two more steps are necessary: to convert the PS layer in particles (PSps) and modify their surface with functional molecules: polyethylene-glycol (PEG) or 3-Aminopropyltriethoxysilane (APTS) to form PEG-PSps or APTS-PSps respectively. For clarity, the overall process is schematically depicted on **Fig. 2.4**.

PS particles (PSps) have been formed following the methodology of previous works **[20, 99-101]**. First, mesoporous PS layers were formed as explained in the previous section. Etching time of 1 h and current density of 200 $mA \cdot cm^{-2}$ lead to 300 μm thick PS structures **[54]** (first step shown on **Fig. 2.4**).

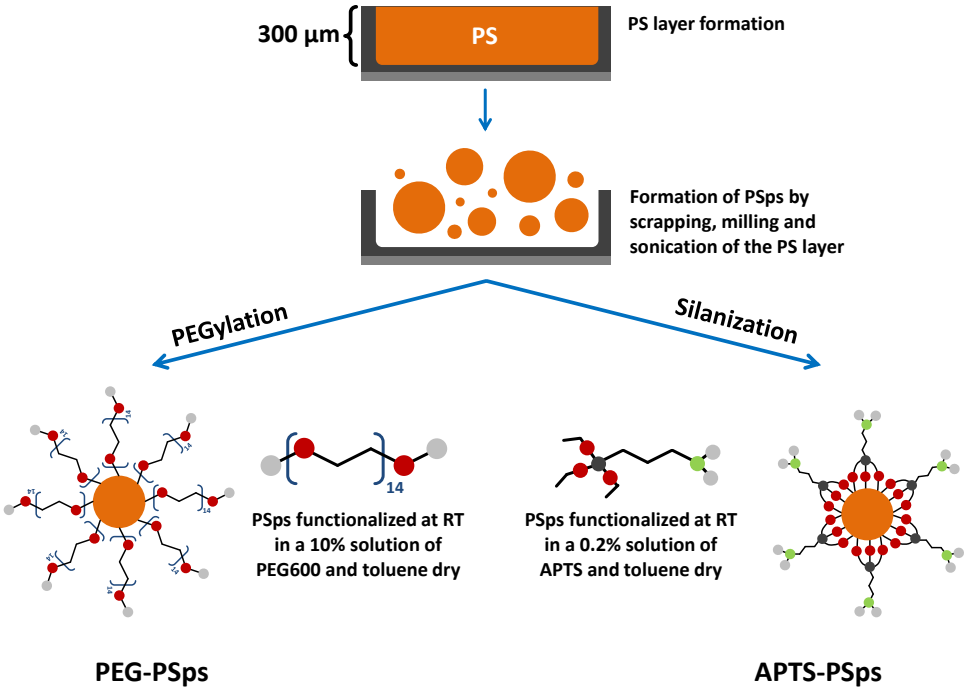

Figure 2.4: Steps followed to the production of APTS-PSps and PEG-PSps.

After a scrapping process followed by a mortar milling step, the PSps are first collected in a toluene dry (Panreac) solution to avoid oxidation and then subjected to 5 min. ultrasound agitation. Due to the extremely high reactivity of the Si-H bonds present at the PS surface after anodization, the PSps start to oxidize during the milling step in air, forming silica (SiO_x, $x \approx 2$) and silanol groups (Si-OH) on the surface **[28, 32, 102]**. These last groups open the possibility of grafting the surface with PEG and APTS molecules by stablishing Si-O-C covalent bonds. The thus ground materials were used to form a colloidal suspension for reaction with solutions of PEG 10% (Mw=600, Fluka) or APTS 0.2% (pur. >98%, Fluka) v/v in toluene dry. These precise concentration for APTS assembly was optimized by reducing the typical concentrations used in bibliography ranging 1 % v/v **[103-105]**. For PEG, the concentrations were based on routes for bonding with Si **[106]**. The surface functionalization with PEG is known as pegylation, while if done with APTS, or other organosilane, it is called silanization.

Pegylation of PSps (PEG-PSps)

PEG is a polymer formed by n ethylene oxide monomers whose chemical formula is $C_{2n+2}H_{4n+6}O_{n+2}$ ($n \approx 14$ in our case). In this molecule, both ends are hydroxyl groups (–OH). One of them is attached to the PSps surface stablishing a covalent bond **[107, 108]** with one of the available Si–OH groups due to its high polarization, producing an H_2O molecule (see **Fig. 2.5**). The other –OH group is free and responsible of the interaction with the biomolecular medium. Synthesis of PEG-PSps is achieved by placing the slightly oxidized PSps in a 10% solution of PEG600 in toluene at RT. After letting the PSps surface react, the PSps were precipitated by centrifugation and changed of toluene medium twice.

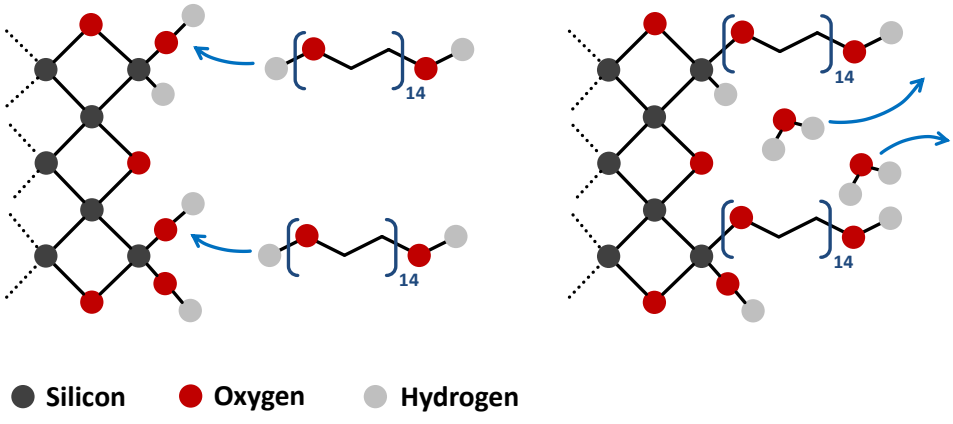

Figure 2.5: Scheme of the PEGylation process at the surface of the PSps.

Silanization of PSps (APTS-PSps)

APTS ($C_9H_{23}NO_3Si$) is an aminosilane formed by one aminopropyl and three ethoxy units linked to a Si atom, producing terminations by one amino and three ethyl groups, respectively. Following previous literature analysis of PS surface modification by APTS molecules **[109]**, the functionalization takes place when APTS is linked by condensation through Si-OH bonds available at the surface of the PSps by producing an ethanol molecule as byproduct. If two chemisorbing APTS

molecules are close enough, two APTS molecules can be linked through an oxygen atom (see **Fig. 2.6**). A slight presence of water molecules extremely facilitates this process (since hydrolysis of APTS increases density of groups that can be potentially condensed). In fact, an excess of water can induce a homogeneous reaction of APTS colloids. In this form, the $-NH_2$ group is free standing on the surface of the PSps and responsible of the interaction with the biological medium, opening the possibility to link to other molecules such as proteins or DNA. Synthesis of APTS-PSps is achieved, similarly to the case of PEG-PSps, by placing the slightly oxidized PSps in a 0.2% solution of APTS in toluene at RT. Again, after letting the PSps surface react, the PSps were precipitated by centrifugation and changed of toluene medium twice.

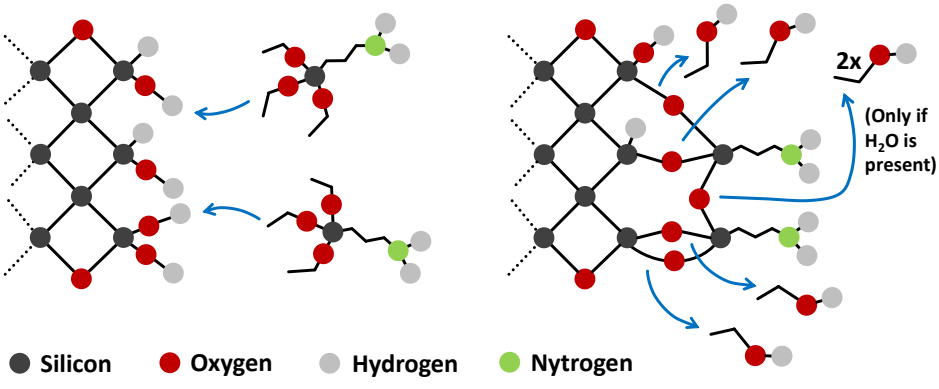

Figure 2.6: Scheme of the silanization process at the surface of the PSps.

2.1.3 Synthesis of PS-ZnO nanocomposites

As in the previous case, the synthesis process can be divided in two parts: the formation of PS layers and its infiltration with ZnO using the sol-gel spin-coating technique (**Fig. 2.7**). PS layers were formed by the electrochemical anodization of p+-type (B-doped), low-resistivity (0.01-0.02 Ω·cm), (100) Si wafers applying a constant current density of 80 $mA \cdot cm^{-2}$ for 30 s resulting in 1.5±0.3 μm thick mesoporous structures.

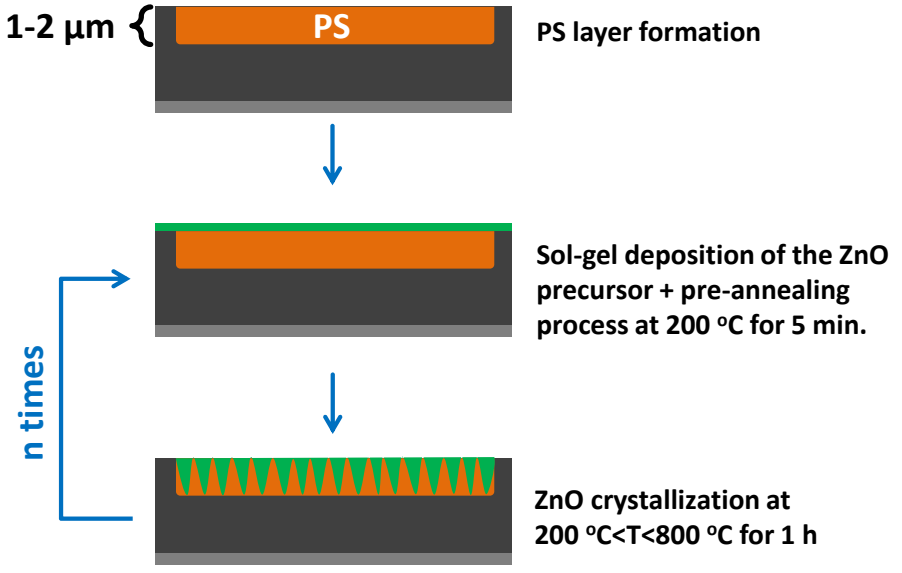

Figure 2.7: Steps followed to synthesize PS-ZnO nanocomposites.

The next step is the permeation of the PS-ZnO structures using a sol-gel spin-coating technique following previously described routes **[65, 110, 111]**. For this study, a 0.2 M solution of zinc acetate dihydrate (ZAD, $Zn(CH_3COO)_2 \cdot 2(H_2O)$, ≥98%, Sigma-Aldrich) diluted in absolute ethanol (Panreac) and monoethanolamine (MEA, with [MEA]=[Zn^{2+}]) was prepared.

There are three nucleophilic species (MEA, OH^- and CH_3COO^-) competing for the Zn^{2+} cations under these conditions (ethanolic solution with MEA as additive, with [H_2O]/[Zn^{2+}]=2) (see **Fig. 2.8**) **[111]**. Hydrolysis and condensation of the Zn^{2+} cations are relatively slow, due to the low quantities of water (provided by ZAD). However, in order to avoid the earlier formation of ZnO particles in the solution, MEA is used as a complexing agent retarding the Zn^{2+} condensation (see **Fig. 2.9**). However, not less important is the role of acetates acting as stabilizer by complexing Zn^{2+} in competition with MEA **[112]**.

The ZAD-EtOH-MEA solution is stirred for 10 hours at 60 ºC under reflux to favor the hydrolysis and stabilize the solution until a transparent sol was obtained. After having the solution prepared, 50 µL are deposited by spin-coating at 2500 rpm

during 30 s over PS. As mentioned before, PS exposed to the atmosphere rapidly oxidizes to form silica SiO_x (x≈2) and Si-OH, which is well known for its hydrophilic character. If the sample stays under an oxidant atmosphere for a long time, the whole surface of PS exhibits a pure SiO_x (x≈2) layer (even all PS can be transformed in silica). Thus, the small PS pores act like small capillaries causing to absorb the solution **[113]** and, by the capillary action, the zinc cations (Zn^{2+}) and hydroxide anions (OH^-) containing water can be easily permeated.

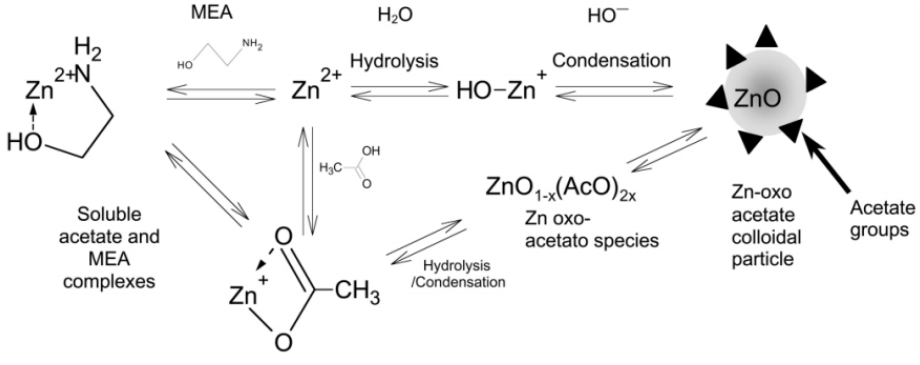

Figure 2.8: Sketch of the possible chemical equilibria taking place in the ZAD-EtOH-MEA solutions (from **[111]**).

After RT condensation, the composites were annealed in a furnace in presence of air at different temperatures between 200 ºC and 800 ºC for 1 hour. This deposition-annealing process was repeated several times (depending on the subsequent analysis or application) to increase the ZnO retention. The thermal annealing turns the gel (**Eq. 2.3**) into ZnO nanocrystals by dehydration reactions (**Eq. 2.4**) **[85]**:

$$Zn^{2+} + 2OH^- \longrightarrow Zn(OH)_2 \qquad \textbf{Eq. 2.3}$$

$$Zn(OH)_2 \longrightarrow ZnO + H_2O \qquad \textbf{Eq. 2.4}$$

However, the chemistry is expected to change for high annealing temperatures when silicate phases can be activated. At high temperatures (around 800 ºC), the annealing in presence of oxygen produces a rapid oxidation of the PS matrix that forms SiO_2:

$$Si(s) + O_2(g) \longrightarrow SiO_2(s) \qquad \textbf{Eq. 2.5}$$

Then, this silicon oxide reacts with the ZnO present along the structure to form silicates as follows **[114]**:

$$SiO_2(s) + 2ZnO(s) \longrightarrow Zn_2SiO_4(s) \qquad \textbf{Eq. 2.6}$$

It is interesting to illustrate the effects of MEA in the solution after the spin-coating process, in which samples synthesized with no complexing agent present ZnO particles. **Fig. 2.9a** shows the pH of a ZAD dissolved in EtOH one month after its preparation. On its right side, there is an optical fluorescence image of a PS sample capped with this solution and annealed at 800 ºC. The formation of ZnO precipitates in the solution induces an inhomogeneous capping. However, if the solution is stabilized with MEA, the pH is notably different after one month and no precipitates are formed, leading to a regular capping as seen on **Fig. 2.9b**.

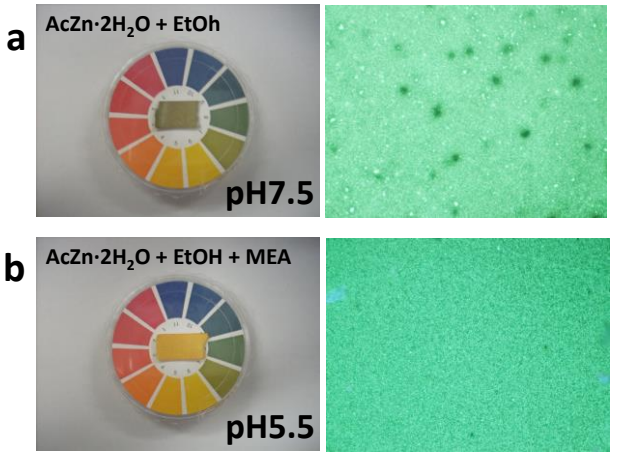

Figure 2.9: Differences between solutions with and without MEA as complexing agent. Both samples where annealed at 800 ºC.

2.1.4 Processing of PS-ZnO electroluminescent structures

Light emitting devices are formed by slight variations of the protocols defined for the formation of PS-ZnO nanocomposites. They are synthesized by the electrochemical anodization of p+-type (B-doped), low-resistivity (0.01-0.02 Ω·cm), (100) Si wafers, although the anodization time was set to 120 $mA \cdot cm^{-2}$ for 90 s resulting in 1.1±0.1 μm thick micro-porous columnar structures. These experimental conditions were determined after a trial-error process with the objective of producing PS layers with enhanced luminescence. The sol-gel spin-coating process was carried out 20 times with pre-annealing steps of 200 ºC for 5 min. in each case to remove the possible initial sol-gel hydrocarbons. Finally, the device is completed by depositing a front transparent indium tin oxide (ITO) contact by electron beam evaporation that is subsequently annealed at 550 ºC for 10 min. to improve its crystallinity. After this thermal treatment, this layer becomes highly conductive ($4.5 \cdot 10^4$ $S \cdot m^{-1}$) with a 70% transmittance over the whole visible range. Once prepared, the sample was cut in 4±0.2 mm^2 pieces for testing in order to avoid current leakage at the ITO-Si edges. The process is depicted on **Fig. 2.10**.

Figure 2.10: Steps followed to finish a PS-ZnO electroluminescent structure.

2.2 Characterization techniques

This section is intended to give a brief description of all the characterization techniques used during this work. Since there is a large amount of characterization techniques and their objectives are specific, they are described by alphabetical order. Special attention is paid in the description of specialized non-conventional techniques. The parameters used in each case are described in the next section.

2.2.1 Energy-Dispersive X-Ray Spectroscopy (EDX)

An electron beam (~10 keV) impinges in a sample interacting with its electrons producing ionization in deep electronic levels. Then, characteristic X-rays are generated when another electron from a higher energy state occupies its state, making possible to determine the elements present in the sample **[115]**. Conventional electron and transmission microscopes usually integrate the equipment necessary to carry out the analysis. In our case, the EDX device used was placed in a TEM. Results from this technique in low dimensional materials should be carefully studied due to the high electron scattering inside the sample that may cause emission from a very large volume beyond the region of interest **[116]**. In addition, modern configurations allow a selective recollection of the signal, which provides compositional maps with relevant information on the distribution of compounds in composite materials **[115]**.

2.2.2 Elastic Backscattering Spectrometry (EBS)

This technique consists in probing a sample with accelerated ions (usually ionized α particles) at high energies (~MeV). Ions interact with the atomic nucleus present in the sample ($X(\alpha,\alpha)X$) and are backscattered at lower energies. The change in energy is proportional to the kinematic factor K **[117]**:

$$E = KE_0, \quad K = \frac{M_1^2}{(M_1+M_2)^2}\left\{\cos\theta \pm \left[\left(\frac{M_2}{M_1}\right)^2 - \sin^2\theta\right]^{1/2}\right\}^2 \qquad \textbf{Eq. 2.7}$$

where E and E_0, are the backscattered and incindent energies of the ions, θ the scattering angle and M_1 and M_2 the ion used to probe the sample and the element from the sample with which it interacts. Each interaction has a characteristic energy and thus, the unknown element present in the sample can be identified. In addition, the concentration of an element can be also calculated since it is proportional to the number of its atoms present in the sample and their cross section. In contrary to Rutherford Backscattering Spectrometry (RBS), EBS uses resonant energies that are higher enough to enter the coulomb barrier of the nucleus. In this case, the cross section of the element needs to be calculated, not by the Rutherford's

approximation to the particle dispersion, but using the Schrödinger's equation. Due to its complexity, these cross section values are experimental **[118]**.

EBS, as well as RBS, is useful to determine the in-depth composition of a sample, as well as its thickness, since ions can reach several microns inside the material depending on their incident energy and the sample properties (i.e. composition, density, homogeneity or isotropy) **[119]**.

2.2.3 Electroluminescence (EL)

This technique uses an electric field along the sample to inject current in the material under test. The recombination of electrons in available states (holes) releases photons (luminescence). EL is influenced by a number of factors such as the optical properties of the structure/structures studied and thus, information about its band structure and emission mechanisms can be obtained **[120]**. However, it is required from the sample to have adequate ohmic contacts in order to inject the current in the structure without junction effects. To register the signal, a monochromator is placed between the polarized sample and the detector so that intensity is registered as a function of the wavelength.

2.2.4 Fluorescence optical microscopy

A fluorescence microscope is an optical microscope with a high intensity light source (100 W Hg lamp in the microscope used) capable of exciting fluorescent samples. To collect selected wavelengths, these microscopes incorporate a series of band pass filters. The resulting images correspond to the radiative transitions that take place in the sample in the different wavelengths (colors). Generally, there is the possibility of using three different filters to obtain the fluorescence in different bands (red, green and blue). For this work, since the samples studied (functionalized PSps and PS-ZnO nanocomposites) show a very broad photoluminescence, the image was registered by filtering only the scattered light from the UV source, observing the whole luminescence.

2.2.5 Grazing-Incidence X-ray Diffraction (GIXD)

When monochromatic X-rays impinge upon the atoms of a material, they are scattered by electrons. If the material has a periodic structure, the scattered X-rays undergo constructive and destructive interference registered as a function of the diffraction angle (2θ) constituting the X-ray diffractograms. This phenomenon is described by Bragg's Law **[121]**:

$$n\lambda = 2d_{hkl}\sin\theta \qquad \textbf{Eq. 2.7}$$

where n is the diffraction order ($n=1$ in this case), λ is the X-rays wavelength used (Cu-Kα, λ =1.5405 Å), and θ the diffraction angle. The peak intensities are determined by the distribution and nature of the atoms within the lattice **[121]**.

In this work, grazing-incidence X-ray diffraction (GIXD) configuration has been used. The difference between conventional X-ray diffraction (XRD) and GIXD lies in the measurement setup, since the impinging X-rays are fixed at a very small angle so that diffraction can be made more surface-sensitive. Therefore, it is a technique specially adapted to the characterization of thin film systems. Both XRD and GIXD are used to characterize crystalline or polycrystalline materials, providing information about their structure, effective crystallite size, lattice strain, phases present in the material, preferential orientations and defects **[121]**.

2.2.6 Photoluminescence (PL)

Electrons are photo-excited by exposing the sample to a light source. For most materials, a de-excitation to a lower energy state is induced by emitting photons that produce the PL spectrum. This spectrum is usually obtained registering the light coming from the sample through a monochromator, so that its intensity can be recorded as a function of its wavelength. In this device, one should be careful to avoid exposure of the detector to the excitation light reflected on the sample surface, whose emission peaks can distort the PL spectra. Particularities in the radiative recombination (i.e. phosphorescence, allowed and forbidden states,

phonons, plasmons) are not discussed here, but are treated in detail in the bibliography **[122]**.

PL is principally used to determine the optical properties of a material and should be distinguished from EL, since the different emission mechanisms could also result in huge emission wavelength/intensity changes.

2.2.7 Scanning Electron Microscopy (SEM and FESEM)

This technique uses a fine beam of accelerated electrons (~10 keV) to scan a sample while a detector registers the secondary electrons intensity emitted that varies along the surface depending on its orientation and composition, producing a high-resolution 2D image with long depth of field **[116]**.

The difference between SEM and Field-Emission SEM (FESEM) lies in how electrons are produced. The former uses a filament made of tungsten (W) from which electrons are generated by thermionic effect. The latter uses a field-emission cathode that provides narrower probing beams, at low as well as high electron energy, resulting in clearer, less electrostatically distorted images with improved spatial resolution **[116]**.

2.2.8 Transmission electron microscopy (TEM)

Although it uses electrons like SEM techniques, TEM images are produced from primary electrons that are able to cross the sample. These electrons accelerated at high energies (~100 keV) have very short De Broglie wavelengths, comparable to the interatomic distance in a crystal. For this reason, TEM microscopes reach extremely high magnifications, even to resolve single atoms **[116]**. However, it usually requires a careful sample preparation, especially in the case of thick ones that need several steps to reduce its cross section **[123]**.

Apart from EDX, as discussed previously, this technique incorporates also the possibility of obtaining diffraction patterns by taking advantage of the electrons' wave nature. This allows the identification of crystalline structures and phases in single nanocrystals. A particular mode for this diffraction receives the name of Selected Area Electron Diffraction (SAED).

2.2.9 Ultraviolet-Visible Spectroscopy (UV-Vis)

This spectroscopy is used to quantify the light absorbed, reflected or transmitted in a sample. For this purpose, it uses UV and visible light (even near-infrared) to excite the sample. It is widely used in chemistry providing information about the functional groups present in structures, as well as the determination of the concentration of a molecule in a solution through its absorption of light (extinction coefficient) **[122]**. However, in our case the interest of this technique applied to thin film analysis is focused on determining the transmission of ITO films and the ZnO band gap. In the case of the latter material, there are some drawbacks since in this work 300 μm thick Si samples are used and thus, reflectance is the only way to determine the band gap value (i.e. no transmission signal available).

2.2.10 X-ray absorption spectroscopy (XAS)

XAS is a non-destructive technique based on the absorption of X-rays close to the energy of a determined orbital from a specific atom promoting electrons from that energy level to the vacuum. Although there are different measuring methods in XAS (i.e. absorption, total electron yield and fluorescence) we focus exclusively in fluorescence herein. In this case, the absorption spectra is obtained by the existing relation between the X-rays initial intensity (I_0) and the one produced by the de-excitation (dipolar transitions) to the unoccupied states produced by photoemission (I_f) as follows **[124]**:

$$\mu \propto \frac{I_f}{I_0} \qquad \textbf{Eq. 2.8}$$

A full XAS scan has two zones: XANES (X-Ray Near-Edge Structure) and EXAFS (Extended X-ray Absorption Fine Structure). The separation between them depends on the interatomic distances and the X-rays wavelength used to the study (considering the excited electrons as spherical waves, they will suffer interaction when its wavelength is in the order of the first neighbors).

On the one hand, XANES gives information about the local structure around the absorbing atom as well as the oxidation state and bonding characteristics. This

part of the spectrum doesn't have a concise mathematical formulation and results more qualitatively than quantitatively **[124]**.

On the other hand, EXAFS is useful to determine the interatomic distances (R), sample structure disorder (mean-square disorder or Debye-Waller factor, σ^2) and coordination number (N). In contrary to XANES, it has a very precise mathematical background where electrons are modelled as spherical waves scattered in a periodic structure suffering constructive and destructive interferences that allow calculating the mentioned structural parameters through the EXAFS equation:

$$\chi(k) = \sum_{\forall j} \frac{N_j f_j(k) e^{-2k^2\sigma_j^2}}{kR_j^2} \sin[2kR_j + \delta_j(j)] \qquad \textbf{Eq. 4.8}$$

where subindex j refers to the j'th electron scattering path, $f(k)$ and $\delta(k)$ are theoretical scattering properties, and k is the photoelectron wavenumber.

2.2.11 X-Ray photoelectron Spectroscopy (XPS)

This non-destructive technique allows studying quantitatively the elemental composition of a sample, its empiric formula and the chemical and electronic states of the elements present. It uses monochromatic X-rays with energy E_γ, to excite a sample and register the kinetic energy (E_K) of the photoemitted electrons and their number, obtaining information about the particular binding energy (E_{bin}). They are related by the following equation **[125]**:

$$E_K = E_\gamma - E_{bin} - \phi \qquad \textbf{Eq. 2.9}$$

where ϕ is the work function (energy required to remove electron from sample to vacuum). Since electrons are required to escape from the sample to the vacuum, XPS provides information only from the surface of the sample (around tens of Å). When plotting the intensity of photoemitted electrons (related with its concentration) versus their binding energy, different peaks related to specific elements are observed (each element will show different XPS peaks corresponding, if the case, to the 1s, 2p, etc. levels). Since registered photoelectrons come from

external orbitals, including valence band if desired, this spectroscopy is, not only quantitative, but also extremely sensitive to chemical shifts induced by the more or less oxidative environment of a particular element **[126]**.

2.3 Sample characterization

After describing the different techniques used during this work, the details on the sample characterization for the systems studied are shown below.

2.3.1 Functionalized PSps

For the morphological characterization, sediment of the PSps on a Ta foil (with no surface metallization step) was analyzed in a Hitachi S-3000N scanning electron microscope (SEM) with conventional thermionic filament and operation voltage set at 20 keV.

X-ray photoelectron spectroscopy (XPS) was used for the surface characterization of the PSps after modification and medium exchange and dispersion onto mirror polished Ta substrates. XPS measurements (survey and high resolution) were obtained by using an Ultra photoelectron spectrometer XPS (KRATOS Analytical) with a monochromatic Al-Kα source. The spectra were obtained at 90º take-off angle and pass energy of 20 eV. Surface charge was compensated by magnetic immersion lenses and all peak energies were referred to the binding energy (BE) of the hydrocarbon peak at 284.6 eV. Peak fitting after a Shirley background subtraction with a G/L function (30/70) was done by using Vision 2 software (Kratos) and casaXPSv2.3.15 (Casa Software Ltd., UK).

Photoluminescence (PL) measurements were performed in a cuvette containing 500 µl PSps-toluene solutions with a SLM Aminco AB2 luminescence spectrometer. Excitation light was provided by a Xe lamp, monochromatized at 420 nm with a 2 nm bandwidth. Emission spectra were monochromatized with a 4 nm bandwidth and detected with a photomultiplier tube operated at 800 V.

Fluorescence images from PSps on Si surfaces were obtained in an inverted microscope Olympus IX81 linked to a digital camera DP72 controlled by cellD software. The excitation source of this device was a 100 W Hg lamp operating at stabilized direct current, suitable for UV fluorescence.

2.3.2 PS-ZnO nanocomposites

The morphology of the samples was studied by electron microscopy using a Philips XL-40 FEG Field-Emission Scanning Electron Microscope (FESEM) operated at 10 kV using its through-the-lens (TLD) detector. The cross-sectional images shown were obtained without any previous metallization. High Resolution Transmission Electron Microscopy (HRTEM) was carried out using a Hitachi H9000NAR microscope (300kV, LaB6, point to point resolution=0.18 nm). The energy-dispersive X-ray spectra (EDX) were obtained by using a Kevex Super-Quantek Si–Li detector. Diffraction patterns were obtained using selected area electron diffraction (SAED). Cross section samples were prepared by the tripod method and ion beam milling in a Gatan PIPS system until an electron transparent area was obtained **[123]**.

Evolution of the crystalline structure upon annealing was determined using a Siemens D5000 HR diffractometer in the Grazing-Incidence X-ray Diffraction configuration (GIXD) using Cu-Kα radiation (λ=1.54 Å). In order to increase the signal from the layer, the analysis was performed at a fixed angle of 0.5º from 2θ=15º to 2θ=70º with increments of $\Delta\theta$=0.04º (accumulation time of 10 s). The crystallite size has been calculated using the Scherrer formula **[121]** with the spherical particle approximation $L = 0.9\lambda/(\beta_{2\theta}cos\theta)$ where L is the average grain size, λ the X-rays wavelength, $\beta_{2\theta}$ the full width at half maximum of the peak and θ its diffraction angle.

Elastic (non-Rutherford) Backscattering Spectrometry (EBS) technique was useful to study in detail the in-depth composition. Due to possible differences in the O and C concentrations after the annealing, the analysis was performed at O- and C-resonant energies using 3.035 and 4.26 MeV helium ($^4He^+$) ion beams. Backscattered He ions were detected using a surface barrier blind detector with an

active area of 50 mm^2, placed at a scattering angle of θ=170.4º from the probe beam. Each data set was obtained depositing a charge of 20 μC, which corresponds to a particle density of $5.49 \cdot 10^{11}$ part·sr. Beam current was stabilized at 17±2 nA. Data sets were fitted using SIMNRA 6.05 software **[127]** (oxygen non-Rutherford cross-section used was Cheng et al. 1993A **[128]** and carbon non-Rutherford from Leavitt et al. **[129]**).

XPS measurements and analysis were performed to study in detail the surface chemistry using the same equipment and methods as described for the characterization of PSps.

Extended X-ray Absorption Fine Structure (EXAFS) was used to study the Zn local structure of the ZnO nanoparticles (Zn K-edge at 9.659 keV). The experiments were performed at the BM-25A beamline (5-35 keV) placed at the European Synchrotron Radiation Facility (ESRF). The fluorescence signal was registered with a 13-element Si(Li) detector from e2v Scientific Instruments with the sample placed at 45º. During the measurements, a metallic thin film was used to set and calibrate the energy incoming from the monochromator. Each sample was compared with a pure ZnO powder sample. All data sets were processed by the Demeter software pack (v0.9.20) that contains FEFF code **[130]**, which is an automated program for *ab-initio* multiple scattering calculations **[131]**. All XAS measurements were carried out at the synchrotron radiation facility (ESRF) in Grenoble (France), specifically in BM25A branch.

Photoluminescence (PL) has been measured using a luminescence spectrometer (Aminco Bowman series 2) operating with a 150 W continuous wave Xe lamp. Samples were excited with wavelengths between 350 and 400 nm in order to excite the different energy levels formed in the nanocomposite. Signal was recorded using a photomultiplier tube detector polarized at 500 V. The emission scan was performed between 475 and 675 nm, avoiding the second harmonic diffraction peak from the excitation wavelength. Luminescence from different samples was observed directly by fluorescence microscopy using the same equipment as for observation of PSps.

Finally, UV-Vis spectra were measured by using A Jasco V-560 spectrometer using the reflectance configuration. The reflected light from the sample was collected in an integrating sphere made of highly reflective $BaSO_4$. Before measurements, the device was calibrated by closing the integrating sphere with a piece of the same reflective material to measure the baseline. The reflectance spectra were expressed as absorbance by using the Kubelka-Munk transformation. Band gaps were calculated using Tauc plots assuming a direct band-gap for ZnO.

2.3.3 PS-ZnO electroluminescent devices

In this case, sample morphology was studied by electron microscopy using a Philips XL-40 FEG Field-Emission Scanning Electron Microscope (FESEM) operated at 10 kV using its through-the-lens (TLD) detector. J-V characteristics where measured using a TTi PL303QMD Quad-Mode Dual power supply which was also used to forward-biasing the device at 10 V to measure the EL spectra between 300 nm and 800 nm using the photomultiplier detector polarized at 250V from the same Aminco Bowman series 2 luminescence spectrometer used to characterize the PL from the PS-ZnO nanocomposites.

CHAPTER 3:

PS functionalized particles

This chapter presents the results from the analysis of APTS- and PEG-modified porous silicon particles (APTS-PSps and PEG-PSps) with regard to their morphology, surface chemistry and photoluminescence. The content of this chapter is complemented by a subsequent work concerning the biocompatibility of these modified PSps (improved with Fe/Co magnetic nanoparticles embedded in the PS matrix) **[132, 133]**. Results from that study were discussed in detail in a previous thesis **[134]**. All details about the particles synthesis and functionalization were described in detail on **Chapter 2**.

3.1 Particle morphology

The key aspects of the particle morphology are their shape, size and agglomeration state. It can be observed in the scanning electron microscopy (SEM) images at **Fig. 3.1a** that most particles are dispersed and show a regular and spherical shape after any of the two different functionalizations studied (APTS or PEG). Therefore, particle size can be described in both cases by measuring the diameter (ϕ), obtaining a size distribution (**Fig. 3.1b**). From these plots, some useful statistical values can be derived, such as the mean, median and mode of the distribution. However, it is helpful to report the cumulative distribution function (CDF) from which percentiles can be easily derived. Percentiles P10, P50 and P90 tell us the percent of particles (10%, 50% and 90% respectively) whose diameter is below a certain value, making the interpretation of the plot more intuitive. All these statistical values derived from the size distribution are reported in **Table 3.1** for both APTS-PSps and PEG-PSps.

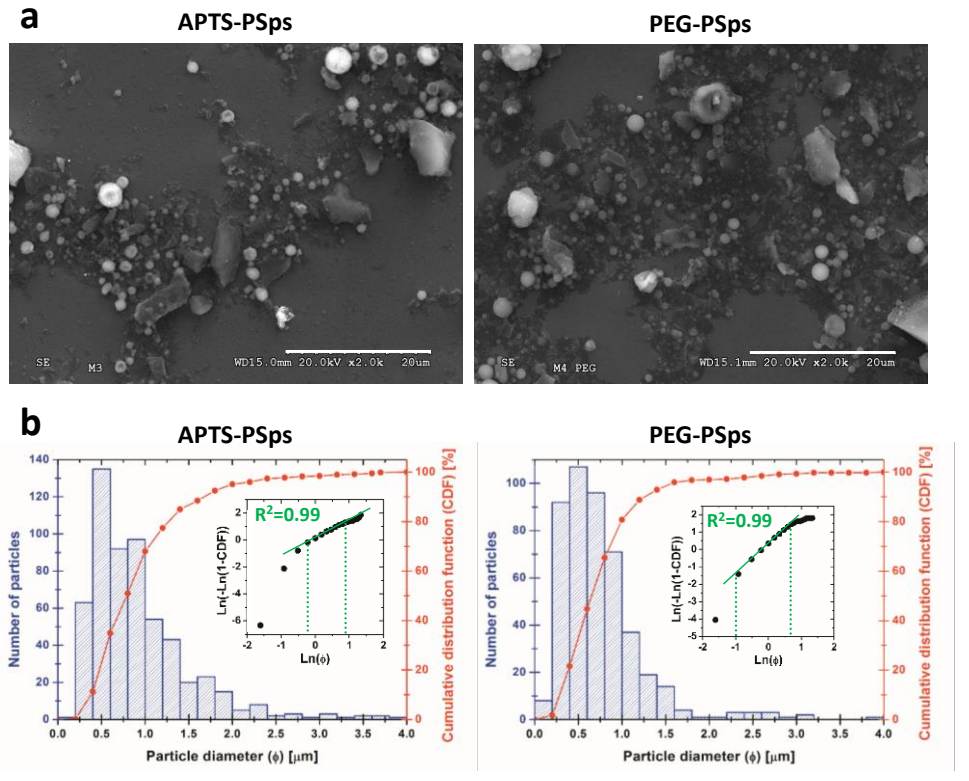

Figure 3.1: FESEM images from APTS- and PEG-PSps standing on a polished Si surface (**a**) and their corresponding size distribution (blue histogram) plotted together with the cumulative function, CDF (red line + dots) (**b**). The graph insets correspond to the Weibull plots in which the green continuous lines are the lineal fits.

	# particles	Mode	Median	Mean	P10	P50	P90
APTS-PSps	571	0.52	0.79	0.92	0.38	0.79	1.68
PEG-PSps	467	0.54	0.65	0.78	0.28	0.65	1.26

Table 3.1: Statistical results obtained from the size distribution (in blue) and the cumulative function (in red) plotted on **Fig. 3.1b**. Data is given in microns (μm).

The statistical study was carried out from 571 and 467 particles for the APTS- and PEG-PSps respectively. In both functionalization processes, the shape of the size distribution function is very similar (**Fig. 3.1b**). However, although the mode indicates that most of the particles have sub-micrometric sizes (ϕ=0.5 μm), the

mean and the median are larger in the case of the APTS-PSps, with values close to the micron. This observation can be due to the linkage of small colloidal particles through APTS molecules as proposed on **Fig. 3.2** (the way these molecules stablish covalent bonds between them and the PSps surface was discussed on **Chapter 2**). In fact, by looking at its size distribution, there is a negligible number of APTS-PSps found with diameters between 0.0-0.2 μm in contrast to those with sizes between 0.4-0.6 μm, suggesting that the smaller particles present in the colloid may tend to condense in larger ones as previously described in the case of silica particles **[89]**.

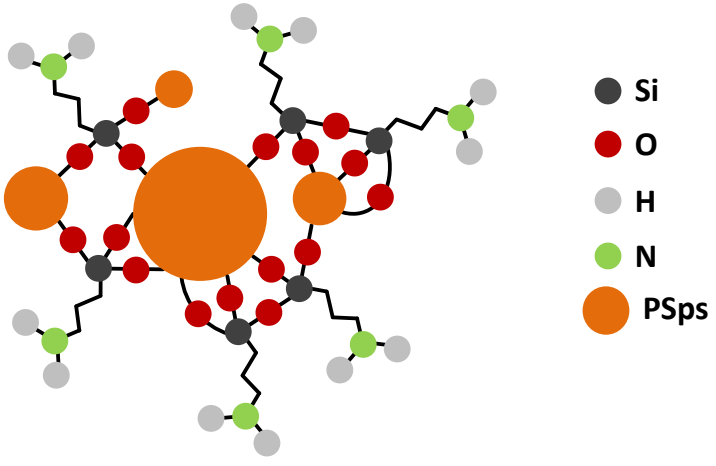

Fig. 3.2: Proposed mechanism to the PSps linkage through APTS molecules.

The CDF plotted together with the size distribution function can be used to study the particles from another point of view. On the one hand, percentiles P10 and P90 from the APTS- PSps indicate that 10% of them have diameters below 0.38 μm, while 90% are below 1.68 μm. On the other hand, in the case of PEG-PSps these values are 0.28 μm and 1.26 μm for P10 and P90 respectively. Thus, it is another way to show that there are larger particles in the case of the APTS modification. Nevertheless, percentile P50 is mathematically identical to the value given by the median but it has been shown for completeness.

Returning to the shape of the particle size distribution, we need to take into account that these particles are synthesized by scrapping PS films, followed by

milling and ultrasound steps. In fact, these processes usually give rise to a particle population that fits to a Rosin-Rammler distribution **[135]** (also known as Weibull distribution) which is given, in this case, by:

$$CDF = 1 - e^{-(\phi/a)^b} \qquad \textbf{Eq. 3.1}$$

In this equation, a and b are the scale and shape parameters respectively. Taking two times the natural logarithm, a linear plot is expected when plotting $\ln(-\ln(1 - CDF))$ vs. $\ln(\phi)$. In fact, the linear fits (with R^2=0.99) performed on the Weibull plots indicate that both distributions show a linear behavior for the following sizes: 0.7<ϕ(μm)<2.5 and 0.4<ϕ(μm)<2.2 for the APTS- and PEG-PSps respectively (**Fig. 3.1b**). The reason why larger particles do not follow this trend is that they precipitate faster and thus, they are not efficiently collected by the pipette used to prepare the samples. However, the most noticeable difference between both plots is observed for smaller particles, in which its non-lineal behavior is more pronounced for sizes under 0.7 μm, as a result of the lack of particles under this size. The same occurs for the PEG-PSps, but to a lesser extent (under 0.3 μm).

3.2 Surface characterization

The surface chemical composition of PS and the modified PSps was analyzed by X-ray photoelectron spectroscopy (XPS) to verify the capping induced by APTS and PEG. Elements detected included O, C, Si and F (see **Table 3.2**).

The most relevant information from this analysis is that the surface of the PSps is intensively oxidized to the point of almost reaching 87 at% after PEG modification. In fact, by comparing with a published reference related to the oxidation of PS layers after APTS or PEG modification, it was confirmed that the composition of the particles contained more O and less C than the as-prepared PS particles **[87]**. It is also relevant that the C composition is higher than 9 at% for every type of PSps, whether this C is bound or not to APTS or PEG. On the other hand, concentrations lower than 4.6 at.% of F species appeared, possibly as a trace of F ions remaining trapped inside the pores after the electrochemical etching and subsequent functionalization processes.

Sample	O	F	C	Si
PS	60±1	3.8±0.5	22±1	15±2
APTS-PSps	59.4±0.5	4.6±0.3	12.6±0.7	23.3±0.7
PEG-PSps	87±1	3.8±0.4	9±1	0.7±0.1

Table 3.1: Surface elemental composition of the APTS (in at%).

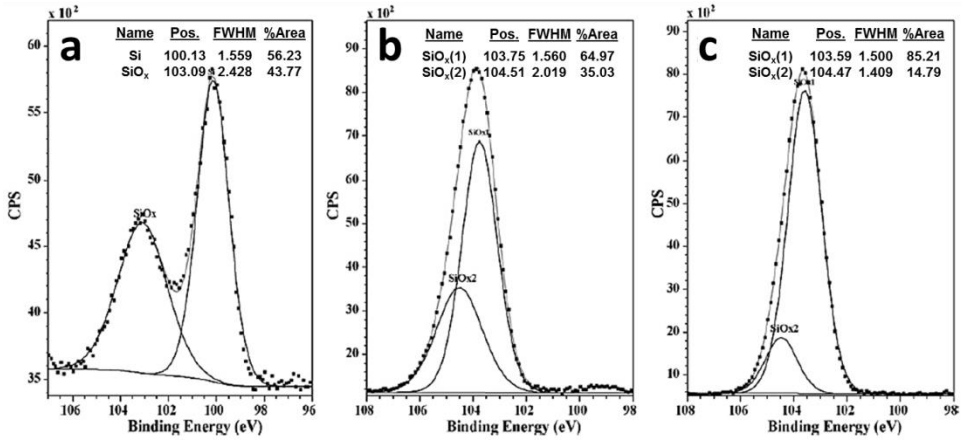

Figure 3.3: XPS core level Si-2p spectra corresponding to as-prepared PSps (**a**), APTS-PSps (**b**) and PEG-PSps (**c**). Insets in all graphs give the values of the peak position, full width at half maximum and relative area of the peak components.

However, the most relevant aspect concerning the Si and C signals emerges from the corresponding high resolution Si-2p and C-1s spectra. The Si-2p spectra presented in **Fig. 3.3** show that the chemical state of the exposed Si surface is considerably different in the modified PSps with respect to the original. As-prepared PSps present two contributions with a dominant component from elemental Si–Si at circa 100 eV (**Fig. 3.3a**) while the spectra corresponding to APTS-PSps (**Fig. 3.3b**) and PEG-PSps (**Fig. 3.3c**) show exclusively components related to oxidized Si, which are integrated herein as SiO_x at circa 103.5 eV **[13]** and suggesting a combined composition of Si−OH and SiO_2.

Regarding the high resolution C-1s component in **Fig. 3.4**, an insight into the capping functionality of the PSps can be obtained. Unmodified PSps present the characteristic C-1s spectrum of semiconductor surfaces exposed to atmospheric conditions. Thus, the electrochemically etched Si (**Fig. 3.4a**) presents a dominant C−C component at 284.6 eV and lower intensity peaks related to C−C−O (about 286.6 eV), O−C−O (about 287 eV) and O=C−OH (about 289.0 eV). The spectrum corresponding to APTS-modified PSps changes considerably with respect to the one of untreated PSps (**Fig. 3.4b**). The most relevant observation is that a new contribution appears related to C−N bonding in the aminopropyl groups from APTS at approximately 286 eV **[89]**. The contribution related to C−O increases and emerges as a shoulder, as expected for high concentrations of unreacted ethoxy groups in APTS. On the other hand, O−C−O and O=C−OH contributions appear clearly weakened in this spectrum with respect to the reference one. Finally, with regards to the modification with PEG, the C-1s high resolution spectrum (**Fig. 3.4c**) clearly indicates an increased intensity for C−O contributions emerging from the PEG chain $(-CH_2-CH_2-O-)_n$ with $n \approx 14$ **[89]**. Other relevant aspects from the spectrum are the partial alkyl contribution to the surface composition (clearly lower than the corresponding to C−C−O) and the peaks from O−C−O and O=C−OH that, in these samples, appear with lower overall contribution than those observed after APTS modification.

To conclude this section, XPS analysis of the C-C-O component can be used as a preliminary instrument to predict the antifouling character of PEG-like materials. In this regard, a good antifouling behavior can be foreseen in the case of PEG modified PSps, since over 50% of the total carbon signal correspond to the C-C-O contribution.

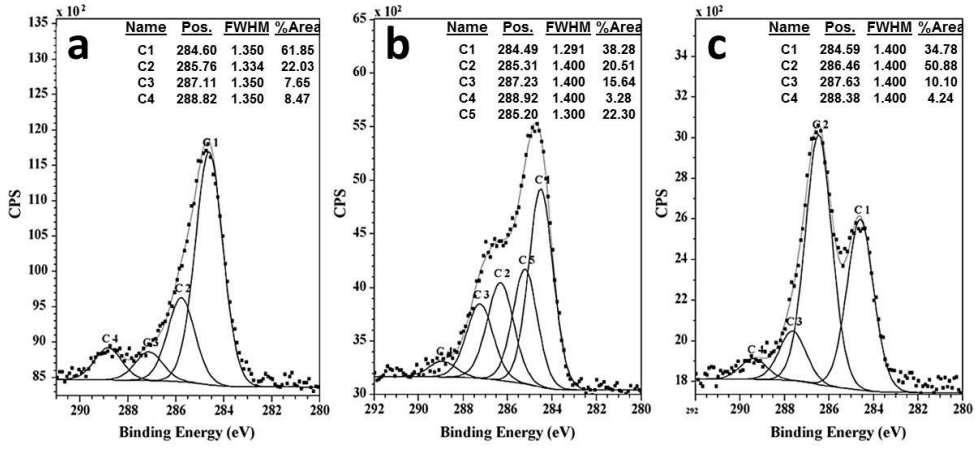

Figure 3.4: XPS core level C-1s spectra corresponding to as-prepared PSps (**a**), APTS-PSps (**b**) and PEG-PSps (**c**). Insets in all graphs give the values of the peak position, full width at half maximum and relative area of the peak components.

3.3 Photoluminescence

Photoluminescence (PL) of the APTS-PSps and PEG-PSps were measured in order to study their viability as fluorescent tags. PL spectra of fresh APTS- PSps and PEG-PSps are depicted in **Fig. 3.5a**, showing the typical broadband visible emission of PS due to quantum confinement **[13]**. Emission is centered at 1.86 eV (667 nm) and 1.92 eV (646 nm) for the APTS and PEG modifications respectively. Despite the shift in the PL signal, both wavelengths might be defined as an orange-red color, as evidence in **Fig 3.5b**. This image corresponds to a fluorescence image of the PSps after PEG modification obtained by using conventional fluorescence optical microscopy equipment and evidences the characteristic red-orange emission of PS originated in particles with different degree of agglomeration induced by the drying process. The smallest isolated spots present dimensions that are in agreement with the sizes of individual particles observed in SEM images (**Fig. 3.1a**). The same result is obtained in the case of APTS-PSps, as suggested on **Fig. 3.5a**.

It is important to notice that neither PEG nor APTS introduce contributions to the PL, but rather a slightly shift and quench of the luminescent properties of the PSps in their lifetime along several days. However, PL of as-formed PSps rapidly quenches due to aging effects (in fact, it is almost extinguished after 24 h), making

them unsuitable for tagging purposes. Nevertheless, modified PSps show a considerably more stable PL. **Fig. 3.5c** shows the evolution of PL of APTS-PSps and PEG-PSps immersed in toluene for several days.

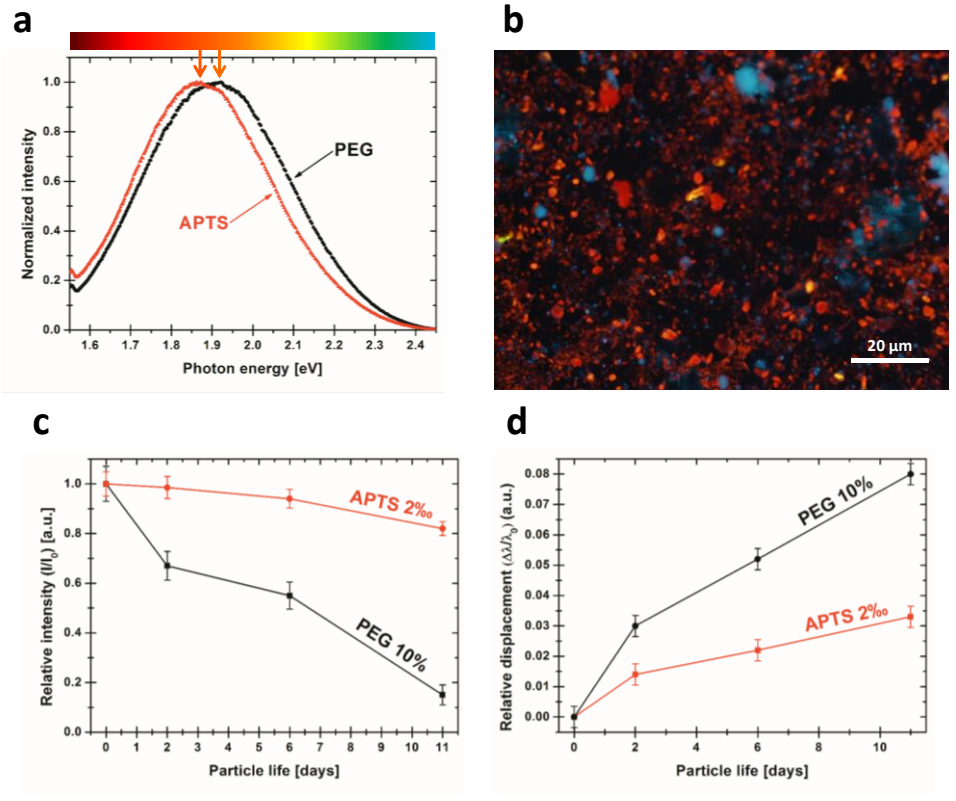

Figure 3.5: (**a**) photoluminescence spectrum of PEG-modified PSps in toluene obtained by using an excitation wavelength of 420 nm. (**b**) Fluorescence microscopy image of PEG-capped PSps, showing red-orange luminescent PSps (blue regions correspond to silica dust). (**c**) Evolution of the PL intensity (I) normalized to the initial intensity (I_0). (**d**) Redshift normalized to initial position (taken as the origin) for both APTS- and PEG-modified PSps.

As it can be observed, APTS-modified PSps retain more than 80% of its PL after 10 days. In contrast to this behavior, the PL of the PEG-modified PSps is quenched to half its initial intensity after one week. Modification of PL stability with PSps life could be also related to the shift induced in the PL emission maxima as illustrated in **Fig. 3.5d**. This wavelength drift is smaller in the case of APTS capping than in the case of PEG capping, with a redshift of 3.2% in the former case, and 8%

in the latter, after 11 days. This difference may be attributed to a more complete isolation of PSps by APTS than that achieved by PEG as suggested by the higher SiO_x contribution in XPS spectrum corresponding to APTS. This higher efficiency in surface coverage translates into an improved chemical stability of the PSps. Thus, it is possible to state that the higher the quenching effect induced by aging, the higher the orange to redshift induced.

CHAPTER 4:

PS-ZnO nanocomposites

This chapter compiles the results obtained from the study of PS-ZnO nanocomposites. Although this system has been previously studied principally by electron microscopy **[44, 69, 71, 84, 85, 136]**, X-ray diffraction **[44, 71, 77, 84, 85, 136]** and photoluminescence **[62, 69, 70, 77, 85]**, new aspects are reported by these techniques in this work. However, the most relevant results are those focused on the nanocomposites' fine structure changes due to the annealing temperature in presence of oxygen, using advanced ion and X-ray techniques such Elastic Backscattering Spectrometry (EBS) and X-ray Absorption Spectroscopy (XAS). Finally, the overall conclusions are itemized at the end of the chapter.

4.1 Sample morphology (SEM)

The structure of the PS-ZnO nanocomposites has been studied by FESEM, which is able to resolve the structure details. **Fig. 4.1** shows cross-sectional images of PS-ZnO samples annealed at 600 ºC (**a**) and 800 ºC (**b**). Both samples show a ~1.5 μm thick PS layer where ZnO has permeated the columnar structure to form the nanocomposite. **Fig. 4.1a** reveals that PS columns propagate during etching along the [100] direction as expected from the etching of highly-doped p^+-type (100) Si wafers **[27]**. The size of ZnO nanoparticles formed inside the PS structure is limited by the pore diameter. Moreover, the distribution of ZnO nanoparticles along the pore is homogeneous. In addition, both figures show larger crystals formed at the surface, where no constrains for crystal growth are induced by pore walls. It is worth remembering that as-prepared PS has a very large internal surface covered by

highly reactive Si-H bonds which is rapidly oxidized when exposed to the atmosphere **[28, 30-32]**. Thus, the incorporation of O atoms forms silica (SiO_2), increasing the PS volume. This process is enhanced when PS is annealed at high temperatures, which is clearly noticed in the marked changes observed in the sample annealed at 800 ºC. Specifically under these experimental conditions, both layer thickness and pore walls became larger compared to the samples annealed at 600 ºC. The original columnar structure of the pore along the [100] direction is not well defined (as seen in detail on the graph inset) due to the formation of SiO_2 at high annealing temperatures and a new α-Zn_2SiO_4 phase (see **Fig. 4.2** and the discussion about X-ray diffraction), which also contributes to the lattice expansion. Therefore, all together induce significant structural changes in the samples annealed at 800 ºC.

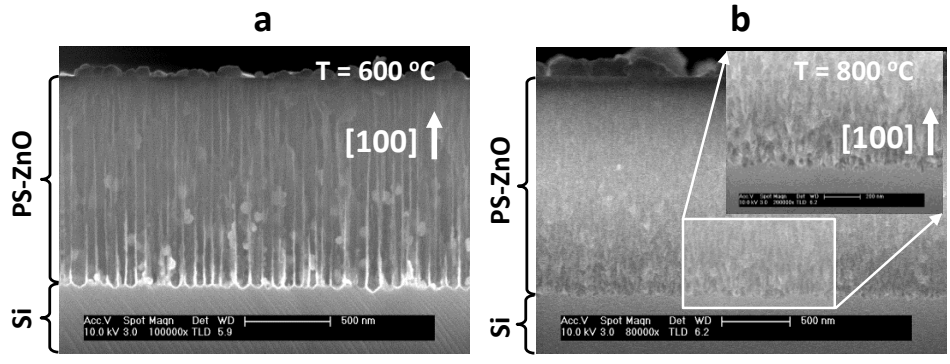

Figure 4.1: Cross-sectional FESEM images of the PS-ZnO samples annealed at 600 ºC (**a**) and 800 ºC showing a detail from the bottom of the pores as an inset (**b**).

4.2 Crystalline structure (GIXD)

For a more detailed analysis of the crystalline structure and the possible changes induced due to the annealing process, X-ray diffraction technique was used. Taking into account that the PS-ZnO nanocomposites are thin films synthesized on 300 μm thick (100) Si wafers, grazing-incidence X-ray diffraction configuration (GIXD) was used in order to maximize the surface information.

The X-ray diffractograms obtained from PS-ZnO samples annealed between 200 ºC and 800 ºC are shown in **Fig. 4.2**. Samples annealed at 200 ºC shows no

distinguishable ZnO peaks due to the absence of long-range order in the first formation stages. However, a sharp peak centered at 56.14±0.04º corresponding to Si (311) reflections can be identified (Si crystalline structure can be seen on **Fig. 4.3a**). The particular shape of this peak has been reported earlier and ascribed to the presence of non-uniform lattice distortions due to highly tensioned Si QDs inside the PS matrix **[137]**.

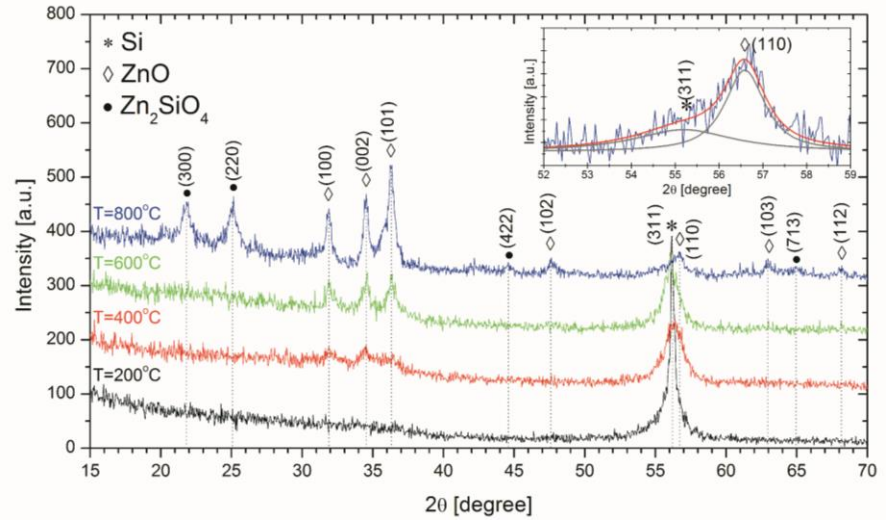

Figure 4.2: Diffraction patterns from PS-ZnO samples annealed between 200 and 800 ºC. The inset shows the deconvolution of the peak centered on 2θ=56º.

ZnO characteristic peaks appear around 2θ=35º when the annealing step is carried out at 400 ºC. These peaks correspond to the (100), (002) and (101) planes from the most common hexagonal wurtzite structure ($P6_3mc$ space group[1], ICDD No. 361451, see **Fig. 4.3b**). In addition, Si (311) peak has been notably reduced as a result of the PS oxidation induced by the annealing step in the presence of oxygen. The sample annealed at 600 ºC shows the same behavior but in this case the ZnO peaks are sharper, suggesting an increased long-range order.

[1] This space group, **$P6_3mc$**, is interpreted as follows:

- **P**: indicates that the Bravais lattice is primitive.
- **6_3**: order 6 sub 3 screw axis oriented in the z direction.
- **m**: there is a reflection plane perpendicular to the x direction.
- **c**: type c glide plane perpendicular to direction [1,-1,0]

At the highest annealing temperature considered (800 ºC) new peaks are observed, which can be attributed to the activation of new Zn silicate phases in the form of α-Zn_2SiO_4 (Willemite, ICDD No. 067235, see **Fig. 4.3c**), as previously reported at similar temperatures (around 900 ºC) **[138]**. Another particular effect of annealing at this temperature is that the (311) Si diffraction peak is hardly distinguishable (inset graph in **Fig. 4.2**) due to the high oxidation of the PS matrix.

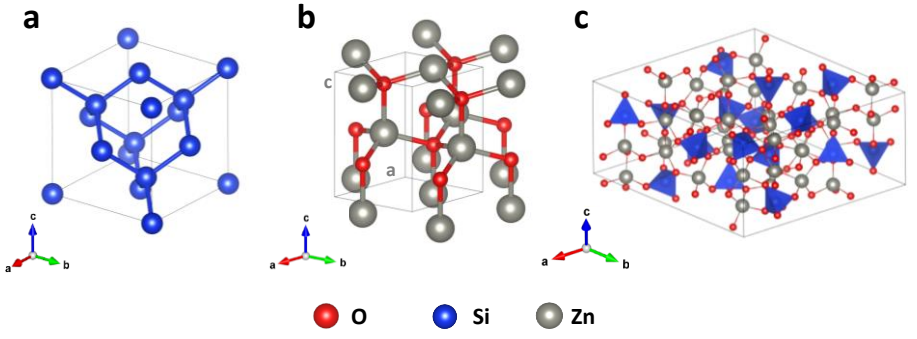

Figure 4.3: Si (**a**), ZnO (**b**) and α-Zn_2SiO_4 (**c**) crystalline structures and their corresponding unit cells (drawn in black lines). Blue tetrahedrons denote silicate units.

Although diffractograms appear noisy, it is possible to calculate the ZnO unit cell dimensions a and c (**Fig. 4.3b**) through the algebraic expression of the interplanar distance for an hexagonal system **[139]**:

$$\frac{1}{d_{hkl}^2} = \frac{4(h^2 + hk + k^2)}{3a^2} + \left(\frac{l}{c}\right)^2 \qquad \textbf{Eq. 4.1}$$

where h, k and l are the Miller indices (hkl); d_{hkl} is the interplanar distance relative to them and *a* and *c* the parameters of the unit cell. Since d_{hkl} is unknown, this parameter can be substituted by using the Bragg's law:

$$n\lambda = 2d_{hkl}\sin\theta \qquad \textbf{Eq. 4.2}$$

where n is the diffraction order ($n=1$ in this case), λ is the X-rays wavelength used (Cu-Kα, $\lambda=1.5405$ Å), and θ the diffraction angle. Thus, by combining **Eq. 4.1** and **Eq. 4.2** the following relationship is obtained:

$$\sin^2\theta = \frac{\lambda^2(h^2+hk+k^2)}{3a^2} + \left(\frac{\lambda l}{2c}\right)^2 \qquad \textbf{Eq. 4.3}$$

Looking closely this equation, a and c appear in different terms. Thus, parameter a can be calculated using diffraction peaks with $l=0$ (peaks (100) and (110) in our data) and, by the same way, parameter c using $h=k=0$ (only the (002) diffraction peak). The following expressions and results are obtained:

$$a = \left[\frac{\lambda^2(h^2+hk+k^2)}{3\sin^2\theta}\right]^{\frac{1}{2}} = 3.2 \pm 0.3 \text{ Å} \qquad \textbf{Eq. 4.4}$$

$$c = \frac{\lambda l}{2\sin\theta} = 5.2 \pm 0.7 \text{ Å} \qquad \textbf{Eq. 4.5}$$

These values show large uncertainties due to an overstimation of the experimental error caused by the noisy diffractogram. However, both values are in agreement with the most common parameters reported for ZnO (calculated *a* and *c* are 3.24 and 5.18 Å respectively). In addition, the relation c/a obtained is 1.602 (1.6±0.2), which is very close to the theoretical value of 1.633 **[74]**.

The evolution of the ZnO crystallization can be studied through the ZnO effective crystallite size (L) calculated by using the Scherrer formula **[121]**:

$$L = \frac{0.9\lambda}{\beta_{2\theta}\cos\theta} \qquad \textbf{Eq. 4.6}$$

where λ is again the X-rays wavelength, $\beta_{2\theta}$ is the full width at half maximum of the diffraction peak and θ the diffraction angle. The constant 0.9 is known as the shape factor, which is related with the crystallite shape (originally $2[\ln(2)/\pi]^{1/2} \approx 0.9$ for spherical particles **[140]**). In this case, the calculated values are 12±8 nm, 16±5 nm and 20±3 nm for the samples annealed at 400, 600 and 800 ºC respectively, revealing the improvement of ZnO crystallinity with higher annealing temperatures. This result is also interesting to predict that at least the ZnO crystallites formed in these composites at 600 ºC and 800 ºC can be understood as bulk material, since quantum confinement is not present in ZnO until reaching a size around ~10 nm due to its high exciton binding energy **[141, 142]**.

4.3 Detailed structural information (TEM, SAED, EDX)

The Si nanostructure has been studied in depth by TEM, revealing that mesoporous silicon is formed by Si QDS embedded in a matrix formed by amorphous Si and silicon oxide (a-Si:O) **[33, 34, 143, 144]**. However, there is a lack of detailed structural information of the PS-ZnO system through this technique in the literature. So far, it has been shown by FESEM that the ZnO permeates the PS columnar structure along the [100], being its size limited by the pore diameter. This is checked again by TEM (**Fig. 4.4a**). Taking a closer look to the PS walls in a sample annealed at 600 ºC (**Fig. 4.4b**), it can be seen that the size of the Si nanocrystals is around ~20 nm. In addition, the hexagonal pattern obtained by selected area electron diffraction (SAED, inset on **Fig. 4.4a**) confirms that the ZnO crystals correspond to a wurtzite structure. Both results are in agreement with the GIXD results previously discussed.

Aiming at applications in optoelectronics, it is useful to determine how Si and ZnO may interact. **Fig. 4.4d** shows an EDX microanalysis from the sample that clearly reveals Si- and Zn-rich regions corresponding to a Si QD and the ZnO nanocrystals respectively. Relevantly, there seems to be (as expected due to the PS oxidation) a region of Si and ZnO lower concentration in the interface, which may indicate the existence of a SiO_2 barrier between them. This situation is repeated all

over the nanocomposite, indicating that Si QDs and ZnO nanocrystals can stablish semiconductor-insulator-semiconductor junctions (Si QDs-silica-ZnO). The silica barrier is expected since PS is exposed to air before the ZnO synthesis and is annealed at high temperatures. Finally, the EDX analysis does not show any additional elements in the composite (apart from C and Cu coming from the grid used for supporting scrapped material).

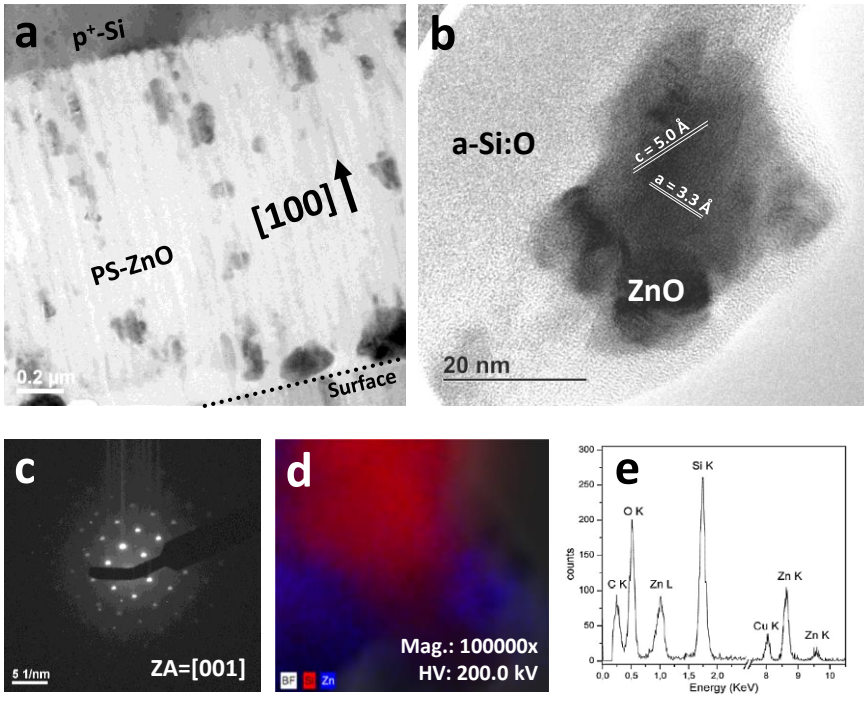

Figure 4.4: (**a**) Low amplification image of the sandwich structure delimited by the dotted line which corresponds to the surface. Darker points correspond to ZnO nanocrystals. (**b**) Detail of a ZnO nanocrystal embedded in the structure. (**c**) SAED image of the ZnO nanocrystal. (**d**) EDX microanalysis performed on the cluster region and (**e**) results from the EDX element detection.

4.4 In-depth composition (EBS analysis)

In order to determine the Zn distribution along the porous network, the possible C traces due to the sol-gel synthesis and the evolution of O with the different annealing processes, an in-depth elemental composition profile was obtained by EBS. While Zn atomic number is large enough to be properly studied

by Rutherford cross sections whitout using resonant energies, both C and O where measured using O-resonant (3.04 MeV) and C-resonant (4.26 MeV) He^+ ions to improve the surface detection of these elements.

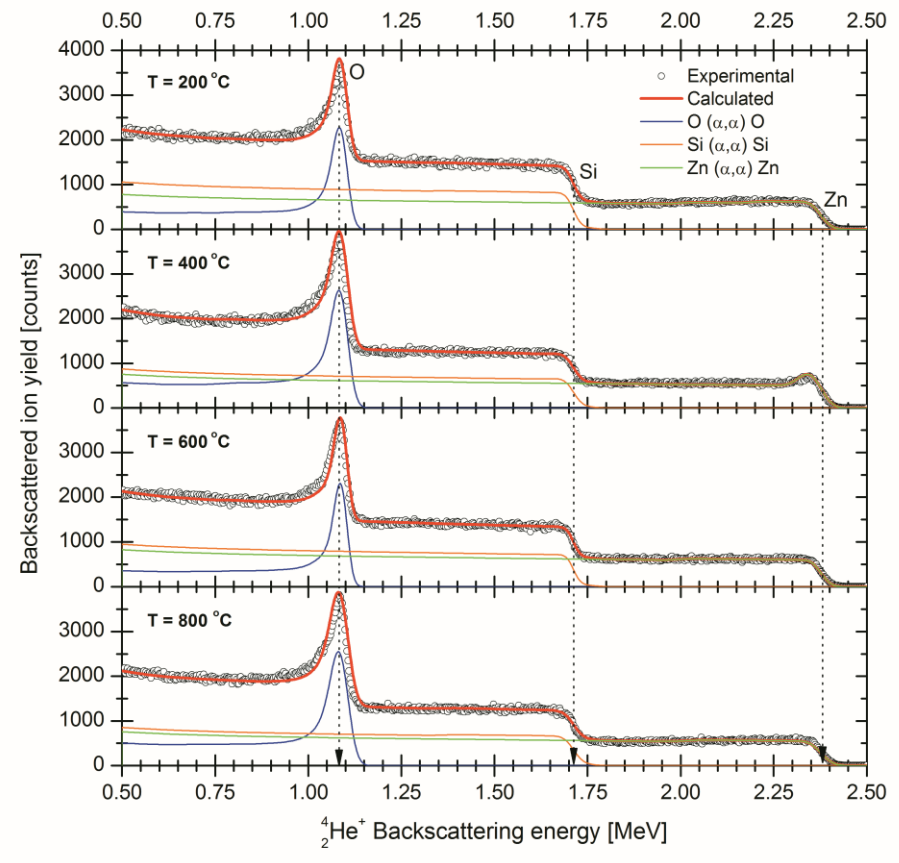

Figure 4.5: EBS results for the samples annealed between 200 and 800 ºC (hollow dots-experimental data, continuous line–fitted spectra) with individual contributions of Zn, O and Si to each fitting. Concentrations are given in at%.

Fig. 4.5 presents the measured spectra and the fittings performed on the PS-ZnO samples annealed at temperatures between 200 ºC and 800 ºC. As discussed in **Chapter 2**, each element appears at an energy determined by **[127]**:

$$E = \frac{M_1^2 E_0}{(M_1 + M_2)^2}\left\{\cos\theta \pm \left[\left(\frac{M_2}{M_1}\right)^2 - \sin^2\theta\right]^{1/2}\right\}^2 \qquad \textbf{Eq. 4.8}$$

where E and E_0, are the backscattered and incindent energies of the ions, θ the scattering angle and M_1 and M_2 the mass of the probing and target atoms, respectively. Thus, the backscattered ion energies were calculated using θ =170.5º, E_0=4.26 MeV, M_1=4.00 uma and M_2=65.38, 28.09, 15.99 and 12.01 uma for the Zn, Si, O and C atomic masses respectively **[9]**.

The signal from Si starts at 1.72 MeV, which corresponds well to surface atoms, demonstrating that no continuous ZnO surface layer has been formed. The signal due to the Zn(α,α)Zn interaction begins at 2.4 MeV (corresponding again to surface atoms) and is present through all the lower energies, confirming the presence of Zn atoms inside the PS pores.

	Surface layer (100 nm)			**Bottom layer (100 nm)**		
Temperature (Δ=±10)	**Zn at% (Δ=±0.5)**	**O at% (Δ=±5)**	**Si at% (Δ=±4)**	**Zn at% (Δ=±0.5)**	**O at% (Δ=±5)**	**Si at% (Δ=±4)**
200 ºC	5.7	56	38	4.0	56	40
400 ºC	6.4	62	32	3.8	59	37
600 ºC	5.6	62	33	2.6	60	37
800 ºC	5.2	65	30	3.5	64	33

Table 4.1: Atomic concentrations obtained from the EBS fittings of the samples annealed between 200 ºC and 800 ºC at the surface (first 100 nm layer) and at the bottom of the pores (last 100 nm layer).

Compositions resulting from the fittings of $26 \cdot 10^4$ atomic monolayers to these spectra are shown in **Table 4.1**, where two atomic concentration values are reported: one evaluated at the first 100 nm surface layer and another evaluated at the last 100 nm layer (i.e. no backscattered He ions were detected from the bulk Si substrate). As seen in this table, the concentration of Si atoms in the sample annealed at 200 ºC is higher due to less PS oxidation (around 38 at%). When the temperature is increased to the range between 400 ºC and 800 ºC, oxygen composition increases up to 62–63%, leading to a [Si]/[O] ratio of 0.5, that is, close to that corresponding to pure silica (SiO_2).

However, the combined Si and Zn concentrations compared to O indicate an excess of non-oxidized Si, which is explained by the presence of the Si QDs observed by GIXD. In the case of the sample annealed at 800 ºC, the trend of the atomic concentrations is in agreement (especially in the surface estimation) with the formation of an a-Zn_2SiO_4 phase, since the stoichiometry becomes closer to that of the ZnO–SiO_2 derived compound. In all cases, the concentration of Zn is higher on the surface than inside the sample, which indicates the presence of an in-depth diffusion gradient.

Temperature (ºC) (Δ=±10)	**Zn at% (Δ=±0.5)**	**O at% (Δ=±5)**	**Si at% (Δ=±4)**	**C at% (Δ=±0.5)**
400	6.7	60	30	3.2
600	5.5	65	25	5.0
800	5.5	70	24	2.0

Table 4.2: Atomic concentrations obtained from the EBS fittings of the samples annealed between 400 ºC and 800 ºC at the surface (approximately first 100 nm).

Fig. 4.5a-c presents the measured spectra and the fittings performed on the PS-ZnO samples annealed at temperatures between 400 ºC and 800 ºC. It can be seen that the signal due to the nuclear Zn(α,α)Zn interaction begins at 3.3 MeV as expected from **Eq. 4.8** (corresponding to surface atoms) and presents an in-depth concentration around 6.0±0.5 at% (**Table 4.2**), which is in accordance with the value obtained by the O-resonant experiments. Again, the Zn concentration is relatively constant along the pores although a slight decrease of its concentration indicatesa Zn concentration gradient. Relevantly, the surface and in-depth Zn concentration values are very similar in every sample and the major differences, are noticed at the bottom of the pores (see concentration profiles on **Fig. 4.5a-c**). Si and O signals are almost the same in the fittings since the concentrations used to fit the O-resonant measurements were initially used to fit the C-resonant ones.

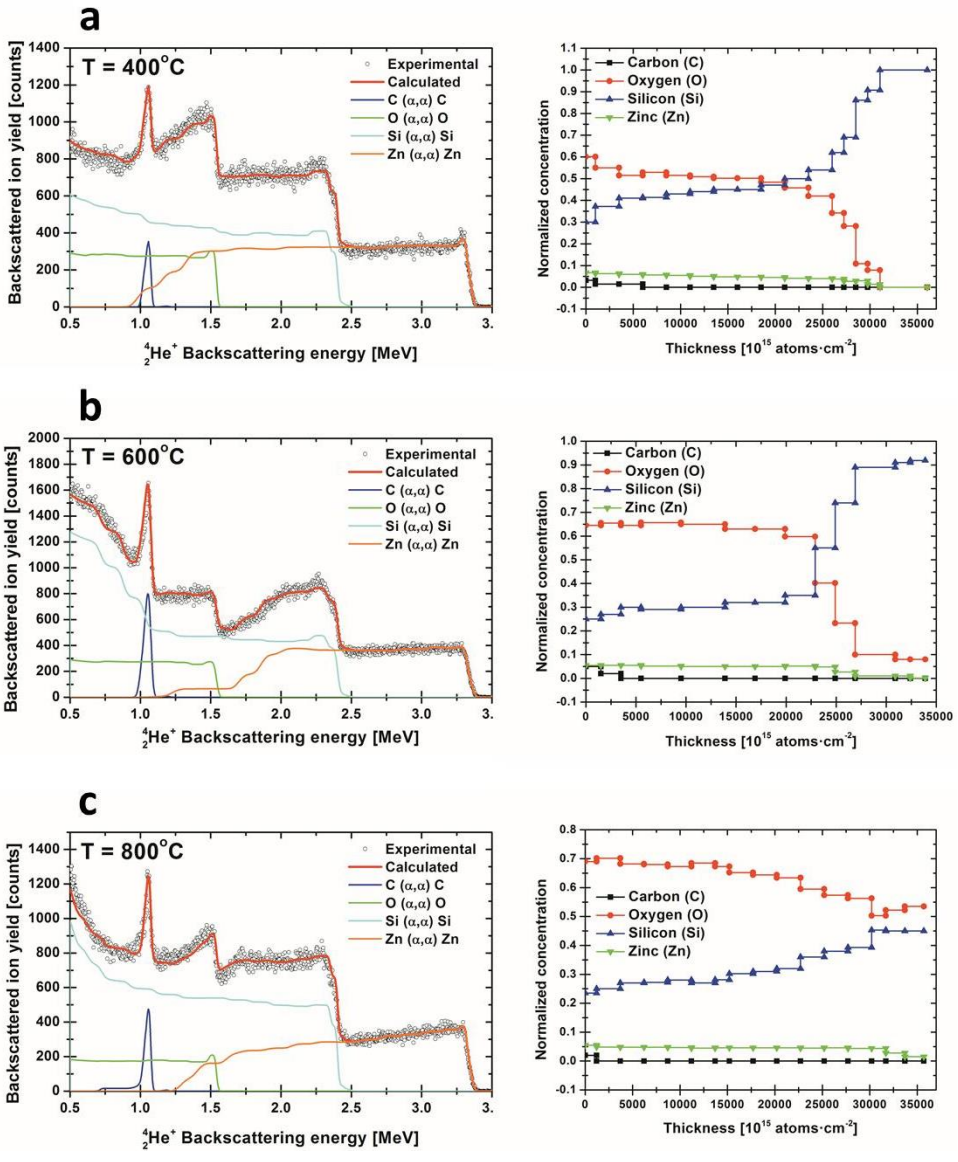

Figure 4.6: EBS results for the samples annealed between 400 and 800 ºC (hollow dots-experimental data, continuous line–fitted spectra) with individual contributions of Zn, O and Si to each fitting. Concentrations are given in at%.

Although C detection with high sensitivity is only effective in the first monolayers (when α particles lose energy the resonant condition is lost), the simulations allow estimating a mean C concentration within the first 100 nm of about 5 at.% for mild temperature annealing (400 and 600 °C). This level is significantly reduced after 800°C annealing to about 2 at %.

4.5 ZnO fine structure (XAS)

As mentioned in **Chapter 2**, XAS spectra can be divided in two (not so well) defined regions. On the one hand, the closest part to the absorption edge is called XANES and carries information about the oxidation state and the local electronic structure of the absorbing atom (Zn in these studies). On the other hand, EXAFS carries information about the local structure, the coordination number and the "disorder". Since each technique discloses different aspects, this discussion is divided in two parts named by the region of interest.

4.5.1 XANES

Spectra of the PS–ZnO nanocomposites annealed at the different temperatures are shown in **Fig. 4.7**. The white line main resonances of the Zn K-edge (labelled A, B and C) are related to electron transitions from occupied Zn-1s to unoccupied Zn-4p states along the main axes of the ZnO unit cell. It is widely accepted that the relative height of the main peaks in the white line spectra can be related to the existence of vacancies, which are evidenced by polarization effects in crystalline structures **[145]**. In this case, ZnO nucleates randomly giving rise to a polycrystalline structure which does not allow obtaining such information. Thus, special attention is paid to the main peak (B), since it is the most sensitive to the local deficiency or excess of O in the absorber vicinity. Additionally, XANES can also account for other properties, like interatomic distances **[124]**.

Remarkable differences can be outlined by contrasting the spectra corresponding to PS–ZnO samples annealed at different temperatures with the ZnO reference. Comparisons are restricted to samples containing crystalline ZnO phases (i.e. annealed from 400 to 800 ºC). Comparing with the absorption edges of ZnO and Zn references on **Fig. 4.7**, the oxidation state for all PS-ZnO samples is clearly the one corresponding to that of the ZnO reference, as derived from the absence of relative shift from the latter. However, the three resonances A, B and C are very different due to the modification of the scattering paths in the Zn atom vicinity. It is noticeable that the intensity of features A and B increase in all samples in contrast to peak C, whose intensity is slightly reduced. The comparison of

experimental and *ab initio* theoretical spectra indicates that these changes of the spectral shape are mainly determined by local structure defects **[146]**. In fact, theoretical studies of nanocrystalline ZnO show that oxygen vacancies (V_O) are the principal candidates to produce these spectral modifications **[147]**. Specifically, the increase in amplitude in resonance A can be attributed to the combined effect of V_O and the relaxation induced displacement of the central atom in the coordination shell. Indeed, V_O in ZnO crystals are thermodynamically favored, even when the annealing is performed in an O-rich atmosphere, for temperatures above 473 K **[148]**. For the sample annealed at 800 ºC, an increase of pre-peak A is noticeable while peaks B and C are considerably reduced. This can be explained by the structural changes in the local coordination caused by the formation of the new phase formed by α-Zn_2SiO_4.

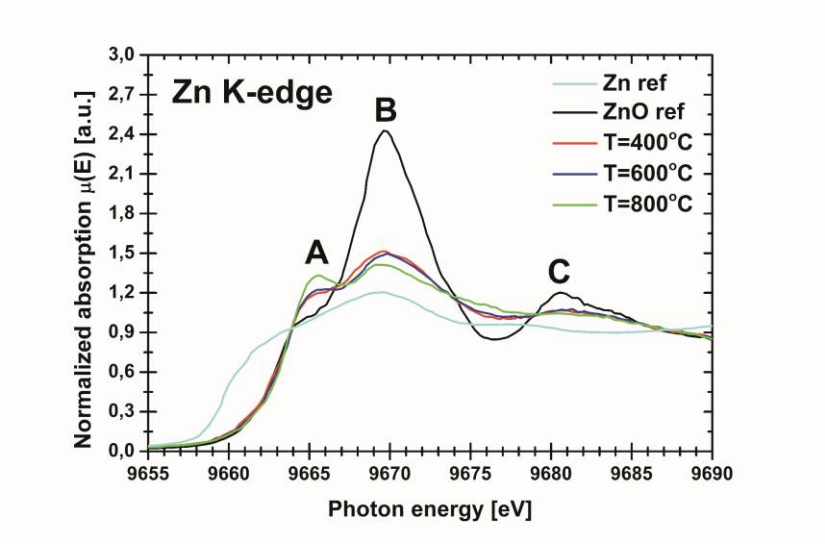

Fig. 4.7: XANES spectra of the PS–ZnO nanocomposites annealed at 400, 600 and 800 ºC, a bulk ZnO reference and a Zn foil reference.

4.5.2 EXAFS

The information obtained from XANES has been complemented with a detailed analysis of the EXAFS signal. **Fig. 4.8a** shows the $\chi(k)$ data obtained from recording the fluorescence signal. A sample of wurtzite ZnO powder was measured

to compare results, showing characteristic peaks denoted by W_1 and W_2. PS–ZnO nanocomposites annealed between 400 and 800 ºC show the same $\chi(k)$ oscillatory behavior as the wurtzite reference, supporting the GIXD results. However, changes in A, B and C features (see labels on graph) indicate particular structural differences, especially for the sample annealed at 800 ºC, where zinc silicates have been previously identified. To study these changes, a FEFF theoretical model was developed starting from a $P6_3mc$ ZnO structure with $a=b=$ 3.2495 Å and c = 5.2069 Å. The scattering path calculations obtained from this structure induce two main contributions to the Fourier transform at 1.5 and 3.5 Å, as identified in **Fig. 4.8b**. The first one is produced by the interaction of the scattering electron with the tetrahedron formed by 3 O atoms at a distance of 2.14 Å and another at 1.79 Å from the Zn absorbing atom. The second one is constituted by Zn atoms, 6 placed at 3.21 Å and 6 at 3.25 Å (both shell structures can be schematically seen in the inset in **Fig. 4.8b**).

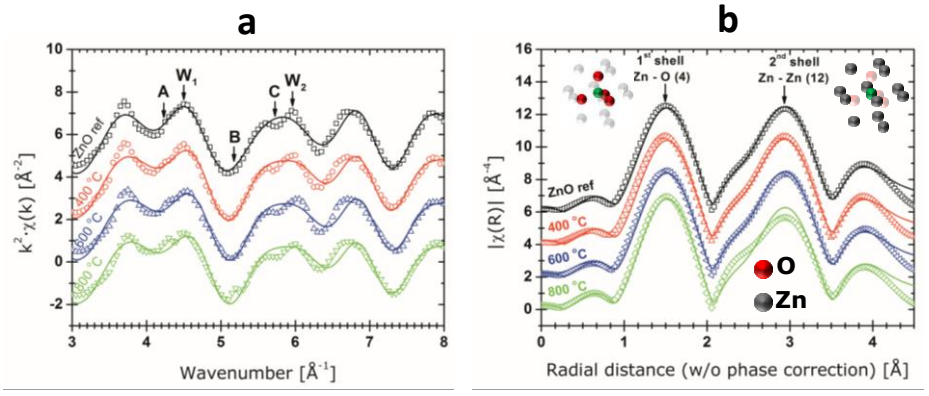

Figure 4.8: $k^2 \cdot \chi(k)$ (**a**) and its Fourier transform (**b**) for the ZnO reference and the samples annealed between 400 and 800 ºC. Experimental data are represented with hollow symbols while the fit to the data is shown with continuous lines. FT is not phase-corrected. An inset to (**b**) shows the atoms in the structure contributing to the shell (green atom represents the absorbing Zn).

Although the spectra in **Fig. 4.8b** are all very similar, the corresponding peak of the second shell of Zn atoms varies in amplitude. This change can be attributed to a change in the degeneracy of the coordination number (N) or to the shell mean-square disorder (σ^2). However, since the nanoparticle size (~nm) and the

coordination shell size (~Å) differ by an order of magnitude, it makes sense to consider that most Zn atoms are fully coordinated and thus, variations due to the presence of point defects or lattice distortions can be derived from the parameter σ^2. This can be seen more clearly by looking at the XAFS equation **[124]**:

$$\chi(k) = \sum_{\forall j} \frac{N_j f_j(k) e^{-2k^2\sigma_j^2}}{kR_j^2} \sin[2kR_j + \delta_j(j)] \qquad \textbf{Eq. 4.8}$$

where subindex j refers to the j'th electron scattering path, $f(k)$ and $\delta(k)$ are theoretical photoelectron scattering properties, R is the distance to the neighboring atom considered and k is the photoelectron wavenumber. As mentioned previously, N and σ^2 are the variables that affect directly the amplitude of the signal (although indirectly it can be also varied by other ways like sample inhomogeneity, detector response…).

Numerical results from the fittings can be found in **Table 4.3**. In the case of the sample annealed at 400 ºC, the first oxygen coordination shell mean-square disorder (σ_O^2) is close to the value obtained for the reference. However, σ_O^2 increases approximately by 40% in the case of the samples annealed at 600 ºC and 800 ºC. It contrasts with the GIXD results that showed an improvement in the long-range order, but can be compatible with a significant presence of non-ordered V_O in this shell. In the case of the second coordination shell formed by Zn atoms, the mean-square disorder σ_{Zn}^2 for the PS–ZnO composites shows variations between 40% and 50%. However, this shell is also affected by Zn–O single-scattering paths beyond the fitting R-range, which affect directly the value of σ_O^2 as well as the presence of V_O and oxygen antisite (O_{Zn}) defects. Green emission from PS–ZnO nanocomposites has been attributed earlier to O_{Zn} **[81]**, especially when the oxygen partial pressure (p_{O_2}) is increased, as seen in the following chemical reaction:

$$\frac{1}{2}O_2(g) + V_{Zn} = O_{Zn} \quad [O_{Zn}] \propto \left(p_{O_2}\right)^{1/2}[V_{Zn}] \qquad \textbf{Eq. 4.9}$$

Thus, this mechanism should not be overlooked. As data are obtained from a Zn K-edge, the nearest O_{Zn} must be at least at the distance of the first Zn neighbor (3.21 Å if it is considered that the O atom stays in the same site as the Zn atom), having a minor contribution to the white line compared to the contribution of the four coordinated oxygen neighbors in the tetrahedron around the absorbing Zn atom (3 at 1.96 Å and 1 at 2.01 Å). Therefore, O_{Zn} must not be discarded when oxygen is present during the annealing process of PS–ZnO nanocomposites. Considering this, feature C (**Fig. 4.8a**) decreases with temperature, probably indicating that the distance between the absorbing Zn atoms and the first oxygen neighbors (d_{Zn-O}) slightly increases. This is in consonance with the increasing uncertainty in the interatomic distance R (**Table 4.3**). If these sites were occupied by oxygen atoms (O_2 with larger ionic radius instead of Zn^{2+} with shorter ionic radius) the distance d_{Zn-O} would tend to decrease by the compression induced by a larger atom replacing the Zn position. Summarizing, the results from XAS measurements suggest that oxygen vacancies are more likely to happen than oxygen antisites, although O_{Zn} can be present in the structure.

	Zn-O (1st shell)		**Zn-Zn (2nd shell)**		
Sample	R **[Å]**	σ_o^2 **(x10^{-4}) [Å^2]**	N	R **[Å]**	σ_{Zn}^2 **(x10^{-4}) [Å^2]**
ZnO	2.01±0.01	25±8	12	3.23±0.02	65±10
400	2.01±0.02	27±10	12	3.23±0.02	87±8
600	2.01±0.03	33±12	12	3.23±0.03	94±10
800	2.01±0.03	35±15	12	3.23±0.03	97±11

Table 4.3: Results from the fittings to the 1st and 2nd shells. PS-ZnO samples are labelled with the temperature used during the annealing process. Errors from the mean square disorder are given with two significant digits intentionally.

4.6 ZnO band gap

The technique UV-Vis was used to determine the ZnO bandgap and its evolution with the annealing temperature. Since PS-ZnO nanocomposites are synthesized on a Si (100) wafer, reflectance spectroscopy with an integrating sphere

was used to obtain data. The best way to determine the bandgaps in amorphous material is using the Tauc plot **[149]**, in which the $(h\nu\alpha)1/n = A(h\nu - Eg)$, where n=1/2 since ZnO is a direct bandgap semiconductor, h is the Planck's constant, ν the photon frequency, A is a constant and E_g the bandgap energy to be determined. The absorption was obtained by the Kubelka-Munk approximation **[150, 151]**.

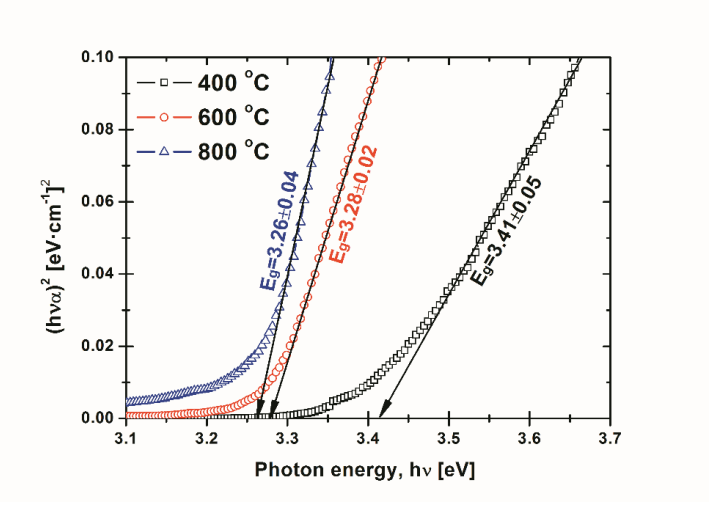

Figure 4.9: Tauc-plots from the samples annealed between 400 and 800 ºC. Absorption was calculated from the reflectance spectra using the Kubelka-Munk transformation.

Results for the samples annealed at 400, 600 and 800 ºC are shown in **Fig. 4.9**. In that figure, it is possible to see how the band gap is closer to the ideal reported value of 3.37 eV **[74]** but looks smaller in the cases of the samples annealed at 600 ºC and 800 ºC which can be explained by the formation of new states in the band gap which, as deduced from the XANES and EXAFS may be due to the formation of V_O and O_{Zn}.

4.7 Photoluminescence

As previously reported, these nanocomposites are able to produce white-light through the combination of red-orange emission from PS and blue-green emission from ZnO **[69-71]**. In order to observe the effects on luminescence of the

processing history of the sample, PL measurements combined with fluorescence microscopy have been used to perform an optical characterization. **Fig. 4.10a-c** shows the PL spectra and non-filtered images of PS-ZnO composites annealed at 400, 600 and 800 ºC respectively. The sample annealed at 400 ºC shows a broad PL peak centered at 618 nm corresponding to PS characteristic orange-red emission **[35]**. As seen on GIXD measurements, ZnO crystals are being formed around that temperature but no significant blue-green emission is observed. This result is supported by its optical fluorescence image. As mentioned before, the PS PL peak can be related to the Si QDs size embedded in the PS matrix **[13]**. Thus, the Si QDs average size has been calculated resulting in 19±2 Å using the suggested model for he exciton quantum confinement in QDs of indirect band-gap materials.

At 600 ºC, in coincidence with the XANES pre-peak increase (feature A in **Fig. 4.6**), luminescence from the sample shows a yellowish color. This result is supported by the coexistence of Si and ZnO nanocrystals in the PS–ZnO composite around that temperature, as demonstrated by GIXD. Furthermore, PL spectra show that this yellowish emission is the combination of three main emission bands centered at 510, 572 and 625 nm. The band centered at 625 nm corresponds to PS but the other bands are directly related to ZnO. Specifically, the broad blue–green (almost yellow) emission can be attributed to O_{Zn} and V_O intrinsic defects respectively **[71, 82]**, which is in agreement with the XANES and EXAFS results. Nevertheless, the emission around 510 nm may be constituted partly by luminescence originating in silica formed in the PS structure, whose presence is more evident at this temperature, as shown by EBS.

Finally, the PL spectra and an optical fluorescence image of the sample annealed at 800 ºC are shown. The emission observed through the fluorescence microscope shows a greenish color attributed to point defects on ZnO nanocrystals and the characteristic luminescence from α-Zn_2SiO_4 **[138]**. The detailed study of the PL spectra show a blue-green band when the samples are irradiated with λ_{exc}>490 nm. This result is remarkable and indicates that a different luminescence mechanism is taking place, merging contributions from silica, ZnO intrinsic defects (at least V_O and O_{Zn}) and α-Zn_2SiO_4.

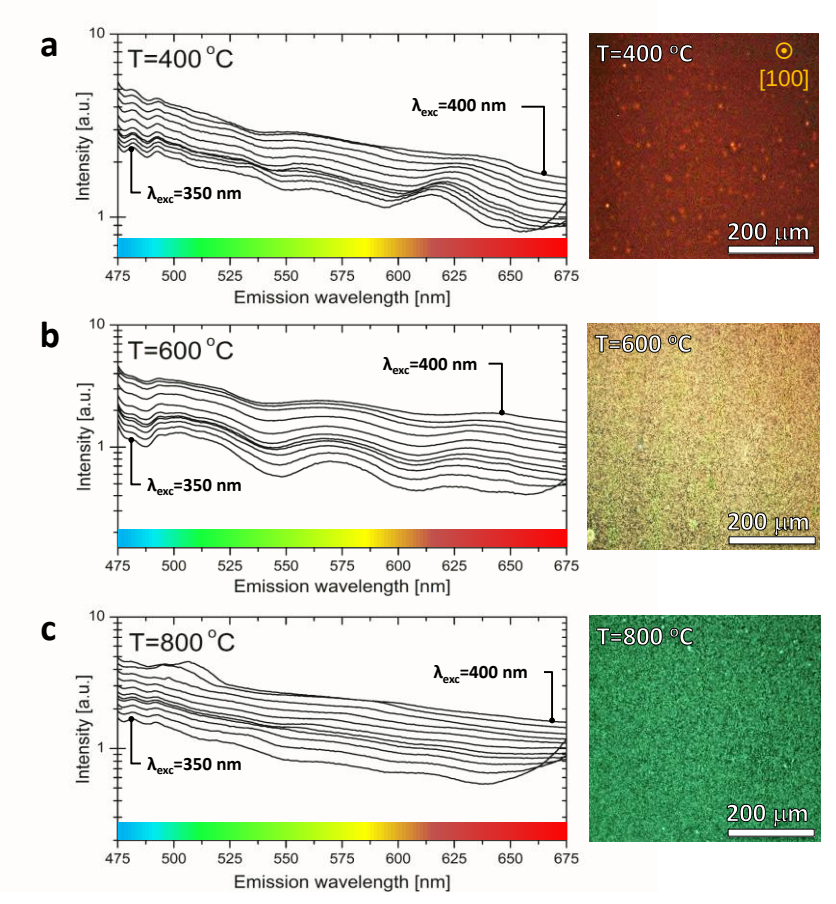

Figure 4.10: PL measurements and fluorescence microscopy images taken from the samples annealed at 400 °C (**a**), 600 °C (**b**) and 800 °C (**c**). Note that the features observed at 481 nm and 492 nm correspond to discrete lamp emission lines.

CHAPTER 5:

PS-ZnO electroluminescent devices

Literature dealing with the fabrication and properties of PS-ZnO nanocomposites agrees with the suitability of this system for light-emitting devices **[62, 69, 73, 77]**. However, electroluminescence (EL) or current-voltage (J-V) measurements are found only in few works using indium-doped zinc oxide (IZO) **[92, 152]** or ZnO as contact, but not as active material **[73]**. Therefore, the objective of this chapter is to study these characteristics in the PS-ZnO nanocomposites studied in **Chapter 4**. The samples were completed with an indium tin oxide (ITO) front side contact resulting in an ITO/PS-ZnO/p^+-Si/Al structure in which ZnO is used as active material in combination with PS (see **Chapter 2** for details about the synthesis). Furthermore, the lack of a model that explains the electrical behavior and the mechanism of white-light emission from these structures moved us to propose one.

5.1 Morphology

Fig. 5.1a shows the surface of a PS-ZnO layer annealed at 600 ºC before growing the top ITO transparent contact. It shows a large amount of uniformly distributed ZnO crystals (mean diameter 75±20 nm) covering 55% of the surface. **Fig. 5.1b** shows a cross-sectional view of the sample once the contact has been grown and annealed (i.e. ITO/PS-ZnO/p^+-Si structure). This last image reveals that PS pores propagate along the [100] direction (see **Chapter 4**). The mean pore diameter is 48±17 nm, in contrast to the exposed pores seen on **Fig. 5.1a**, whose diameter is around 17±6 nm. This observation suggests a gradient of the ZnO concentration, since ZnO nucleated preferentially close to the surface. Nevertheless,

the inset shows a detail of the p^+-Si/PS-ZnO interface in which ZnO can be observed permeating some pores, forming a delocalized interface.

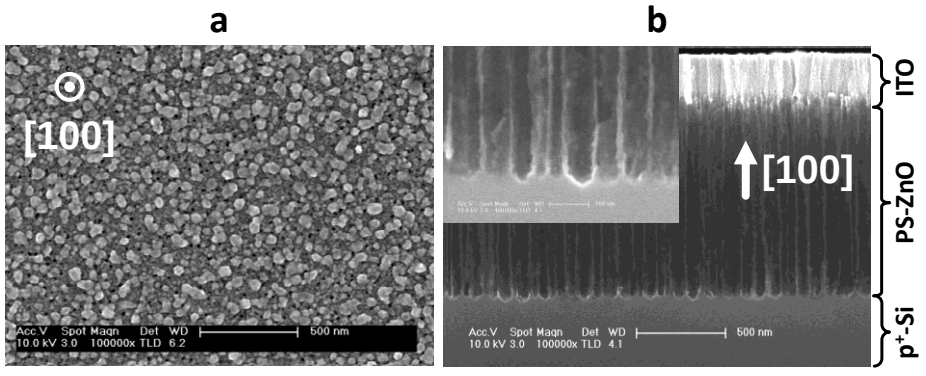

Figure 5.1: Top view of the sample before growing the ITO contact (**a**). Cross-section of the ITO/PS-ZnO/p^+-Si part of the device. The graph inset shows a detail of the pores (**b**).

5.2 Electroluminescence

The experimental setup used to test the device is shown in **Fig. 5.2a**. Note that forward bias voltage (V_{FB}) is applied to the sample when the probe, touching the ITO layer, is set at negative voltages. **Figs. 5.2b-e**, reveal that white EL can be observed when the structure is forward-biased at voltages above V_{FB}>4 V. Taking a closer look, the light is produced on localized spots over the surface, which can be due to the non-conformably covered PS surface with ZnO. This may also indicate that the main contribution from the composite to the total luminescence is produced there. In addition, the right side of the sample appears brighter when the V_{FB} is increased, which can be induced by a voltage gradient as a result of local ITO contact properties.

With the device forward biased at V_{FB}=10 V (i.e. **Fig. 5.2e**), the EL spectrum was measured (**Fig. 5.2f**). This particular bias value corresponds to the highest possible voltage (maximum emission) that the current structure is capable to withstand before resulting permanently damaged. The spectrum can be resolved in three main emission bands labeled as A, B and C (**Fig. 5.2f**).

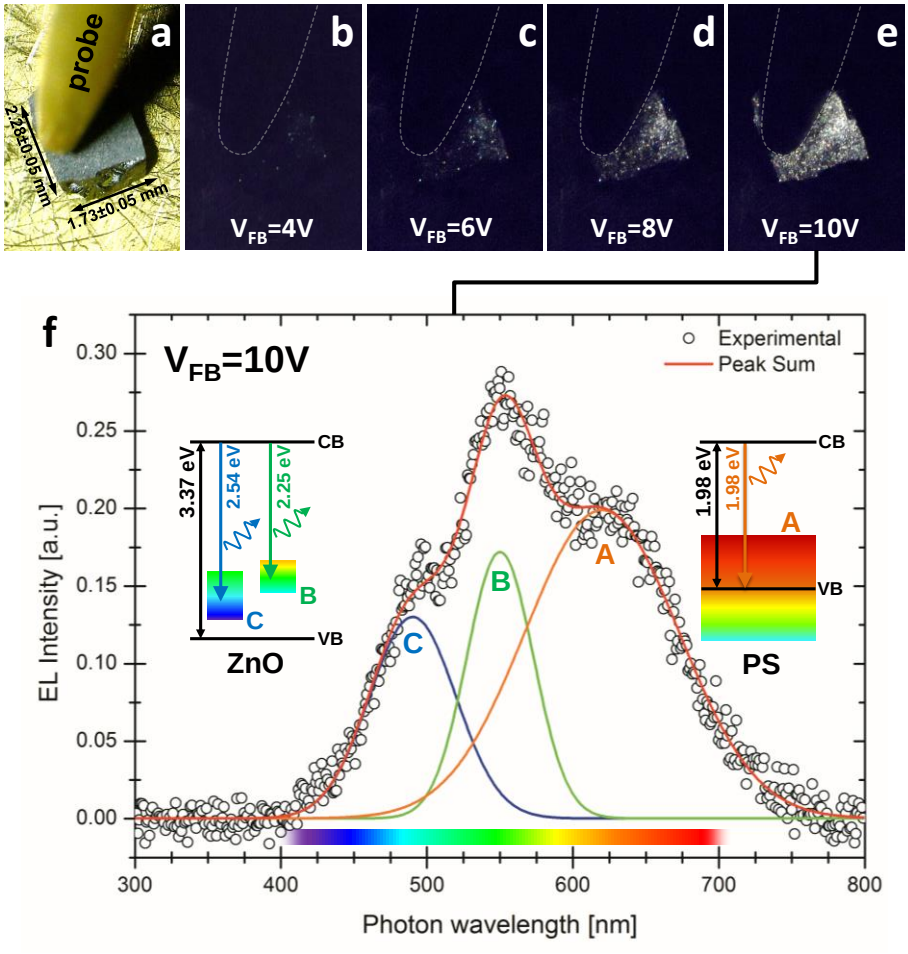

Figure 5.2: Images from the device taken through a lens with a Coolpix L18 camera showing the sample and the probe prepared for the test (**a**), and the sample forward-biased at 4, 6, 8 and 10 V (**b**, **c**, **d** and **e** respectively) in the dark. Graph (**f**) shows the EL spectrum obtained from a forward-biased ITO/PS-ZnO/p^+-Si/Al structure (hollow dots) at V_{FB} = 10 V. Insets show graphically the origin of the emission bands and their broadening.

Band A is centered at 625 nm (1.98 eV), corresponding to a visible orange-red emission produced by quantum confined exciton recombinations in Si QDs embedded in PS **[153]**. The broad band observed is explained by the fact that a size distribution of the Si QDs is produced during the electrochemical anodization **[33]**. Consequently, this size distribution can be related with the PS photoluminescence emission spectrum using theoretical models developed for small semiconductor crystallites **[35]**:

$$E \approx E_{Si} + \frac{\hbar^2 \pi^2}{2R^2}\left(\frac{1}{m_e} + \frac{1}{m_h}\right) - \frac{1.8e^2}{\varepsilon_{Si} R} \qquad \textbf{Eq. 5.1}$$

where E_{Si} is the band gap energy of bulk Si, $\hbar$ the Planck's constant, m_e and m_h the effective mass of the electron (e^-) and hole (h^+) respectively, e the elementary charge, ε_{Si} the dielectric constant of Si and R the radius of a spherical QD. The second term in the equation corresponds to the energy of a pair electron-hole inside a spherically symmetric potential while the third term is the consequence of the Coulomb attraction. From this equation a mean QDs size of 20±3 Å has been calculated by taking E as the energy corresponding to the emission maximum.

Bands B and C are centered at 490 nm (2.54 eV) and 550 nm (2.25 eV), respectively. Both are related to electronic transitions between the ZnO conduction band (CB) and deep level native point defects produced in its crystalline structure. However, silica formed during the PS oxidation may contribute to band C around 510 nm. These bands show a broadening which can be related to the local structure of the intrinsic defect affecting the energy levels in the gap. In fact, we have seen so far by XAFS in **Chapter 4** that the annealing process at this temperature (600 ºC) in the presence of oxygen favors the formation of donor oxygen vacancies (V_O), which contributes to the green-blue luminescence emission as well as the ZnO intrinsic n-type character (see also **[148]**). In addition, blue-green emission from PS-ZnO composites is also attributed to oxygen antisites (O_{Zn}), especially when the oxygen partial pressure increases **[81]**. Nevertheless, the additional energy levels formed in the band gap by this kind of defect are deeper than those formed by V_O **[82]**. Therefore, we have assigned the blue and green bands to V_O and O_{Zn}-silica respectively. The measured EL spectrum and its different band emissions are in good agreement with previous photoluminescence (PL) results from PS-ZnO composites reported by different groups **[70, 71]**.

5.3 J-V characteristics and modelization

For a better understanding of the mechanisms involved in the device operation, the current-voltage (J-V) characteristics at RT have been measured. The first thing noticed is the different rectifying behavior revealing different conduction mechanisms for both forward and reverse operation voltages. Hence, three different cases have been studied in detail: equilibrium (no bias), forward and reverse bias.

5.3.1 Equilibrium

Fig. 5.3 shows the proposed energy band diagram at RT using the electron affinity model. The Fermi level (E_F) remains constant along the device. The ITO transparent front-side contact has a high transparency and conductivity and is considered in this model as a conductor whose work function has been taken from previous bibliography **[154]**. This layer is in contact with ZnO.

Due to the ZnO high exciton binding energy (60 meV), quantum confinement effects are not expected in this case and therefore, the band gap between the valence and conduction bands (VB and CB) can be considered as 3.37 eV while the electron affinity as χ_{ZnO}=4.6 eV **[155]**. However, the value calculated by UV-Vis spectroscopy in the case of the PS-ZnO nanocomposite annealed at 600 ºC indicates that the band gap energy is E_g=3.28±0.02 eV. This energy corresponds to a photon wavelength of 380 nm that is very close to the beginning of the electroluminescence emission (**Fig. 5.2f**) indicating that the observed band gap energy may be due to a large number of defects induced in the ZnO structure. Due to the presence of the resolved blue-green band in the EL spectra, two slightly broad levels (simulating the broadening of the emission bands shown on **Fig. 5.2f**) are proposed in the ZnO band gap at 2.54 and 2.25 eV corresponding to O_{Zn} and V_O respectively. In addition, due to the presence of V_O, there is an excess of positive charges and thus, n-type doping is considered **[74]**.

ZnO is in contact with a silica SiO_x (x≈2) layer, formed on the PS surface during the annealing process. In fact, we already know that the surface of electrochemically etched PS is fully covered by highly reactive Si-H bonds that are

rapidly oxidized in the presence of oxygen forming silica **[28, 30]**. Therefore, the model considers the electron affinity of pure silica χ_{SiO2}=0.9 **[156]**.

Beneath this layer, PS has been modelled according to previously developed models in which the intrinsic Si band gap (1.12 eV) is modified due to quantum confinement **[73, 157]** (see **Eq. 5.1**). In this case, the band gap value is taken as 2 eV, corresponding to the mean value of the PS emission observed in the EL spectra in **Fig. 5.2f**. Its valence band is represented by a broad energy level which tajkes account of the effect of the Si QDs size distribution. PS forms a type I (straddled lineup) junction with p^+-Si that as proposed by some authors **[73, 157]** and adapted to this model. In addition, the electron affinity of PS is assumed as 3.7 eV as experimentally calculated in the bibliography **[73]**.

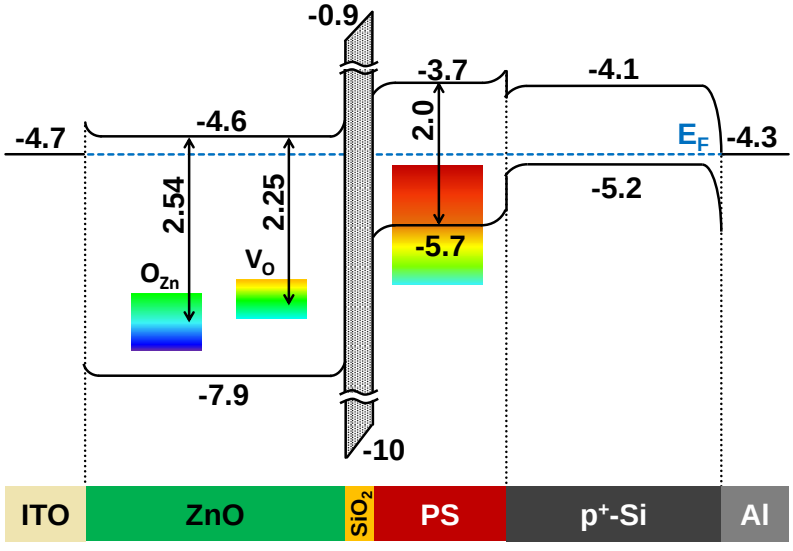

Figure 5.3: Proposed energy band diagram for the ITO/ZnO-PS/p^+-Si/Al structure at 0 V bias. All values are given in eV (zero energy is set at the vacuum level).

The B-doped Si substrate (p^+-Si) has an intrinsic gap of 1.1 eV between its CB and its VB at RT and due to its p^+-type character, the Fermi level is close to the VB. Finally, an ohmic contact is formed between p^+-Si and an Al layer whose work function is assumed as 4.3 eV **[158]**.

5.3.2 Forward Bias

Fig. 5.4a shows the $\log(J) - \log(V)$ plot for forward bias voltages (V_{FB}) revealing three different conduction mechanisms denoted by I, II and III respectively. However, it is the Fowler-Nordheim (FN) plot showed in **Fig. 5.4b** which defines them specifically through the behavior of $\ln(J/V^2)$ vs. $1/V$, where J is the current density and V the applied bias voltage.

At low bias voltages (region I, $0 < V_{FB}(V) < 1 \pm 0.2$), the plot of $\ln(J/V^2)$ against $1/V$ exhibits a logarithmic behavior, indicative of a direct tunneling (DT) in this regime **[159]** given by:

$$\ln\left(\frac{J}{V^2}\right) \propto \ln\left(\frac{1}{V}\right) - \frac{2d}{\hbar}\sqrt{2m_e^*\varphi} \qquad \textbf{Eq. 5.2}$$

Where d is the oxide width, m_e^* the electron effective mass and φ the effective barrier height. **Fig. 5.4c** shows the proposed conduction mechanism. The current is dominated by electrons (e^-) moving along the conduction band from ZnO to PS through the full oxide thickness. In this case, conduction by holes (h^+) is not favorable due to the larger potential energy required to move between the valence bands.

At medium forward bias voltages (region II, $1 \pm 0.2 < V_{FB}(V) < 3.9 \pm 0.2$), the steeper slope in **Fig. 5.4a** indicates an improvement in conduction efficiency. The FN plot indicates that the logarithmic relation between $\ln(J/V^2)$ and $1/V$ corresponds again to a DT conduction mechanism (**Fig. 5.4b)**. The change in the conduction regime occurs for $V_{FB}=1 \pm 0.2$ V (E_F increases 1 eV), which is in agreement with the energy difference between ZnO and PS conduction bands. Above that voltage, e- at the ZnO CB are at higher energy than those in the PS CB, and thus, the tunneling across the oxide is favorable. The PS band starts to bend due to the presence of a stronger electric field.

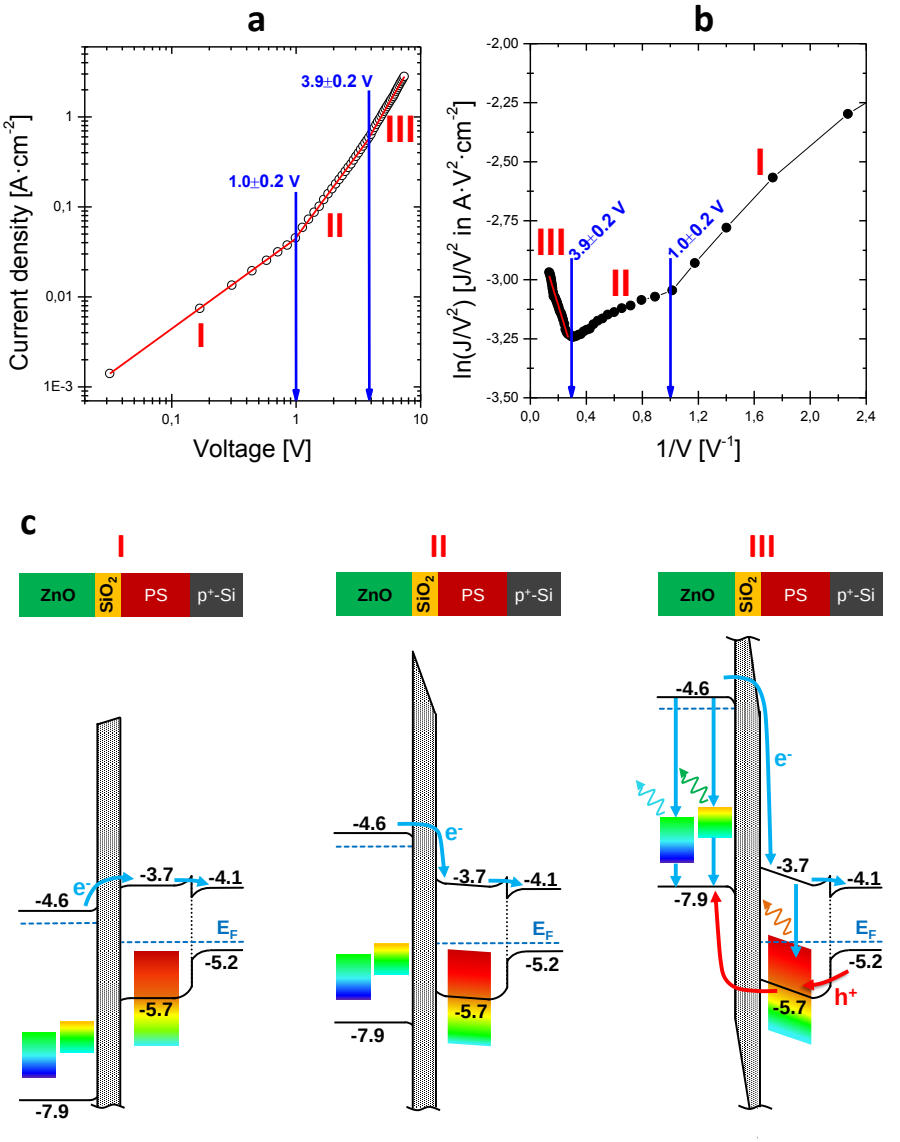

Figure 5.4: $\log(J) - \log(V)$ plot for the forward biased device (**a**), its Fowler-Nordheim plot (**b**) and energy band diagrams showing schematically the three main conduction mechanisms I, II and III (**c**).

At high forward biases (region III, $V_{FB}(V) > 3.9 \pm 0.2$), a new improvement in the conduction is evidenced by the steeper slope (**Fig. 5.4a**). However, the FN plot reveals a completely different behavior. In fact, this lineal behavior indicates that the

main conduction mechanism is FN tunneling (in other words, field emission) **[159]**, described by the relation:

$$\ln\left(\frac{J}{V^2}\right) \propto \left(\frac{-4d\sqrt{2m}}{3q\hbar}\varphi^{3/2}\right)\left(\frac{1}{V}\right) \qquad \textbf{Eq. 5.3}$$

Interestingly, this conduction regime corresponds to the white-light emission from the structure. Actually, the value 3.9±0.2 V obtained from the graphs in which this conduction mechanism begins, agrees with **Fig. 5.2**, where light is observed only for voltages higher than 4 V. Looking at **Fig. 5.4c**, at 3.7 V the ZnO CB reaches the 0.9 eV of the oxide layer and electrons sense the triangular oxide barrier (FN tunneling) and thus, the conduction is improved from ZnO to PS. However, the valence band in this situation has changed noticeably to the point that holes can cross from p^+-Si to PS by tunneling the structure due to a band bending in PS caused by the high electric field. This produces holes in the PS valence band, making possible the radiative recombination and the orange-red emission. Moreover, these holes can tunnel the oxide by DT to the ZnO VB which now is at higher energy, allowing radiative recombinations in ZnO across states in the band gap causing the blue-green band of the EL spectrum (**Fig.5.2f**).

5.3.3 Reverse Bias

Fig. 5.5a shows the $\log(J) - \log(V)$ plot for reverse bias voltages (V_{RB}), revealing again three different conduction regimes denoted in this case by IV, V and VI, respectively. The Fowler-Nordheim (FN) plot showed in **Figure 5.5b** helps determining again the specific conduction mechanisms through the behavior of the plot $\ln(J/V^2)$ vs. $1/V$.

For low reverse bias voltages (region IV, V_{RB}(V) < 2.3±0.2), the FN plot reveals again a logarithmic relationship, indicating that DT is the main conduction mechanism. Taking a closer look at **Figure 5.5c**, the conduction is dominated by holes crossing by DT the oxide barrier, which is energetically favorable. To the

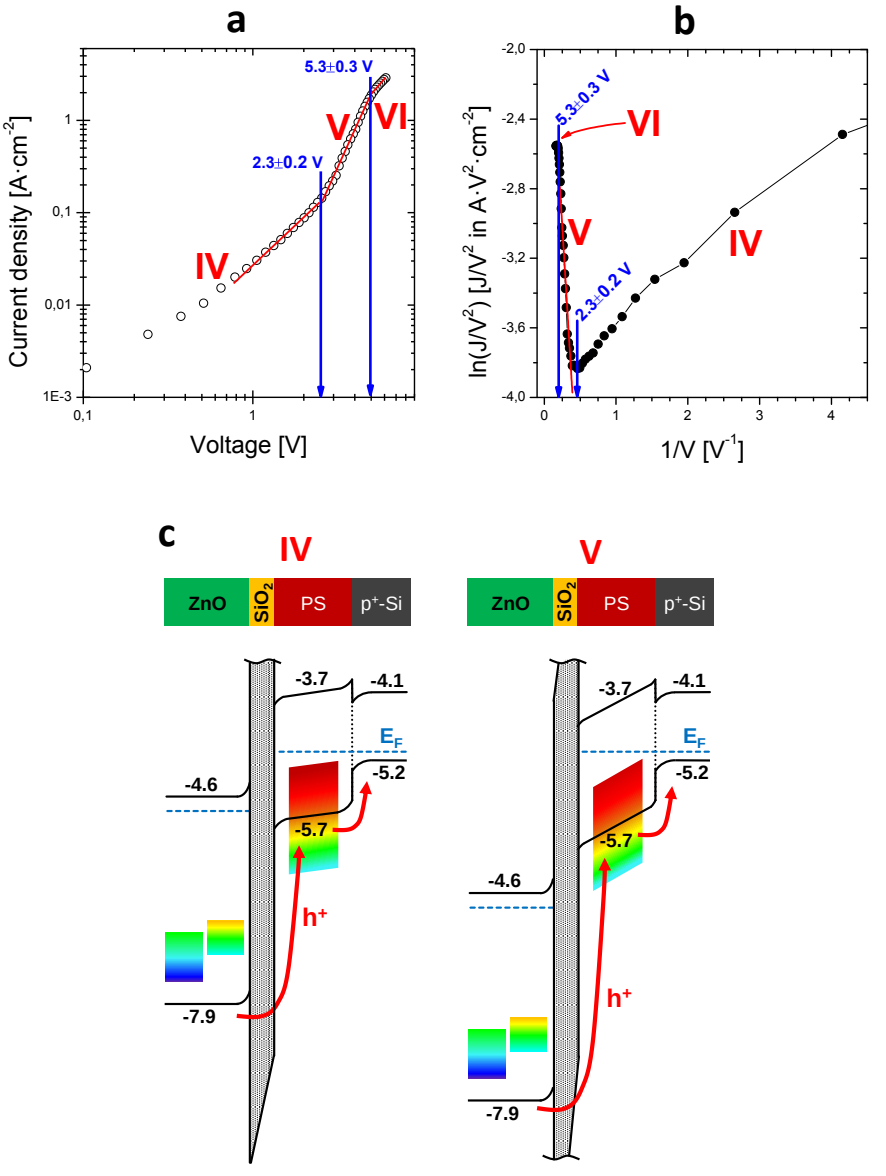

Figure 5.5: $\log(J) - \log(V)$ plot for the reverse biased device (**a**), its Fowler-Nordheim plot (**b**) and energy band diagrams showing schematically the three main conduction mechanisms IV, V and VI (**c**).

contrary, this polarization produces a depletion of electrons in ZnO due to the positive voltage applied to this part of the device and thus, its contribution is not so important. Holes tunneling the oxide barrier see the whole oxide thickness and fall

in the PS valence band energy distribution. This supports the nonlinear behavior of the $\log(J)$-$\log(V)$ plot.

At medium reverse bias voltages (region V, $2.3\pm0.2 < V_{RB}(V) < 5.3\pm0.3$), the FN plot changes to a straight line indicative of field emission, when holes in the ZnO VB see the oxide as a reduced effective barrier, increasing the conductivity. In fact, this corresponds to the energy difference between the ZnO VB and the oxide VB at 10 eV. Under these assumptions, no light can be produced at reverse bias due to the absence of radiative exciton recombinations.

At high bias voltages (region VI, V_{RB} (V) $> 5.3\pm0.3$), the conduction mechanism changes again. This value corresponds to the extreme case in which the band alignment between ZnO CB and PS VB occurs. However, this change may correspond to a damage of the device due to the presence of a high electric field evidenced by the oxide slope in the band energy diagram.

CHAPTER 6

Conclusions and perspectives

This chapter, divided in three parts, contains all conclusions derived from the previous chapters. The first section is about the particular conclusions derived from each system studied. The second section gives a general perspective that tries to answer the question made at the beginning about the suitability of PS for biomedical and optoelectronic applications. The third section discusses the future perspectives based on all previous results.

6.1 Particular conclusions

6.1.1 Functionalized particles

The first study done in this work explored the biomedical applications of PS since this material offers interesting properties such luminescence at room temperature, biocompatibility, biodegradability and a large internal surface. In this particular case, the interest was to deepen in the PS biomedical applications by producing particles that we named PSps. These particles usually lose their luminescence very quickly so that the interest was focused in the functionalization of the Psps passivating their internal structure extending their useful life. The approach to solve this problem was to functionalize the PSps with APTS and PEG.

During the characterization process, SEM images showed that both APTS-PSps and PEG-PSps are dispersed particles with spherical shapes. The mode of both size distributions indicates that most of the particles have sub-micrometric sizes with a mode of ϕ=0.5 μm. However, in the case of APTS-PSps, mean and median values are larger due to the APTS condensation of smaller colloidal particles. In both cases, the size distribution is very similar as well as their cumulative

distribution function (CDF) corresponding to a Rosin-Rammler distribution for medium-sized particles as a result of the PSps formation through a scrapping and milling process and evidencing that those with diameters $0.0<\phi(\mu m)<0.4$ tend to condense in larger ones whose size is close to 0.5 μm.

The surface characterization performed by XPS confirms that freshly–formed PSps exposed to the atmosphere can be modified through self-assembly with PEG and APTS functional molecules. This technique also showed through the O concentrations that a higher oxidation takes place in the case of the PEG-PSps than in the case of APTS-PSps. An explanation to this observation is a protective action due to the APTS condensation described in the morphological aspects.

Interestingly, these modifications with APTS and PEG functional molecules do not alter the PS properties such as its characteristic red-orange luminescence. Furthermore, the experimental results show that APTS and PEG functionalization of PSps results in an improved stability of its luminescence. In particular, APTS-PSps show a remarkable and stable luminesce, with no significant emission quenching or shift for more than 10 days.

However, if the objective of these particles is to be used in biomedical applications, the biocompatibility should be tested. Although not shown in this work, MTT assays carried out with PEG-modified PSps in human mesenchymal stem cells (hMSCs), demonstrated that the particles are not toxic until at least 72 h. Furthermore, its luminescence is still observed through the cellular membrane. This result indicates that this surface modification makes this kind of particle a potential tool for fluorescence tagging applications in biological media (see **[132, 133]**).

6.1.2 PS-ZnO nanocomposites

The second approach to the applications of PS was to optoelectronics. As already mentioned in the text, this material is highly reactive and is not easy to maintain its properties for a long time since it oxidizes and loses its luminescence. Indeed, this is its main drawback. In order to overcome these problems, it has been proposed to fill the PS pores with transparent materials in order to passivate the PS

layer and combine their optoelectronic properties. This aspect was studied along this work focused on the combination of PS with ZnO to produce PS-ZnO nanocomposites that exhibit white luminescence under determined synthesis conditions.

From the results, it is clear that the annealing temperature plays an important role in the physical properties of PS-ZnO nanocomposites, affecting their luminescence, which is determined by a critical balance between Si QDs and defects in ZnO. Crystallinity and the concentration of point defects can be controlled by means of the annealing temperature.

Specifically, electron microscopy shows that the nanocomposites studied are formed by a PS columnar matrix permeated with ZnO nanoparticles at relatively low processing temperatures (200 ºC<T<600 ºC). However, the structure becomes an amorphous SiO_x matrix when the sample is annealed at 800 ºC.

X-ray diffraction showed that the formation of wurtzite ZnO starts at temperatures above 400 ºC, with no relevant diffraction peaks observed at this temperature . Above 200 ºC, crystalline Si and ZnO coexist in the structure. However, this coexistence disappears at 800 ºC, when the formation of a new phase is activated (α-Zn_2SiO_4). At this temperature (800 ºC), the presence of Si QDs has been remarkably reduced. The ZnO structural parameters a and c were 3.2±0.3 Å and 5.2±0.7, resulting in a relation c/a=1.6±0.2, which is close to the ideal ratio of 1.633. In addition, the grain size determines that there is a correlation between the ZnO crystallization and the annealing temperature.

TEM images confirmed the presence of ZnO along the pores. Their crystalline strructure were tested by SAED, which corroborated a wurtzite structure. In addition, EDX performed showed that Si and ZnO crystals are close between them, which is interesting for optoelectronic applications.

EBS results can be divided in two parts: O- and C-resonant experiments. O-resonant experiments indicates that ZnO permeates uniformly the pores stablishing a slight concentration gradient along the pore. Stoichiometry indicates that annealing in presence of oxygen leads to the matrix oxidation in the form of SiO_2. These measurements were completed with C-resonant EBS, that showed small C

concentrations, specially at the surface. In either case, a non-conformably ZnO layer was formed at the surface as suggested by the superficial Si signal.

Changes in the XANES spectra indicate that the most probable point defects found in this structure are oxygen vacancies (V_O) but it does not discard the presence of a much lower concentration of antisite oxygen atoms (O_{Zn}) in the ZnO structure. EXAFS supports this conclusion, showing an increase in the local structural disorder in the first atomic layer that can be attributed to these defects. In addition, both techniques evidence the presence of wurtzite ZnO.

Fluorescence microscopy shows white emission at 600 ºC, when Si QDs red emission coexists with the blue-green emission from oxygen vacancies in ZnO. This technique also shows the dramatic changes induced in the composites annealed at 800 ºC, where no PS induced emission is observed although a strong green luminescence from zinc silicates remains as the main emitting source.

In addition, the ZnO band gap calculated by UV-Vis spectroscopy is closer to its intrinsic value of 3.37 eV but looks smaller in the cases of the samples annealed at 600 ºC and 800 ºC which can be explained by the formation of new states in the band gap which, as deduced from the XANES and EXAFS may be due to the formation of V_O and O_{Zn}.

6.1.3 PS-ZnO electroluminescent devices

So far the EL from a solid-state white-light source (SSWLS) based only on PS and ZnO formed by the sol-gel technique has been shown. Its broadband emission can be resolved into three main bands in the visible range centered at ~490 (light blue), ~550 (green) and ~620 nm (red-orange) that we associate to O_{Zn}-silica, V_O and quantum confinement in Si QDs within PS, respectively. Current-voltage (J-V) characteristics have been studied at RT, showing that the silicon oxide layer grown between ZnO and PS controls the conduction of the device, being direct tunneling (DT) at low bias voltages and Fowler-Nordheim (FN) tunneling at high polarization voltages, for both forward and reverse bias conditions. Visible EL is only achieved at forward bias voltages from the threshold determined by the change of conduction from DT to FN, at $V_{FB}>3.9\pm0.2$ V. An energy band diagram has been proposed to

explain the different conduction mechanisms, suggesting that forward and reverse bias operations are dominated by electrons and holes respectively.

6.2 General conclusions

So far two systems have been studied in order to explore the possible biomedical and optoelectronic applications of PS, answering the question asked at the beginning of the thesis. In contrast to bulk Si, PS has demonstrated to be useful to the production of functionalized PSps and electroluminescent devices.

In the case of PSps, the different surface functionalizations used (PEG and APTS) passivate the surface protecting PS, increasing the luminescence life-time during days, opening the possibility of using this material as a biological marker. In addition, the different functionalization routes used confer these particles special properties depending on the functional group used.

In the case of PS-ZnO, this work has deepened in the study of PS-ZnO nanocomposites using advanced characterization techniques such XAS and EBS. All the work was focused on the analysis of PS-ZnO systems formed at annealing temperatures between 200 ºC and 800 ºC observing changes in the PL that are key to the development of electroluminescent devices. In addition, this part of the work gave new information about the origin of the ZnO blue-green band related with intrinsic point defects, that we related with V_O and O_{Zn}.

These structures were tested by placing a transparent front-side contact in order to inject current in the device. Three bands in the EL were successfully observed as a combination of the recombination in the intrinsic point defects (blue-green), silica and quantum confinement in Si QDs (orange-red emission). The J-V characteristics revealed the different mechanisms of operation being direct tunneling and Fowler-Norheim in both direct and reverse bias voltages. Light is only visible at direct bias (above 4 V), where the recombination of electrons and holes is possible.

In summary, PS is an interesting material for both biomedical and optoelectronic applications. Looking at the big picture of all the work, the biomedical applications are more interesting than the biological applications since

PS has more attractive qualities (luminescence at RT, biocompatibility, biodegradability and large surface to volume ratio) than those that are interesting for optoelectronic applications (Si-based luminescent devices at RT and large surface to volume ratio).

6.3 Future perspectives

In the case of the PSps, different applications can be envisaged by combining the APTS-PSps and PEG-PSps with magnetic nanoparticles such their use for biomedical tracking **[132]**, hyperthermia, or drug delivery taking advantage of the PS large surface to volume ratio. This work is being done nowadays in the group in which this thesis was done.

Despite their low performance, the perspective of the PS-ZnO electroluminescent devices is encouraging since there are many different ways to improve the device. Based on EL results, a good starting point would be to obtain a conformal ZnO capping on the surface and inside the pores, protecting totally the PS layer and taking advantage of the large internal surface area. The best way to achieve this is by infiltrating the pores by electrochemical deposition that allows a precise growth control in contrary to PVD techniques and avoids the presence of organic compounds. In addition, further characterization about ZnO must be made in order to study its electrical properties such the amount of oxygen vacancies contributing to its n-type character.

In addition, an interesting application can result from the combination of both studies using PSps infiltrated with ZnO as three-band emission nanoparticles. This emission may vary with the temperature of the system depending on the band gap behaviour, obtaining temperature-dependent biological markers. However, although biocompatibility tests for nanowires are promising **[160]**, the nanotoxicity of ZnO nanoparticles in this context must be studied in detail.

CHAPTER 7

Conclusiones y perspectivas

Este capítulo, dividido en tres partes, contiene todas las conclusiones derivadas de los capítulos previos. La primera parte se centra en aquellas que son específicas de cada sistema estudiado. Una segunda sección da una perspectiva general que trata de responder a la cuestión que nos hicimos al comienzo del estudio sobre la viabilidad del PS en aplicaciones biomédicas y optoelectrónicas. La tercera y última sección discute las perspectivas futuras basadas en todos los resultados previos.

7.1 Conclusiones particulares

7.1.1 Partículas funcionalizadas

Esta parte del estudio estaba dedicada a las aplicaciones biomédicas del PS, ya que este material ofrece propiedades interesantes tales como luminiscencia a temperatura ambiente, biocompatibilidad, biodegradabilidad y una alta relación superficie-volumen. En este caso, el estudio se centró en profundizar en estas cuestiones produciendo partículas a las que llamamos PSps. Estas partículas, en contacto con un medio oxidante, suelen perder su luminiscencia rápidamente, de modo que la pasivación de la estructura de PS mediante funcionalización aumenta su vida útil. Con tal fin, se emplearon moléculas de APTS y PEG.

Durante el proceso de caracterización, las imágenes de SEM mostraron que, tras ambas funcionalizaciones (APTS-PSps y PEG-PSps), el resultado es el de partículas esféricas dispersas. La moda de la distribución de tamaños indica que la mayor parte de ellas, en ambos casos, tienen tamaños submicrométricos de ϕ=0.5 μm de diámetro. Sin embargo, en el caso de las APTS-PSps, la media y la mediana son mayores debido a la condensación de partículas de PS de menor tamaño. En

ambos casos, la distribución de tamaños y la distribución cumulativa de tamaños (CDF) son muy similares, correspondiendo a una distribución de Rosin-Rammler, como resultado de un proceso de raspado y molienda. Esta distribución evidencia también que las partículas de tamaños $0.0<\phi(\mu m)<0.4$ tienden a condensar en partículas de 0.5 μm.

La caracterización superficial realizada mediante XPS confirmó que las PSps expuestas a la atmósfera pueden ser modificadas mediante autoensamblado con partículas funcionales de PEG y APTS. Esta técnica también mostró, a través de la concentración de O, que existe una mayor oxidación en el caso de las PEG-PSps. Una posibilidad para explicar este resultado puede ser debida a la acción protectora de la condensación de partículas funcionalizadas de APTS frente a las de PEG.

Ninguna de las dos funcionalizaciones altera las propiedades ópticas intrínsecas del PS. De hecho, los resultados experimentales muestras que la funcionalización mediante APTS y PEG resulta en una estabilización de la luminiscencia. En particular, las APTS-PSps, más protegidas frente a la oxidación, muestran una luminiscencia muy estable durante más de 10 días.

Sin embargo, la biocompatibilidad de estas partículas debe ser estudiada si el objetivo es el de aplicarlas en biomedicina. Aunque no se muestra en este trabajo, se han realizado ensayos MTT con las partículas PEG-PSps en células mesenquimales humanas (hMSCs), demostrando que las partículas no eran tóxicas al menos durante las72 h que duró el experimento. De hecho, su luminiscencia aún es observable a través de la membrana celular, indicando que las PSps funcionalizadas tienen potencial como marcador biológico fluorescence **[132, 133]**.

7.1.2 Nanocompositos PS-ZnO

La segunda aplicación del PS está dirigida a la optoelectrónica. Como ya se mencionó anteriormente en el texto, este material es muy reactivo y se oxida muy fácilmente en contacto con una atmósfera oxidante, perdiendo sus propiedades (entre ellas su luminiscencia). Como alternativa para resolver este problema, se ha seguido la tendencia de rellenar los poros del PS con materiales transparentes de modo que se protege su estructura de la oxidación y se pueden combinar las

propiedades optoelectrónicas de ambos materiales. En nuestro caso empleamos ZnO para producir nanocompositos fotoluminiscentes de PS-ZnO bajo determinadas condiciones de síntesis.

A partir de los resultados, se observa que la temperatura a la que se lleva a cabo la cristalización del ZnO juega un papel clave en las propiedades luminiscentes del PS-ZnO, afectando al balance entre los puntos cuánticos de Si formados durante la síntesis electroquímica como a la producción de defectos que afectan a la luminiscencia del dispositivo.

De manera más específica, los resultados de microscopía electrónica muestran nanocompositos formados por PS columnar permeabilizado con nanopartículas de ZnO a temperaturas de 200 ºC<T<600 ºC. Sin embargo, la estructura del PS-ZnO se convierte en una matriz de SiO_x porosa cuando la muestra se trata a 800 ºC.

La difracción de rayos X muestra que la formación de ZnO tipo wurtzita comienza a temperaturas por encima de 400 ºC. Por encima de 200 ºC, los puntos cuánticos de Si y ZnO coexisten en la estructura. Sin embargo, esta coexistencia desaparece a 800 ºC, coincidiendo con la formación de una nueva fase de willemita(α-Zn_2SiO_4). A esta misma temperatura la presencia de puntos cuánticos de Si es muy reducida, no observándose apenas reflexiones por parte de sus planos crustalinos. Los parámetros estructurales a y c calculados a través de la difracción de rayos X son 3.2±0.3 Å y 5.2±0.7 respectivamente (c/a=1.6±0.2). Además, el tamaño de cristalito determina que hay una correlación entre la cristalización de ZnO y la temperatura a la que se lleva a cabo el tratamiento térmico.

La microscopía electrónica TEM confirma también la presencia de ZnO a lo largo de los poros. Su estructura cristalina volvió a ser determinada mediante SAED, que corroboró una estructura de wurtzita. El EDX complado al TEM permitió observar la coexistencia de cristales de Si y ZnO próximos entre sí.

Los resultados de EBS pueden dividirse en resonancia de O y C. Los experimentos de resonancia de O indican que el ZnO permeabiliza uniformemente los poros con un ligero gradiente de cocentración en profundidad. La estequiometría indica que los tratamientos térmicos en presencia de oxígeno produce una oxidación de la matriz de PS en forma de sílice. Estas medidas fueron complementadas con las

de resonancia del C que mostraron pequeñas concentraciones superficiales de C. En ambos casos, se muestran átomos de silicio en superficie indicando capas no uniformes de ZnO en superficie.

Los cambios observados en el espectro de XANES indican que los defectos puntuales más probables son vacantes de ocígeno (V_O) pero no es posible descartar la presencia de antisitios de O (O_{Zn}), cuya formación es favorable bajo las condiciones del tratamiento térmico. EXAFS apoya esta conclusión, mostrando un aumento en el desorden local de la estructura cristalina que puede ser atribuído a la presencia de dichos defectos.

La espectroscopía de fluorescencia muestra una emisión de luz blanca en las muestras cristalizadas a 600 ºC al sumarse las emisiones de los puntos cuánticos de Si y los defectos intrínsecos del ZnO. Esta técnica muestra, además, un cambio importante en la luminiscencia de las muestras tratadas a 800 ºC que pasa a ser verde como resultado de la desaparición de la contribución del PS y la formación de silicatos luminiscentes de zinc.

Además, la banda prohibida del ZnO se ha calculado mediante espectroscopía ultravioleta-visible (UV-Vis), encontrando que se encuentra próximo a los 3.37 eV pero resulta de menor energía para las muestras tratadas a 600 y 800 ºC, lo cual puede explicarse con la formación de nuevos estados en la banda prohibida debidos a las vacantes y los antisitios de O.

7.1.3 Dispositivos electroluminiscentes de PS-ZnO

En este estudio se ha observado la EL blanca del dispositivo de PS-ZnO formado mediante la técnica de sol-gel. La emisión se puede resolver en tres bandas principales en el rango visible centradas a ~490 (azul claro), ~550 (verde) y ~620 nm (red-orange) que asociamos a los O_{Zn}-sílice, V_O y al confinamiento cuántico respectivamente. Las medidas de corriente-voltaje (J-V) se han estudiado a RT, mostrando que la intercara de SiO formada entre el PS y el ZnO controla la conducción del dispositivo, siendo túnel directo (DT) y Fowler-Nordheim (FN) a voltajes de polarización bajos y altos respectivamente. La electroluminiscencia se obtiene únicamente en polarización directa para voltajes a partir de $V_{FB}>3.9\pm0.2$ V,

momento en el cual el mecanismo de conducción pasa de DT a FN. Se ha propuesto un diagrama de bandas para explicar los mecanismos de conducción.

7.2 Conclusiones generales

Se han estudiado dos sistemas diferentes basados en PS para explorar la aplicación de este material en biomedicina y optoelectrónica, tratando de responder a la pregunta formulada al principio de este trabajo. A diferencia del Si cristalino macroscópico, el PS ha demostrado ser un material adecuado para la producción de partículas funcionalizadas (PSps) y dispositivos optoelectrónicos.

En el caso de las PSps, las diferentes moléculas empleadas en la funcionalización (PEG y APTS) tienen un efecto protector de la matriz de PS, preservando la luminiscencia y aumentando así el tiempo útil de las partículas. Esto abra la posibilidad de emplear dichas partículas como marcadores biológicos. Además, las dos rutas seguidas para la funcionalización confieren a estas partículas propiedades especiales dependiendo del grupo funcional empleado.

Por otro lado, en el caso de los nanocompositos de PS-ZnO, este estudio ha profundizado en su caracterización, mediante técnicas avanzadas de análisis como XAS y EBS. Todo el trabajo se ha centrado en el análisis de los sistemas PS-ZnO sintetizados a temperaturas entre 200 y 800 ºC, observando cambios en la fotoluminiscencia que son claves para el desarrollo de dispositivos electroluminiscentes. Además, esta parte del trabajo proporcionó nueva información sobre el origen de la luminiscencia azul-verde del ZnO que está relacionada con la formación de defectos puntuales.

Las estructuras fueron estudiadas tras crecer un contacto eléctrico transparente para inyectar corriente en el dispositivo. El espectro de EL mostró tres bandas relacionadas con el confinamiento cuántico en el PS (rojo-anaranjado) y la emisión por recombinación en los estados de las defectos puntuales en el ZnO (azul-verde). La medida de EL incluye la caracterización de corriente voltaje (J-V), delatando diferentes mecanismos de conducción, siendo túnel directo (DT) y emisión de campo (Fowler-Norheim, FN) tanto en polarización directa como indirecta. La emisión de luz sólo se observa en polarización directa (>4V), momento en el cual se pasa de conducción por efecto túnel a conducción por efecto campo.

Como conclusión, el PS es un material con interesantes aplicaciones en el terreno del a biomedicina y la optoelectrónica. Sin embargo, sus características hacen que las aplicaciones en el primer campo sean más atractivas (luminiscencia, biocompatibilidad, biodegradabilidad y alta relación superficie-volumen) que en el caso de las aplicaciones en optoelectrónica (luminiscencia, dispositivos basados en Si y alta relación superficie-volumen).

7.3 Perspectivas futuras

En el caso de las PSps, se pueden prever diferentes aplicaciones combinando las partículas modificadas con APTS y PEG con nanopartículas magnéticas para ser utilizadas como marcador biológico **[132]**, hipertermia o liberación controlada de fármacos empleando su relación superficie-volumen. Estos trabajos están siendo realizados en el grupo en el que se ha llevado a cabo esta tesis.

A pesar de su baja eficiencia, la perspectiva de los dispositivos electroluminiscentes de PS-ZnO es alentadora, dado que hay diferentes maneras de mejorar el dispositivo. A partir de los resultados de EL, un buen punto de partida puede ser el obtener una capa continua de ZnO en la superficie del PS y dentro de la matriz de PS, aprovechando toda su área interna. La mejor manera de conseguir esto es infiltrando los poros mediante electrodeposición, que permite un control preciso de crecimiento a diferencia de las técnicas físicas (PVD). Además se debe llevar a cabo una caracterización más en profundidad del ZnO para comprender mejor sus propiedades eléctricas como la cantidad de vacantes de O que contribuyen a su carácter tipo n.

Además, la combinación de ambos estudios puede dar lugar a una interesante aplicación en el campo de la biología. Combinando la fluorescencia de las partículas con las del ZnO pueden conseguirse partículas con 3 bandas de emisión. La temperatura puede jugar un papel importante dependiendo de cómo afecte a las propiedades optoelectrónicas del PS-ZnO. En este caso, aunque la biocompatibilidad para nanohilos de ZnO ha sido probada **[160]**,hace falta conocer más en detalle lo que sucedería con el ZnO en este contexto.

Appendix I

EXAFS model

In this section, the model used for EXAFS analysis is explained. The number of guessing variables (N) available for fitting is given by the Nyquist criterion ($N = 2\Delta k \Delta R/\pi$). Assuming that EXAFS is ideally packed with information, our data allows the use of $N = 11$ variables. However, the number of variables was kept below this value for a more consistent model. In order to keep it as low as possible, a first shell was modelled as 4 atoms placed at 2.01 Å and a second shell as 12 Zn atoms at 3.23 Å (See **Fig. A.1**). This approximation is valid since the bond distance resolution ($r = \pi/2\Delta k$) for this data set is 0.3 Å, which is higher than the resolution of the theoretical model. Fittings of these functions were made between 1 and 3.5 Å in the real space using single scattering paths.

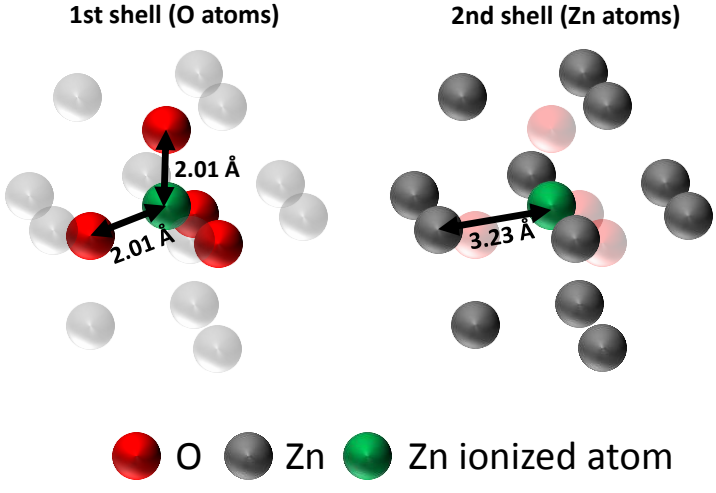

Fig. A.1: Schematic picture of the model used for the EXAFS analysis. Atoms further than the 2nd shell are not shown for simplicity.

To improve the reliability of the results, paths larger than the fitting window have been included (up to 5 Å). **Fig. 4.7b** shows how these paths tend to adjust the experimental data between 3.5 and 4 Å showing consistency for this model. Multiple scattering paths would require different mean-square disorders to take into account the different lengths and number of O and Zn atoms involved. However, there is no information available in the data to resolve such an amount of variables, and combining them in a global scattering variable produces distorted models. For this reason, they were not taken into account as there is no statistical improvement.

REFERENCES

[1] P. Xiaodong. Doping Silicon Nanocrystals with Boron and Phosphorus, Journal of Nanomaterials (2012) 912903 (912909 pp.)-912903 (912909 pp.).

[2] R. Hull. Properties of crystalline silicon. INSPEC, 1999.

[3] C.J. Allegre, J.P. Poirier, E. Humler, A.W. Hofmann. The chemical composition of the Earth, Earth and Planetary Science Letters 134 (1995) 515-526.

[4] L.T. Canham. Nanoscale semiconducting silicon as a nutritional food additive, Nanotechnology 18 (2007).

[5] G. Voskerician, M.S. Shive, R.S. Shawgo, H. von Recum, J.M. Anderson, M.J. Cima, R. Langer. Biocompatibility and biofouling of MEMS drug delivery devices, Biomaterials 24 (2003) 1959-1967.

[6] B.L. O'Dell. Handbook of Nutritionally Essential Mineral Elements, CRC Press, 1997.

[7] F.H. Li, M.K. Balazs, S. Anderson. Effects of ambient and dissolved oxygen concentration in ultrapure water on initial growth of native oxide on a silicon (100) surface, Journal of the Electrochemical Society 152 (2005) G669-G673.

[8] L.L. Hench, J. Wilson. Biocompatibility of Silicates for Medical Use, Ciba Foundation Symposia 121 (1986) 231-246.

[9] C. Kittel. Introduction to Solid State Physics, John Wiley & Sons, 2004.

[10] S.S. Iyer. Light emission from silicon. In: Xie YH, (Ed.), vol. 260: Science, 1993 p.40-46.

[11] E. Roduner. Size matters: why nanomaterials are different, Chemical Society Reviews 35 (2006) 583-592.

[12] A. Uhlir. Electrolytic shaping of germanium and silicon. vol. 35: Bell Syst. Tech. J., 1956. p.333-347.

[13] L.T. Canham. Silicon quantum wire array fabrication by electrochemical and chemical dissolution of wafers, Applied Physics Letters 57 (1990) 1046-1048.

[14] A.G. Cullis, L.T. Canham. Visible-Light Emission due to Quantum Size Effects in highly Porous Crystalline Silicon, Nature 353 (1991) 335-338.

[15] A. Richter, P. Steiner, F. Kozlowski, W. Lang. Current-Induced Light-Emission from a Porous Silicon Device, Ieee Electron Device Letters 12 (1991) 691-692.

[16] K.D. Hirschman, L. Tsybeskov, S.P. Duttagupta, P.M. Fauchet. Silicon-based visible light-emitting devices integrated into microelectronic circuits, Nature 384 (1996) 338-341.

[17] P. Singh, S.N. Sharma, N.M. Ravindra. Applications of Porous Silicon Thin Films in Solar Cells and Biosensors, Jom 62 (2010) 15-24.

[18] W.A. Badawy. Porous silicon modified photovoltaic junctions: An approach to high-efficiency solar cells. in: ElNadi L, (Ed.). MTPR-06: Modern Trends in Physics Research, vol. 888. 2007. pp. 29-35.

[19] R. Soref. The past, present, and future of silicon photonics, Ieee Journal of Selected Topics in Quantum Electronics 12 (2006) 1678-1687.

[20] J. Salonen, A.M. Kaukonen, J. Hirvonen, V.-P. Lehto. Mesoporous silicon in drug delivery applications, Journal of Pharmaceutical Sciences 97 (2008) 632-653.

[21] I. Kleps, T. Ignat, M. Miu, F. Craciunoiu, M. Trif, M. Simion, A. Bragaru, A. Dinescu. Nanostructured Silicon Particles for Medical Applications, Journal of Nanoscience and Nanotechnology 10 (2010) 2694-2700.

[22] S. Singh, S.N. Sharma, Govind, S.M. Shivaprasad, M. Lal, M.A. Khan. Nanostructured porous silicon as functionalized material for biosensor application, Journal of Materials Science-Materials in Medicine 20 (2009) 181-187.

[23] A. Jane, R. Dronov, A. Hodges, N.H. Voelcker. Porous silicon biosensors on the advance, Trends in Biotechnology 27 (2009) 230-239.

[24] R.E. Serda, B. Godin, E. Blanco, C. Chiappini, M. Ferrari. Multi-stage delivery nano-particle systems for therapeutic applications, Biochimica Et Biophysica Acta-General Subjects 1810 (2011) 317-329.

[25] C.A. Prestidge, T.J. Barnes, C.-H. Lau, C. Barnett, A. Loni, L. Canham. Mesoporous silicon: a platform for the delivery of therapeutics, Expert Opinion on Drug Delivery 4 (2007) 101-110.

[26] J. Hernandez-Montelongo, A. Munoz-Noval, J.P. Garcia-Ruiz, V. Torres-Costa, R.J. Martin-Palma, M. Manso-Silvan. Nanostructured porous silicon: the winding road from photonics to cell scaffolds - a review, Frontiers in bioengineering and biotechnology 3 (2015) 60-60.

[27] P.C. Searson, J.M. Macaulay. The fabrication of porous silicon structures, Nanotechnology 3 (1992) 188.

[28] M.J. Sailor. Porous Silicon in Practice: Preparation, Characterization and Applications. First ed., Wiley-VCH Verlag GmbH & Co, 2012.

[29] E. Vazsonyi, E. Szilagyi, P. Petrik, Z.E. Horvath, T. Lohner, M. Fried, G. Jalsovszky. Porous silicon formation by stain etching, Thin Solid Films 388 (2001) 295-302.

[30] O. Bisi, S. Ossicini, L. Pavesi. Porous silicon: a quantum sponge structure for silicon based optoelectronics, Surface Science Reports 38 (2000) 1-126.

[31] E.A. Petrova, K.N. Bogoslovskaya, L.A. Balagurov, G.I. Kochoradze. Room temperature oxidation of porous silicon in air, Materials Science and Engineering B-Solid State Materials for Advanced Technology 69 (2000) 152-156.

[32] J. Salonen, V.P. Lehto, E. Laine. The room temperature oxidation of porous silicon, Applied Surface Science 120 (1997) 191-198.

[33] R.J. Martin-Palma, L. Pascual, P. Herrero, J.M. Martinez-Duart. Direct determination of grain sizes, lattice parameters, and mismatch of porous silicon, Applied Physics Letters 81 (2002) 25-27.

[34] R.J. Martin-Palma, L. Pascual, A.R. Landa-Canovas, P. Herrero, J.M. Martinez-Duart. HRTEM analysis of the nanostructure of porous silicon, Materials Science & Engineering C-Biomimetic and Supramolecular Systems 26 (2006) 830-834.

[35] L.E. Brus. electron-Electron and Electron-Hole Interactions in Small Semiconductor Crystallites - The Size Dependence of the Lowest Excited Electronic State, Journal of Chemical Physics 80 (1984) 4403-4409.

[36] Q.W. Chen, D.L. Zhu, C. Zhu, J. Wang, Y.G. Zhang. A way to obtain visible blue light emission in porous silicon, Applied Physics Letters 82 (2003) 1018.

[37] Y. Kanemitsu. Luminescence Properties of Nanometer-Sized Si Crystallites - Core and surface-States, Physical Review B 49 (1994) 16845-16848.

[38] M.V. Wolkin, J. Jorne, P.M. Fauchet, G. Allan, C. Delerue. Electronic states and luminescence in porous silicon quantum dots: The role of oxygen, Physical Review Letters 82 (1999) 197-200.

[39] S.E. Lewis, J.R. DeBoer, J.L. Gole, P.J. Hesketh. Sensitive, selective, and analytical improvements to a porous silicon gas sensor, Sensors and Actuators B-Chemical 110 (2005) 54-65.

[40] C. Jamois, C. Li, E. Gerelli, Y. Chevolot, V. Monnier, R. Skryshevskyi, R. Orobtchouk, E. Souteyrand, T. Benyattou. Porous-silicon based planar photonic crystals for sensing applications. in: Miguez HR, Romanov SG, Andreani LC, Seassal C, (Eds.). Photonic Crystal Materials and Devices Ix, vol. 7713. 2010.

[41] P. Granitzer, K. Rumpf. Porous Silicon-A Versatile Host Material, Materials 3 (2010) 943-998.

[42] S.P. Low, K.A. Williams, L.T. Canham, N.H. Voelcker. Generation of reactive oxygen species from porous silicon microparticles in cell culture medium, Journal of Biomedical Materials Research Part A 93A (2010) 1124-1131.

[43] R. Jugdaohsingh. Silicon and bone health, Journal of Nutrition Health & Aging 11 (2007) 99-110.

[44] C. Shaoqiang, Z. Jian, F. Xiao, W. Xiaohua, L. laiqiang, S. Yanling, X. Qingsong, W. Chang, Z. Jianzhong, Z. Ziqiang. Nanocrystalline ZnO thin films on porous silicon/silicon substrates obtained by sol-gel technique, Applied Surface Science 241 (2005) 384-391.

[45] X. Michalet, F. Pinaud, T.D. Lacoste, M. Dahan, M.P. Bruchez, A.P. Alivisatos, S. Weiss. Properties of fluorescent semiconductor nanocrystals and their application to biological labeling, Single Molecules 2 (2001) 261-276.

[46] G. Xiaohu, W.C.W. Chan, N. Shuming. Quantum-dot nanocrystals for ultrasensitive biological labeling and multicolor optical encoding, Journal of Biomedical Optics 7 (2002) 532-537.

[47] S.K. Murthy. Nanoparticles in modern medicine: State of the art and future challenges, International Journal of Nanomedicine 2 (2007) 129-141.

[48] N. O'Farrell, A. Houlton, B.R. Horrocks. Silicon nanoparticles: applications in cell biology and medicine, International Journal of Nanomedicine 1 (2006) 451.

[49] R. Subbiah, M. Veerapandian, K.S. Yun. Nanoparticles: Functionalization and Multifunctional Applications in Biomedical Sciences, Current Medicinal Chemistry 17 (2010) 4559-4577.

[50] S. Hediger, J. Fontannaz, A. Sayah, W. Hunziker, M.A.M. Gijs. Biosystem for the culture and characterisation of epithelial cell tissues, Sensors and Actuators B-Chemical 63 (2000) 63-73.

[51] A.P. Bowditch, K. Waters, H. Gale, P. Rice, E.A.M. Scott, L.T. Canham, C.L. Reeves, A. Loni, T.I. Cox. In-vivo assessment of tissue compatibility and calcification of bulk and porous silicon. Symposium on Microcrystalline and Nanocrystalline Semiconductors, at the 1998 MRS Fall Meeting, vol. 536. Boston, Ma, 1998. p.149-154.

[52] S.P. Low, N.H. Voelcker, L.T. Canham, K.A. Williams. The biocompatibility of porous silicon in tissues of the eye, Biomaterials 30 (2009) 2873-2880.

[53] L.M. Bonanno, L.A. DeLouise. Whole blood optical biosensor, Biosensors & Bioelectronics 23 (2007) 444-448.

[54] J. Lopez-Garcia, R.J. Martin-Palma, M. Manso, J.M. Martinez-Duart. Porous silicon based structures for the electrical biosensing of glucose, Sensors and Actuators B-Chemical 126 (2007) 82-85.

[55] R.E. Serda, J. Go, R.C. Bhavane, X. Liu, C. Chiappini, P. Decuzzi, M. Ferrari. The association of silicon microparticles with endothelial cells in drug delivery to the vasculature, Biomaterials 30 (2009) 2440-2448.

[56] L.A. DeLouise, B.L. Miller. Quantatitive assessment of enzyme immobilization capacity in porous silicon, Analytical Chemistry 76 (2004) 6915-6920.

[57] J.H. Park, A.M. Derfus, E. Segal, K.S. Vecchio, S.N. Bhatia, M.J. Sailor. Local heating of discrete droplets using magnetic porous silicon-based photonic crystals, Journal of the American Chemical Society 128 (2006) 7938-7946.

[58] T. Tanaka, P. Decuzzi, M. Cristofanilli, J.H. Sakamoto, E. Tasciotti, F.M. Robertson, M. Ferrari. Nanotechnology for breast cancer therapy, Biomedical Microdevices 11 (2009) 49-63.

[59] M.J. Llansola Portoles, F. Rodriguez Nieto, D.B. Soria, J.I. Amalvy, P.J. Peruzzo, D.O. Martire, M. Kotler, O. Holub, M.C. Gonzalez. Photophysical Properties of Blue-Emitting Silicon Nanoparticles, Journal of Physical Chemistry C 113 (2009) 13694-13702.

[60] L. Bychto, Y. Makushok, V. Chirvony, E. Matveeva. Pulse electrochemical method for porosification of silicon and preparation of porSi powder with controllable particles size distribution, Physica Status Solidi C - Current Topics in Solid State Physics, Vol 5, No 12 2008 5 (2008) 3789-3793.

[61] S.O. Meade, M.Y. Chen, M.J. Sailor, G.M. Miskelly. Multiplexed DNA Detection Using Spectrally Encoded Porous SiO2 Photonic Crystal Particles, Analytical Chemistry 81 (2009) 2618-2625.

[62] H. Elhouichet, M. Oueslati. Photoluminescence properties of porous silicon nanocomposites, Materials Science and Engineering B-Solid State Materials for Advanced Technology 79 (2001) 27-30.

[63] R. Herino. Nanocomposite materials from porous silicon, Materials Science and Engineering B-Solid State Materials for Advanced Technology 69 (2000) 70-76.

[64] A.J.H. Nguyen H. Tran, N. Lamb. Structural Order of Nanocrystalline ZnO Films. vol. 103: J. Phys. Chem. B, 1999. p.4264-4268.

[65] C.F. Wang, B. Hu, W.B. Li, H.H. Yi. Luminescence properties of ZnS/porous Si composites, Optik 125 (2014) 554-556.

[66] N.A. Davidenko, G.V. Kuznetsov, Y.S. Milovanov. Cadmium Sulfide-Porous Silicon Nanocomposite Structures, Ukrainian Journal of Physics 58 (2013) 163-170.

[67] L.T. Canham. Laser-Dye Impregnation of Oxidized Porous Silicon on Silicon-Wafers, Applied Physics Letters 63 (1993) 337-339.

[68] C. Cobianu, C. Savaniu, O. Buiu, D. Dascalu, M. Zaharescu, C. Parlog, A. van den Berg, B. Pecz. Tin dioxide sol-gel derived than films deposited on porous silicon, Sensors and Actuators B-Chemical 43 (1997) 114-120.

[69] B. Zhao, Q.S. Li, H.X. Qi, N. Zhang. White light emission from the composite system of ZnO/porous Si, Chinese Physics Letters 23 (2006) 1299-1301.

[70] R.G. Singh, F. Singh, D. Kanjilal, V. Agarwal, R.M. Mehra. White light emission from chemically synthesized ZnO-porous silicon nanocomposite, Journal of Physics D-Applied Physics 42 (2009).

[71] E. Kayahan. White light luminescence from annealed thin ZnO deposited porous silicon, Journal of Luminescence 130 (2010) 1295-1299.

[72] M.S. Kim, K.G. Yim, J.Y. Leem, S. Kim, G. Nam, D.Y. Kim, S.O. Kim, D.Y. Lee, J.S. Kim. Nanocrystalline ZnO Thin Films Grown on Porous Silicon by

Sol-gel Method and Effects of Post-annealing, Journal of the Korean Physical Society 59 (2011) 346-352.

[73] D. Dimova-Malinovska, M. Nikolaeva. Transport mechanisms and energy band diagram in ZnO/porous Si light-emitting diodes, Vacuum 69 (2002) 227-231.

[74] A. Janotti, C.G. Van de Walle. Fundamentals of zinc oxide as a semiconductor, Reports on Progress in Physics 72 (2009) 29.

[75] H.S. Kang, J.S. Kang, J.W. Kim, S.Y. Lee. Annealing effect on the property of ultraviolet and green emissions of ZnO thin films, Journal of Applied Physics 95 (2004) 1246-1250.

[76] S.B. Zhang, S.H. Wei, A. Zunger. Intrinsic n-type versus p-type doping asymmetry and the defect physics of ZnO, Physical Review B 63 (2001).

[77] R.G. Singh, F. Singh, V. Agarwal, R.M. Mehra. Photoluminescence studies of ZnO/porous silicon nanocomposites, Journal of Physics D-Applied Physics 40 (2007) 3090-3093.

[78] A. van Dijken, E.A. Meulenkamp, D. Vanmaekelbergh, A. Meijerink. The luminescence of nanocrystalline ZnO particles: the mechanism of the ultraviolet and visible emission, Journal of Luminescence 87-9 (2000) 454-456.

[79] S.Y. Ma, X.H. Yang, X.L. Huang, A.M. Sun, H.S. Song, H.B. Zhu. Effect of post-annealing treatment on the microstructure and optical properties of ZnO/PS nanocomposite films, Journal of Alloys and Compounds 566 (2013) 9-15.

[80] F. Tuomisto, K. Saarinen, D.C. Look, G.C. Farlow. Introduction and recovery of point defects in electron-irradiated ZnO, Physical Review B 72 (2005).

[81] B.X. Lin, Z.X. Fu, Y.B. Jia. Green luminescent center in undoped zinc oxide films deposited on silicon substrates, Applied Physics Letters 79 (2001) 943-945.

[82] D. Das, P. Mondal. Photoluminescence phenomena prevailing in c-axis oriented intrinsic ZnO thin films prepared by RF magnetron sputtering, Rsc Advances 4 (2014) 35735-35743.

[83] M.Y. Cho, M.S. Kim, H. Young, S.M. Jeon, G.S. Kim, D.Y. Kim, K.G. Yim, J.-Y. Leem, D.-Y. Lee, J.S. Kim, J.S. Kim, J.I. Lee. Effects of Growth Interruption of ZnO Buffer Layers on the Structural and the Optical Properties of ZnO Thin Films Grown by Using PA-MBE, Journal of the Korean Physical Society 56 (2010) 1833-1837.

[84] H. Cai, H.L. Shen, Y.G. Yin, L.F. Lu, J.C. Shen, Z.X. Tang. The effects of porous silicon on the crystalline properties of ZnO thin films, Journal of Physics and Chemistry of Solids 70 (2009) 967-971.

[85] Y.M. Huang, Q.-l. Ma, B.-g. Zhai. Wavelength tunable photoluminescence of ZnO/porous Si nanocomposites, Journal of Luminescence 138 (2013) 157-163.

[86] P. Ji-Ho, G. Luo, G. von Maltzahn, E. Ruoslahti, S.N. Bhatia, M.J. Sailor. Biodegradable luminescent porous silicon nanoparticles for in vivo applications, Nature Materials 8 (2009) 331-336.

[87] A.J. Nijdam, M.M.C. Cheng, M. Ferrari. X-ray photoelectron spectroscopy depth profile of chemically modified porous silicon, Journal of Vacuum Science & Technology B 24 (2006) 852-854.

[88] G. Palestino, V. Agarwal, R. Aulombard, E. Perez, C. Gergely. Biosensing and Protein Fluorescence Enhancement by Functionalized Porous Silicon Devices, Langmuir 24 (2008) 13765-13771.

[89] E.C. Wu, J.H. Park, J. Park, E. Segal, F. Cunin, M.J. Sailor. Oxidation-Triggered Release of Fluorescent Molecules or Drugs from Mesoporous Si Microplarticles, Acs Nano 2 (2008) 2401-2409.

[90] L. Martinez, O. Ocampo, Y. Kumar, V. Agarwal. ZnO-porous silicon nanocomposite for possible memristive device fabrication, Nanoscale Research Letters 9 (2014).

[91] D. Yan, M. Hu, S. Li, J. Liang, Y. Wu, S. Ma. Electrochemical deposition of ZnO nanostructures onto porous silicon and their enhanced gas sensing to NO2 at room temperature, Electrochimica Acta 115 (2014) 297-305.

[92] F. Severiano, G. Garcia, L. Castaneda, J.M. Gracia-Jimenez, H. Gomez-Pozos, J.A. Luna-Lopez. Electroluminescent Devices Based on Junctions of Indium Doped Zinc Oxide and Porous Silicon, Journal of Nanomaterials (2014).

[93] K.W. Kolasinski. Etching of silicon in fluoride solutions, Surface Science 603 (2009) 1904-1911.

[94] Y.J. Chabal, G.S. Higashi, K. Raghavachari, V.A. Burrows. Infrarred-Spectroscopy of Si(111) and Si(100) surfaces after HF treatment - Hydrogen Termination and Surface-Morphology, Journal of Vacuum Science & Technology a-Vacuum Surfaces and Films 7 (1989) 2104-2109.

[95] G.S. Higashi, Y.J. Chabal, G.W. Trucks, K. Raghavachari. Ideal hydrogen termination of the Siñ-(111) surface, Applied Physics Letters 56 (1990) 656-658.

[96] P. Allongue, V. Kieling, H. Gerischer. Etching Mechanism and Atomic-Structure of H-Si(111) Surfaces Prepared in NH4F, Electrochimica Acta 40 (1995) 1353-1360.

[97] V. Lehmann, U. Gosele. Porous Silicon Formation - A quantum Wire Effect, Applied Physics Letters 58 (1991) 856-858.

[98] X.G. Zhang. Morphology and Formation Mechanisms of Porous Silicon. vol. 151: J. Electrochem. Soc., 2004.

[99] E. Tasciotti, X.W. Liu, R. Bhavane, K. Plant, A.D. Leonard, B.K. Price, M.M.C. Cheng, P. Decuzzi, J.M. Tour, F. Robertson, M. Ferrari. Mesoporous silicon particles as a multistage delivery system for imaging and therapeutic applications, Nature Nanotechnology 3 (2008) 151-157.

[100] F. Erogbogbo, K.-T. Yong, I. Roy, G. Xu, P.N. Prasad, M.T. Swihart. Biocompatible luminescent silicon quantum dots for imaging of cancer cells, Acs Nano 2 (2008) 873-878.

[101] H.A. Santos, J. Riikonen, J. Salonen, E. Makila, T. Heikkila, T. Laaksonen, L. Peltonen, V.-P. Lehto, J. Hirvonen. In vitro cytotoxicity of porous silicon microparticles: Effect of the particle concentration, surface chemistry and size, Acta Biomaterialia 6 (2010) 2721-2731.

[102] P. Gupta, A.C. Dillon, A.S. Bracker, S.M. George. FTIR studies of H2O and D2O decomposition on porous silicon surfaces, Surface Science 245 (1991) 360-372.

[103] J.M. Curran, R. Chen, J.A. Hunt. Controlling the phenotype and function of mesenchymal stem cells in vitro by adhesion to silane-modified clean glass surfaces, Biomaterials 26 (2005) 7057-7067.

[104] J.H. Moon, J.H. Kim, K. Kim, T.H. Kang, B. Kim, C.H. Kim, J.H. Hahn, J.W. Park. Absolute surface density of the amine group of the aminosilylated thin layers: Ultraviolet-visible spectroscopy, second harmonic generation, and synchrotron-radiation photoelectron spectroscopy study, Langmuir 13 (1997) 4305.

[105] D. Wang, F.R. Jones. Surface analytical study of the interaction between gamma-amino propyl trimethoxysilane and E-glass surface, part 2: X-ray photoelectron spectroscopy, Journal of Materials Science 28 (1993) 2481-2488.

[106] S. Jo, K. Park. Surface modification using silanated poly(ethylene glycol)s, Biomaterials 21 (2000) 605-616.

[107] S.J. Sofia, V. Premnath, E.W. Merrill. Poly(ethylene oxide) grafted to silicon surfaces: Grafting density and protein adsorption, Macromolecules 31 (1998) 5059-5070.

[108] M.P. Schwartz. Chemical modification of silicon surfaces for biological applications. In: F. Cunin RWC, M.J. Sailor, (Ed.), vol. 202: Phy. Stat. Sol. (a), 2005. p.1380-1384.

[109] M. Arroyo-Hernandez, R.J. Martin-Palma, J. Perez-Rigueiro, J.P. Garcia-Ruiz, J.L. Garcia-Fierro, J.M. Martinez-Duart. Biofunctionalization of surfaces of nanostructured porous silicon, Materials Science & Engineering C-Biomimetic and Supramolecular Systems 23 (2003) 697-701.

[110] L. Znaidi. Sol-gel-deposited ZnO thin films: A review, Materials Science and Engineering B-Advanced Functional Solid-State Materials 174 (2010) 18-30.

[111] L. Znaidi, G. Illia, S. Benyahia, C. Sanchez, A.V. Kanaev. Oriented ZnO thin films synthesis by sol-gel process for laser application, Thin Solid Films 428 (2003) 257-262.

[112] L. Znaidi, G. Illia, R. Le Guennic, C. Sanchez, A. Kanaev. Elaboration of ZnO thin films with preferential orientation by a soft chemistry route, Journal of Sol-Gel Science and Technology 26 (2003) 817-821.

[113] Q.-l. Ma, B.-g. Zhai, Y.M. Huang. Sol-gel derived ZnO/porous silicon composites for tunable photoluminescence, Journal of Sol-Gel Science and Technology 64 (2012) 110-116.

[114] R.G. Singh. Fabrication of zinc silicate from ZnO-porous silicon naocomposite for broadband emission by chemical route. ICOP 2009 - International Conference on Optics and Photonics. Chandigarh (India), 2009.

[115] D.C.B. A.J. Garratt Reed. Energy-Dispersive X-Ray Analysis in the Electron Microscope, BIOS Scientific Publisher, 2003.

[116] R.P. R. González, C. Ballesteros. Microscopía electrónica, Eudema Universidad: Textos de Apoyo, 1991.

[117] J. Perrière. Rutherford backscattering spectrometry. vol. 37: Vacuum, 1987. p.429-432.

[118] J.F.B. D. Benoit, L. Van't Dack, H. Werner, J. Wernisch. Microbeam and Nanobeam Analysis. vol. Mikrochimica Acta 13: Springer Verlag, 1996.

[119] M.N. Yongqiang Wang. Handbook of Modern Ion Beam Materials Analysis. Cambridge University Press, 2010.

[120] H.K. Henisch. Electroluminescence vol. International Series of Monographs on Semiconductors: Pergamon Press, 1962.

[121] B.D. Cullity. Elements of X-ray Diffraction. Third ed., Prentice-Hall, 2001.

[122] C.S.S.R. Kumar. UV-VIS and Photoluminescence Spectroscopy for Nanomaterials Characterization. vol. 2: Springer Verlag, 2013.

[123] M.M. Silvan, M. Langlet, J.M.M. Duart, P. Herrero. Preparation of interfaces for TEM cross-section observation, Nuclear Instruments & Methods in Physics Research Section B-Beam Interactions with Materials and Atoms 257 (2007) 623-626.

[124] G. Bunker. Introduction to XAFS: A Practical Guide to X-ray Absorption Spectroscopy, Cambridge University Press, 2010.

[125] S. Hüfner. Photoelectron spectroscopy: principles and applications. Springer Verlag, 1996.

[126] M.P.S. D. Briggs. Practical Surface Analysis - Auger and X-ray Photoelectron Spectroscopy. Wiley Interscience, 1990.

[127] M. Mayer. SIMNRA, a simulation program for the analysis of NRA, RBS and ERDA, Application of Accelerators in Research and Industry, Pts 1 and 2 475 (1999) 541-544.

[128] C. Huan-sheng. The studies of non-Rutherford backscattering cross sections of ^{4}He from ^{16}O. vol. 2: Acta Phys. Sin., 1993. p.641.

[129] M.N. J.R. Tesmer. Handbook of Modern Ion Beam Materials Analysis, Materials

Research Society, 1995.

[130] B. Ravel, M. Newville. ATHENA, ARTEMIS, HEPHAESTUS: data analysis for X-ray absorption spectroscopy using IFEFFIT, Journal of Synchrotron Radiation 12 (2005) 537-541.

[131] J.J. Rehr, J.J. Kas, M.P. Prange, A.P. Sorini, Y. Takimoto, F. Vila. Ab initio theory and calculations of X-ray spectra, Comptes Rendus Physique 10 (2009) 548-559.

[132] A. Munoz-Noval, V. Sanchez Vaquero, V. Torres-Costa, D. Gallach, V. Ferro-Llanos, J.J. Serrano, F. del Pozo, M. Manso-Silvan, J.P. Garcia Ruiz, R.J. Martin-Palma, R. MartinPalma, Y. Jen, A. Lakhtakia. Nanostructured porous silicon-based dual luminescent/magnetic particles for biomedical tracking, Nanostructured Thin Films Iii 7766 (2010).

[133] A. Munoz-Noval, V. Sanchez-Vaquero, V. Torres-Costa, D. Gallach, V. Ferro-Llanos, J.J. Serrano, M. Manso-Silvan, J.P. Garcia-Ruiz, F. del Pozo, R.J. Martin-Palma. Hybrid luminescent/magnetic nanostructured porous silicon particles for biomedical applications, Journal of Biomedical Optics 16 (2011).

[134] Á. Muñoz-Noval. Estructuras Híbridas de Silicio Poroso y Metal/Óxido de Metal: Síntesis, caracterización y aplicaciones en biomedicina. Department of Applied Physics, vol. PhD: Universidad Autónoma de Madrid, 2011. p.192.

[135] P.A. Vesilind. The Rosin-Rammler particle size distribution. vol. 5: Resource Recovery and Conservation, 1980. p.275-277.

[136] H.C. Hsu, C.S. Cheng, C.C. Chang, S. Yang, C.S. Chang, W.F. Hsieh. Orientation-enhanced growth and optical properties of ZnO nanowires grown on porous silicon substrates, Nanotechnology 16 (2005) 297-301.

[137] M.J. E. Pinèík, J. Barto, C. Falcony, M. Kuèera. The C-V investigation of light-related properties of porous silicon/crystalline silicon structure. vol. 9: Superficies y vacío, 1999.

[138] R.G. Singh, F. Singh, R.M. Mehra, D. Kanjilal, V. Agarwal. Synthesis of nanocrystalline alpha-Zn2SiO4 at ZnO-porous silicon interface: Phase transition study, Solid State Communications 151 (2011) 701-703.

[139] C. Giacovazzo. Fundamentals of crystallography. Oxford Sciences Press, 1994.

[140] P. Scherrer. Bestimmung der Größe und der inneren Struktur von Kolloidteilchen mittels Röntgenstrahlen. vol. 1918: Nachrichten von der Gesellschaft der Wissenschaften zu Göttingen, Mathematisch-Physikalische Klasse, 1918. p.98 - 100.

[141] D.R. Sahu, C.-L. Wu, J.-L. Huang. Observation of Quantum Confinement Effect on ZnO Embedded Mesoporous Silica, Journal of Nanoscience and Nanotechnology 12 (2012) 2543-2547.

[142] U. Manzoor, M. Islam, L. Tabassam, S.U. Rahman. Quantum confinement effect in ZnO nanoparticles synthesized by co-precipitate method, Physica E-Low-Dimensional Systems & Nanostructures 41 (2009) 1669-1672.

[143] A. Parisini, R. Angelucci, L. Dori, A. Poggi, P. Maccagnani, G.C. Cardinali, G. Amato, G. Lerondel, D. Midellino. TEM characterisation of porous silicon, Micron 31 (2000) 223-230.

[144] M.I.J. Beale, J.D. Benjamin, M.J. Uren, N.G. Chew, A.G. Cullis. An experimental and theoretical study of the formation and microstructure of porous silicon, Journal of Crystal Growth 73 (1985) 622-636.

[145] J. Haug, A. Chasse, M. Dubiel, C. Eisenschmidt, M. Khalid, P. Esquinazi. Characterization of lattice defects by x-ray absorption spectroscopy at the Zn K-edge in ferromagnetic, pure ZnO films, Journal of Applied Physics 110 (2011).

[146] A. Kuzmin, J. Chaboy. EXAFS and XANES analysis of oxides at the nanoscale, IUCrJ 1 (2014) 571-589.

[147] A. Kuzmin, S. Larcheri, F. Rocca. Zn K-edge XANES in nanocrystalline ZnO. Conference on Functional Materials and Nanotechnologies, vol. 93. Riga, Latvia, 2007.

[148] C. Drouilly, J.M. Krafft, F. Averseng, S. Casale, D. Bazer-Bachi, C. Chizallet, V. Lecocq, H. Vezin, H. Lauron-Pernot, G. Costentin. ZnO Oxygen Vacancies Formation and Filling Followed by in Situ Photoluminescence and in Situ EPR, Journal of Physical Chemistry C 116 (2012) 21297-21307.

[149] J. Tauc, Grigorov.R, A. Vancu. Optical properties and electronic structure of amorphous germanium, Physica Status Solidi 15 (1966) 627-&.

[150] P. Kubelka. New contributions to the optics of intensely light-scattering materials (1), Journal of the Optical Society of America 38 (1948) 448-457.

[151] P. Kubelka. New contributions to the optics of intensely light-scattering materials (2) Nonhomogeneous layers, Journal of the Optical Society of America 44 (1954) 330-335.

[152] H. Guangxia, L. Shi Qiang, G. Hao, Z. Yanlin, Z. Jixuan, T.L. Sudesh, L. Wijesinghe, D.J. Blackwood. White light from an indium zinc oxide/porous silicon light-emitting diode, Journal of Physical Chemistry C 113 (2009) 751-754.

[153] V. Lehmann, B. Jobst, T. Muschik, A. Kux, V. Petrovakoch. Correlation between optical-properties and crystallite size in porous silicon, Japanese Journal of Applied Physics Part 1-Regular Papers Short Notes & Review Papers 32 (1993) 2095-2099.

[154] N. Balasubramanian, A. Subrahmanyam. Studies on evaporated indium tin oxide (ITO)/silicon junctions and an estimation of ITO work function, Journal of the Electrochemical Society 138 (1991) C22-24.

[155] K. Jacobi, G. Zwicker, A. Gutmann. Work function, electron affinity and band bending of Zinc-Oxide surfaces, Surface Science 141 (1984) 109-125.

[156] K.K.N. S. M. Sze. Physics of semiconductor devices, Wiley, 2006.

[157] A.S. Gudovskikh, S. IbrahiM, J.P. Kleider, J. Damon-Lacoste, P.R.I. Cabarrocas, Y. Veschetti, P.J. Ribeyron. Determination of band offsets in a-Si : H/c-Si heterojunctions from capacitance-voltage measurements: Capabilities and limits, Thin Solid Films 515 (2007) 7481-7485.

[158] E.W.J. Mitchell. The Work Functions of Copper, Silver and Aluminium. vol. 210: Proceedings of the Royal Society. A, Mathematical, physical, and engineering sciences, 1951. p.70 - 84.

[159] J.M. Beebe, B. Kim, J.W. Gadzuk, C.D. Frisbie, J.G. Kushmerick. Transition from direct tunneling to field emission in metal-molecule-metal junctions, Physical Review Letters 97 (2006).

[160] Z. Li, R. Yang, M. Yu, F. Bai, C. Li, Z.L. Wang. Cellular Level Biocompatibility and Biosafety of ZnO Nanowires, Journal of Physical Chemistry C 112 (2008) 20114-20117.